

**DEVELOPMENT AND IMPLEMENTATION OF CONVERGENCE
DIAGNOSTICS AND ACCELERATION METHODOLOGIES IN
MONTE CARLO CRITICALITY SIMULATIONS**

A Dissertation
Presented to
The Academic Faculty

by

Shi, Bo

In Partial Fulfillment
of the Requirements for the Degree
Doctor of Philosophy in the
George W. Woodruff School of Mechanical Engineering

Georgia Institute of Technology
May 2012

COPYRIGHT 2011 BY GEORGIA INSTITUTE OF TECHNOLOGY

**DEVELOPMENT AND IMPLEMENTATION OF CONVERGENCE
DIAGNOSTICS AND ACCELERATION METHODOLOGIES IN
MONTE CARLO CRITICALITY SIMULATIONS**

Approved by:

Dr. Bojan Petrovic, Advisor
Nuclear and Radiological Engineering
School of Mechanical Engineering
Georgia Institute of Technology

Dr. Farzad Rahnema
Nuclear and Radiological Engineering
School of Mechanical Engineering
Georgia Institute of Technology

Dr. Dingkang Zhang
Nuclear and Radiological Engineering
School of Mechanical Engineering
Georgia Institute of Technology

Dr. Nicoleta Serban
School of Industrial and Systems
Engineering
Georgia Institute of Technology

Dr. Yingjie Liu
School of Mathematics
Georgia Institute of Technology

Dr. John Wagner
Reactor and Nuclear Systems Division
Oak Ridge National Laboratory

Date Approved: Nov. 30th, 2011

[This dissertation is dedicating to my parents and my wife, Anjie Xie, for their remarkable supports of every decision I made]

ACKNOWLEDGEMENTS

I would like to express my deepest appreciation to my advisor, Dr. Bojan Petrovic, for his valuable advices and unparalleled support. I am also grateful to Dr. Farzad Rahnema, Dr. Dingkang Zhang, Dr. Nicoleta Serban, Dr. Yingjie Liu, and Dr. John Wagner for their kindness to be my committee members and their invaluable suggestions. I gratefully acknowledge the help of Dr. Thomas Booth for the instructive discussions. I would like to recognize the effort that I received from my colleagues and friends in Georgia Institute of Technology for the past four years. Special thanks to my senior fellow apprentices, Dr. Bo Lu and Mr. Zhan Zhang for their relentless support.

TABLE OF CONTENTS

	Page
ACKNOWLEDGEMENTS	iv
LIST OF TABLES	viii
LIST OF FIGURES	x
LIST OF SYMBOLS AND ABBREVIATIONS	xiii
SUMMARY	xvi
 <u>CHAPTER</u>	
1 Introduction	1
Time-dependent Neutron Transport Equation	1
Steady-state Neutron Transport Equation	2
Power Iteration Method	3
Challenges and Possible Solutions	4
2 Review of the Convergence Diagnostics Methods	6
Benchmark Problems	6
The Bounding Approach	10
Variance Comparison with Parallel Runs	12
The Shannon Entropy Indicator	14
Entropy-related Diagnostics Methods	18
Combined KPSS Method	21
Statistical Diagnostics with Mesh Sources	23
3 Linear Regression Diagnostics Method	25
Ordinary Linear Regression Model	25
Hypothesis Testing of the Linear Regression Model	26

Diagnostics Procedure for Monte Carlo Simulations	27
One-dimensional Test Example	28
Simplified Benchmark Problem—50,000 Case	35
Simplified Benchmark Problem—500,000 Case	43
Auto-correlated Linear Regression Model	47
Conclusions and Future Work	49
4 Review of the Convergence Acceleration Methods	51
Fission Matrix Method	51
Anchoring Method	53
Wielandt’s Method	55
Smoothed Residual Acceleration Method	57
5 The Modified Power Iteration Acceleration Method	59
Review of the Modified Power Iteration Method	59
Derivations of the Convergence and Convergence Rate	60
Matrix Example and Collapse	65
Refinements to Avoid the Collapse	67
Net-Weight Calculation Schemes	70
One-dimensional Two-group Monte Carlo Simulation Examples	73
Convergence Acceleration Illustration	82
Recent Developments of Related Methods	87
Conclusions and Future Work	89
6 The Source Point Pairing Scheme for Net-Weight Calculation to Obtain the Second Eigenmode	91
Taking into Account the Negative Neutrons	91
Pairing Net-Weight Calculation	93

Issues and Adjustments Prepared for Application to Symmetric One-Dimensional Problems	101
Application to One-Dimensional Problems	105
Conclusions and Future Work	114
7 Conclusions and Future Work	116
REFERENCES	118

LIST OF TABLES

	Page
Table 2.1: Material atom densities of the storage fuel pool benchmark problem (atoms/ 10^{-24} cm ³)	9
Table 2.2: Null hypothesis conditions of the KPSS test	22
Table 3.1: Material information of both HRM and LRM for the one-dimensional testing problem for the linear regression model (Ref. 21)	29
Table 3.2: Summary of the relative differences of the flux distributions between the 250 th generation and a reference simulation for one-dimensional testing problem for the linear regression model	34
Table 3.3: Summary of the minimal t-values for regression sizes $n=65$ and 67 with mesh no. 138 for the simplified benchmark problem for the linear regression model, under $\alpha=0.20$	40
Table 5.1: Fissionable material information for one region example used for the modified power iteration method (Ref. 38) (cross-section in cm ⁻¹)	74
Table 5.2: Comparison of k_{eff} for one region example using the modified power iteration method (Ref. 38)	74
Table 5.3: Comparison of k_2 for one region example using the modified power iteration method (Ref. 38)	75
Table 5.4: Fractions of relative distances in combined standard deviations for one region example (in %) using the modified power iteration method (Ref. 38)	77
Table 5.5: Non-fissionable material information for multiple regions example used for the modified power iteration method (Ref. 38) (cross-section in cm ⁻¹)	79
Table 5.6: Comparison of k_{eff} for multiple regions example using the modified power iteration method (Ref. 38)	80
Table 5.7: Comparison of k_2 for multiple regions example using the modified power iteration method (Ref. 38)	81
Table 5.8: Summary of the convergence acceleration effect	87
Table 6.1: Properties of the fissionable material used for the mono-energetic example with pairing scheme (Ref. 49)	106

Table 6.2: Summary of the second eigenvalue estimates with computational time of the mono-energetic problem using pairing scheme (Ref. 49)	109
Table 6.3: Material properties used in the two-group problem for the pairing scheme (all macroscopic cross sections in cm^{-1}) (Ref. 49)	111
Table 6.4: Summary of the second eigenvalue estimates with computational time of the two-group problem using pairing scheme (Ref. 49)	112

LIST OF FIGURES

	Page
Figure 2.1: Geometry specification of the storage fuel pool benchmark problem (unit in cm)	8
Figure 2.2: Bounding of the sandwich method example (Fig.6 from Ref. 10)	11
Figure 2.3: Evolution of k_{eff} for the four 50K cases without inactive cycles (Ref. 11)	13
Figure 2.4: Evolution of k_{eff} for the four 50K cases with 5,000 inactive cycles (Ref. 11)	14
Figure 2.5: Cycle-wise entropies example (Fig. 14 from Ref. 13)	16
Figure 2.6: Evolution of the entropy values for the four 50K cases (Ref. 11)	17
Figure 2.7: Posterior relative entropy example (Fig. 13 from Ref. 13)	19
Figure 2.8: PRE with respect to the first cycle example (Fig. 11 from Ref. 13)	20
Figure 2.9: PRE plots with respect to the 501th cycle example (Fig. 12 from Ref. 13)	21
Figure 3.1: Geometry structure of the one-dimensional test problem for the linear regression model (Ref. 21)	28
Figure 3.2: Evolution of the entropy values for the one-dimensional test problem for the linear regression model (Ref. 21)	30
Figure 3.3: Converged generation for one-dimensional testing problem for the linear regression model with $\alpha=0.10$ (Ref. 21)	31
Figure 3.4: Converged generation for one-dimensional testing problem for the linear regression model with $\alpha=0.20$ (Ref. 21)	31
Figure 3.5: Changes of the flux distribution from different generations with a reference flux distribution for one-dimensional testing problem for the linear regression model	33
Figure 3.6: Geometry of the simplified storage fuel pool benchmark problem (Ref. 21)	36
Figure 3.7: Evolution of the entropy values of the simplified benchmark problem for the linear regression model (Ref. 21)	37

Figure 3.8: Converged generation for the simplified benchmark problem for the linear regression model (regression size n between 3 and 85)	38
Figure 3.9: Changes of T-values for regression sizes $n=65$ and 67 with mesh no. 138 for the simplified benchmark problem for the linear regression model, under $\alpha=0.20$	39
Figure 3.10: Evolution of the estimated flux in mesh no. 138 for the simplified benchmark problem for the linear regression model, up to 300 generations	41
Figure 3.11: Evolution of the estimated flux in mesh no. 138 for the simplified benchmark problem for the linear regression model, up to 2,000 generations	42
Figure 3.12: Converged generation for the simplified benchmark problem for the linear regression model (regression size n between 51 and 151)	43
Figure 3.13: Converged generation for the simplified benchmark problem with 500K histories per cycle for the linear regression model (regression size n between 3 and 301)	45
Figure 3.14: Evolution of the estimated flux in mesh no. 1 for the simplified benchmark problem with 500K histories per cycle for the linear regression model, up to 1,600 generations	46
Figure 3.15: Comparison of the linear regression model and the transformed model for the simplified benchmark problem	48
Figure 5.1: Eigenvalue estimates for the matrix problem using the modified power iteration method (Ref. 34)	66
Figure 5.2: Eigenvalue estimates for the matrix problem using the first refinement from of the modified power iteration method (Ref. 34)	68
Figure 5.3: Comparisons of reference fluxes and computed fluxes for the fundamental eigenmode for one region example using the modified power iteration method (Ref. 38)	76
Figure 5.4: Comparisons of reference fluxes and computed fluxes for the second eigenmode for one region example using the modified power iteration method (Ref. 38)	78
Figure 5.5: Geometry structure of multiple regions example used for the modified power iteration method (Ref. 38)	79

Figure 5.6: Comparisons of reference fluxes and computed fluxes for the fundamental eigenmode for multiple regions example using the modified power iteration method (Ref. 38)	81
Figure 5.7: Comparisons of reference fluxes and computed fluxes for the second eigenmode for multiple regions example using the modified power iteration method (Ref. 38)	82
Figure 5.8: Convergence acceleration example (Fig. 5 from Ref. 32)	84
Figure 5.9: Convergence acceleration shown with MSE of the flux distribution in logarithmic scale using the modified power iteration method (problem size 9 MFP)	85
Figure 5.10: Convergence acceleration shown with MSE of the flux distribution in logarithmic scale using the modified power iteration method with increased cross-sections	86
Figure 6.1: Histograms of the collision position samples (Ref. 49)	96
Figure 6.2: Combined histogram of the collision position samples (Ref. 49)	97
Figure 6.3: Collision density functions for collisions from positive, negative, and combined sources (Ref. 49)	98
Figure 6.4: Comparison of collision density functions of different point source positions (Ref. 49)	100
Figure 6.5: Sorting and pairing example (Ref. 49)	102
Figure 6.6: Illustration of the sampling procedure with angular dependence (Ref. 49)	103
Figure 6.7: Second eigenfunction estimate of the mono-energetic problem using sorting and pairing scheme (Ref. 49)	107
Figure 6.8: Second eigenfunction estimate of the mono-energetic problem using random pairing scheme (Ref. 49)	108
Figure 6.9: Second eigenfunction estimate of the two group problem using sorting and pairing scheme	113
Figure 6.10: Relative differences in the unit of combined standard deviation of the two group problem using sorting and pairing scheme	114

LIST OF SYMBOLS AND ABBREVIATIONS

$\psi(\vec{r}, \hat{\Omega}, E, t)$	Neutron flux
$\sigma(\vec{r}, E)$	Microscopic total cross-section
$q(\vec{r}, \hat{\Omega}, E, t)$	Neutron source term
$s(\vec{r}, \hat{\Omega}, E, t)$	External source term
$\sigma_s(\vec{r}, E' \rightarrow E, \hat{\Omega}' \rightarrow \hat{\Omega})$	Microscopic scattering cross-section
$\sigma_f(\vec{r}, E' \rightarrow E, \hat{\Omega}' \rightarrow \hat{\Omega})$	Microscopic fission cross-section
A	An operator or matrix
k_i	i^{th} eigenvalue
Ψ_i	i^{th} eigenfunction
Ψ	Any well-behaved function
k_1	Fundamental eigenvalue
Ψ_1	Fundamental eigenfunction
k_2	Second eigenvalue
Ψ_2	Second eigenfunction
$H(S^B)$	Shannon entropy
$D(S^B T^B)$	Relative Entropy
w	Test statistic for KPSS method
S_m^n	Mesh-wise fission source intensity
Y_i	Responding variable
X_i	Predicting variable
ε_i	Independent random error

σ^2	Variance of the random error
β_0	Constant coefficient
β_1	Linear coefficient
t	T-value
α	Significance level
n	Regression size
k_w	Wielandt's arbitrary parameter
a_i	One set of decomposition coefficients
b_i	The other set of decomposition coefficients
x	Unknown parameter
α_i	Assisting variable
β_i	The other assisting variable
R_i	j^{th} region
N_{ij}	Integral of eigenfunction Ψ_j in R_i
r	Estimated root
$f^+(x)$	Positive collision density function
$f^-(x)$	Negative collision density function
f^\pm	Combined collision density function
μ	Cosine of the angle between travelling direction and positive direction
n_1	Number of sources in positive source bank
n_2	Number of sources in negative source bank
k_{eff}	Effective multiplication factor
m_{sl}	Maximum stationary level

<i>PRE</i>	Progressive relative entropy
COM	Center of mass
HRM	High reactive material
LRM	Low reactive material
p-CMFD	Partial current-based coarse mesh finite difference
SRA	Smoothed residual acceleration
MSE	Mean squared error
MFP	Mean free path

SUMMARY

Because of the accuracy and ease of implementation, the Monte Carlo methodology is widely used in the analysis of nuclear systems. The estimated effective multiplication factor (k_{eff}) and flux distribution are statistical by their natures. In eigenvalue problems, however, neutron histories are not independent but are correlated through subsequent generations. Therefore, it is necessary to ensure that only the converged data are used for further analysis. Discarding a larger amount of initial histories would reduce the risk of contaminating the results by non-converged data, but increase the computational expense. This issue is amplified for large nuclear systems with slow convergence. One solution would be to use the convergence of k_{eff} or the flux distribution as the criterion for initiating accumulation of data. Although several approaches have been developed aimed at identifying convergence, these methods are not always reliable, especially for slow converging problems. This dissertation has attacked this difficulty by developing two independent but related methodologies. One aims to find a more reliable and robust way to assess convergence by statistically analyzing the local flux change. The other forms a basis to increase the convergence rate and thus reduce the computational expense. Eventually, these two topics will contribute to the ultimate goal of improving the reliability and efficiency of the Monte Carlo criticality calculations.

CHAPTER 1

INTRODUCTION

The Monte Carlo method is a tremendous outcome from the Manhattan Project¹. Although the computational power around 1940s was extremely low, the entire principle and concepts of the Monte Carlo method was established around that era. Due to the immense development of the new generations of work stations, clusters, and personal computers in the last half of the 20th century, using the Monte Carlo method for statistical experiment is more and more feasible. As the direct inheritors of the initialization of the Monte Carlo method, nuclear engineers are using the Monte Carlo method to analyze nuclear systems, simulate nuclear facilities, and develop the next generation nuclear power plants.

1.1 Time-dependent Neutron Transport Equation

The principle of the Monte Carlo method is to simulate the behaviors of neutrons in the specific systems. Essentially, the travelling and reactions of neutrons follow rules corresponding to the probabilities of certain interactions, which are summarized and expressed by the neutron transport equation²

$$\frac{1}{v} \frac{\partial}{\partial t} \psi(\vec{r}, \hat{\Omega}, E, t) + \hat{\Omega} \cdot \vec{\nabla} \psi(\vec{r}, \hat{\Omega}, E, t) + \sigma(\vec{r}, E) \psi(\vec{r}, \hat{\Omega}, E, t) = q(\vec{r}, \hat{\Omega}, E, t). \quad (1.1)$$

In Eq. (1.1), $\psi(\vec{r}, \hat{\Omega}, E, t)$ is the neutron flux; $\sigma(\vec{r}, E)$ is the cross-section of the materials; and $q(\vec{r}, \hat{\Omega}, E, t)$ is the neutron source term. Although seven variables—position, direction, energy, and time—exist in the expression of the flux, solving the differential equation is not so hard if the source term is explicitly available. Unfortunately, the source term is almost always implicit even without multiplying materials because it contains the desired neutron flux in its expression as a scattering term.

$$q(\vec{r}, \hat{\Omega}, E, t) = s(\vec{r}, \hat{\Omega}, E, t) + \int_0^{+\infty} dE' \int d\Omega \sigma_s(\vec{r}, E' \rightarrow E, \hat{\Omega}' \rightarrow \hat{\Omega}) \psi(\vec{r}, \hat{\Omega}', E', t) \quad (1.2)$$

In Eq. (1.2), $s(\vec{r}, \hat{\Omega}, E, t)$ is the external source term, and $\sigma_s(\vec{r}, E' \rightarrow E, \hat{\Omega}' \rightarrow \hat{\Omega})$ is the scattering cross-section, which leads to the scattering source term. This type of problem is generally referred to as a fixed source or shielding problem. With this implicit source, solving the transport equation is more difficult. By applying certain approximations (e.g., discretization of space and energy and collocation of direction), the neutron flux can be solved numerically. However, when multiplying materials exist, such as uranium or plutonium, the source term has to include the fission source term

$$\int_0^{+\infty} dE' \int d\Omega \nu \sigma_f(\vec{r}, E' \rightarrow E, \hat{\Omega}' \rightarrow \hat{\Omega}) \psi(\vec{r}, \hat{\Omega}', E', t). \quad (1.3)$$

In Eq. (1.3), ν is the average number of neutrons born per fission reaction and $\sigma_f(\vec{r}, E' \rightarrow E, \hat{\Omega}' \rightarrow \hat{\Omega})$ is the fission cross-section. The transport equation is not stationary in time then with the presence of fission sources; the neutron flux is either increasing or decreasing in most cases exponentially.

1.2 Steady-state Neutron Transport Equation

In the analysis of critical systems, the steady-state neutron flux is usually of interest. Therefore, by eliminating the time derivative term, discarding external sources, and introducing a parameter k , the neutron transport equation turns into Eq. (1.4).

$$\hat{\Omega} \cdot \vec{\nabla} \psi(\vec{r}, \hat{\Omega}, E, t) + \sigma(\vec{r}, E) \psi(\vec{r}, \hat{\Omega}, E, t) = \int_0^{+\infty} dE' \int d\Omega \left[\sigma_s(\vec{r}, E' \rightarrow E, \hat{\Omega}' \rightarrow \hat{\Omega}) + \frac{1}{k} \nu \sigma_f(\vec{r}, E' \rightarrow E, \hat{\Omega}' \rightarrow \hat{\Omega}) \right] \psi(\vec{r}, \hat{\Omega}', E', t) \quad (1.4)$$

The purpose of the parameter k is to balance the equation such that the solution is a time-independent neutron flux. This type of problems is classified as criticality or eigenvalue problems, because with operator notations, k behaves like an eigenvalue. In steady-state, only the fundamental eigenvalue remains, and all the higher eigenvalues terms decay to

be zero. The fundamental eigenvalue is called the effective multiplication factor and denoted as k_{eff} . In general, both the fundamental eigenvalue and fundamental eigenfunctions, which is also the steady-state flux distribution, are of interest.

1.3 Power Iteration Method

These two quantities can be solved either by numerical methods iteratively with approximations, or by Monte Carlo simulations. The power iteration method³ has been proved to be a reliable and efficient approach to accomplish this goal by applying to deterministic methods or Monte Carlo simulations. The power iteration method is originally proposed to solve for the fundamental eigenpair (eigenfunction and eigenvalue) of a matrix or operator A . Essentially, the matrix or operator A has a discrete set of eigenvalues, notated as k_i , and eigenfunctions, notated as Ψ_i , which satisfy equation

$$A \psi_i = k_i \psi_i. \quad (1.5)$$

The subscript corresponds to the order of the absolute value of eigenvalues:

$|k_1| > |k_2| > \dots$. All of the eigenfunctions together could generate a subspace because of the completeness and orthogonality of the eigenfunctions. Therefore, any “well-behaved” function Ψ can be expanded into the eigenfunction basis, shown in Eq. (1.6).

$$\Psi = \sum_{i=1}^{\infty} a_i \Psi_i \quad (1.6)$$

If applying the operator A repeatedly on Ψ , certain estimates with normalization, shown in Eq. (1.7), converge to the fundamental eigenpair.

$$\lim_{n \rightarrow \infty} \frac{1}{k_1^n} A^n \Psi = \Psi_1, \text{ and } k_1 = \lim_{n \rightarrow \infty} \frac{A^n \Psi}{A^{n-1} \Psi} \quad (1.7)$$

The ratio $|k_2|/|k_1|$, which is called the dominance ratio, determines the convergence rate of the power iteration method. Since the ultimately remaining components is the fundamental eigenfunction, larger dominance ratio leads to slower

decay or slower computation. In other words, smaller dominance ratio would lead to faster convergence of a numerical solution.

1.4 Challenges and Possible Solutions

Unfortunately, small dominance ratio is typically not the case in real life applications. The size of nuclear systems is usually relatively large compared with the propagation ability (or mean free path, MFP) of neutrons. Therefore, the communication of neutrons is generally weak. Numerically, this kind of systems is represented by a high dominance ratio, which is close to but smaller than one. The slow convergence issue coming with high dominance ratio yields many challenging problems; one well-known example with slow convergence is the “criticality of the world”⁴ problem. These problems may still be difficult to simulate even with high performance computers.

With slow convergence systems, to determine the convergence is really difficult. Traditionally, due to the limit of the computational capability, only k_{eff} was computed and tested for convergence. The convergence diagnostics was based on the evolution of the k_{eff} sequence. However, the convergence of k_{eff} cannot guarantee the convergence of these detailed quantities. Therefore, the unreliability of the previous diagnostics methods was identified, which is because of the quicker convergence of integral quantities such as k_{eff} than the local detailed quantities such as flux distribution. Thus, one possible solution in order to obtain a reliable output, investigated in this thesis, is to utilize local information to perform convergence diagnostics.

On the other hand, if the convergence procedure can be accelerated, the difficulty of convergence diagnostics will decrease. Meanwhile, higher efficiency will also be achieved. Various attempts have been made during the past twenty years by combining deterministic methods and the Monte Carlo method to achieve this objective. Recently, a new approach that mainly depends on the Monte Carlo method has been proposed⁵, with an innovative approach to attack the challenge.

This dissertation is trying to address several aspects of the challenge in order to prepare for the future modification and implementations from these two angles

1. Development of a reliable and robust statistical method to assess the convergence by analyzing the trends of local flux distribution.
2. Development of an efficient approach to increasing the convergence rate in order to assist the convergence diagnostics and reduce computational cost.

Chapter 2 reviews several known convergence diagnostics methods from previous works.

Chapter 3 provides a new approach to perform the convergence diagnostics by applying statistical methods (ordinary and auto-correlated linear regression) to diagnose convergence focusing on the local information, such as the flux or source distribution.

Chapter 4 provides a critical review of several convergence acceleration methods.

Chapter 5 presents the concept and results of numerical examples of the new acceleration method, based on modified power iteration method. Chapter 6 introduces a method for generating the second eigenpair (beside the fundamental one) together with a novel approach for determining the net-weight of positive/negative histories, which has been the main difficulty in development of this class of methods. Chapter 7 concludes this dissertation and lists some guidelines for future work.

CHAPTER 2

REVIEW OF THE CONVERGENCE DIAGNOSTICS METHODS

Many attempts to determine the convergence of the Monte Carlo criticality simulations are available. Some of them are based on k_{eff} or other integral quantities, which have been proved to be unreliable^{4, 6, and 7} for slow convergence problems without extra cautions. The other methods rely on either different quantities extracted from local information or a series of quantities representing local information. In order to be able to identify the true and false convergence, it is necessary to understand the advantages and drawbacks of these methods for real-life computations. Several benchmark problems were proposed to assist to identify the performance and improvements of various diagnostics methods. One such problem will be used in this chapter to help present and review previously developed convergence diagnostics methods.

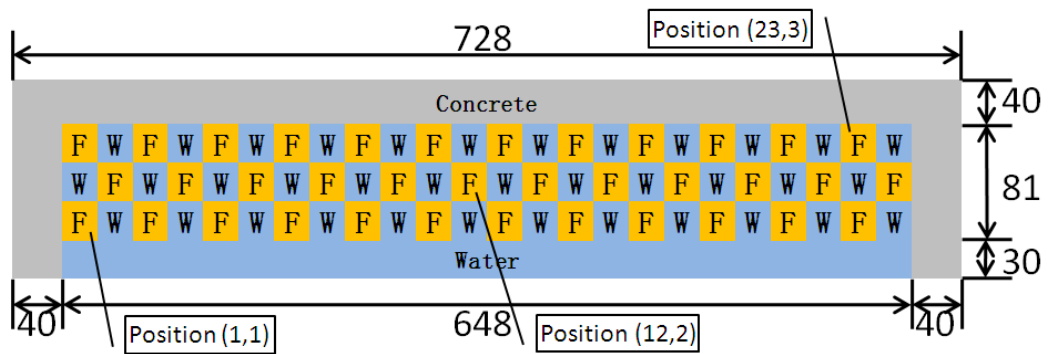
2.1 Benchmark Problems

In order to determine the capability of each convergence diagnostics method and compare their performance, the OECD (Organization for Economic Co-operation and Development) Nuclear Energy Agency (NEA) established an expert group on source convergence in criticality safety analysis. The first task of this group was to assemble several representative test problems⁸ that exhibit slow source convergence. The following four problems, which are used as benchmark problems, have been developed

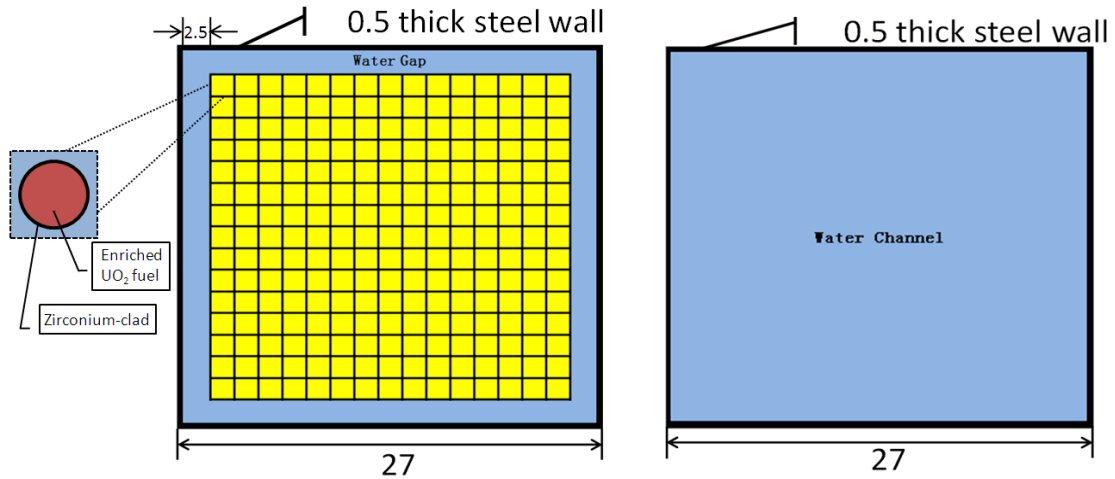
1. Checkerboard Fuel Storage Array
2. Pin-cell Array with Irradiated Fuel
3. Loosely Coupled Uranyl Nitrate Solution Slabs
4. Array of Interacting Spheres.

Among them, the first benchmark problem has been widely-used for the convergence diagnostics purpose. The system represents a fuel storage pool with a 24-by-3 array, surrounded by water layers and concrete walls.

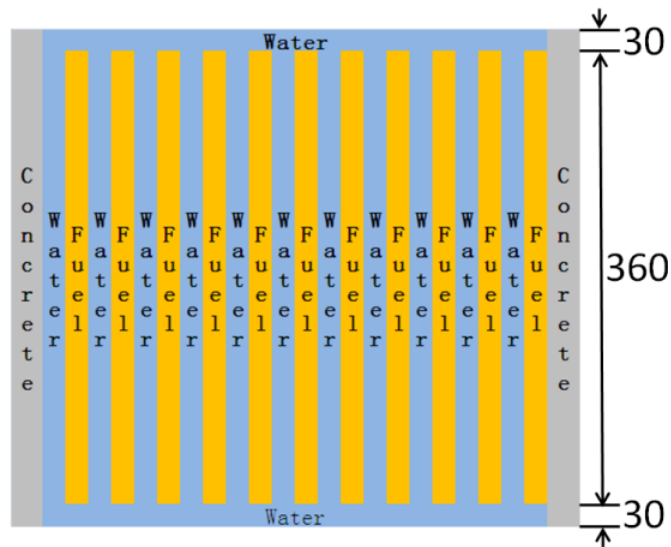
Figure 2.1 shows the geometric structure of the benchmark problem. The system contains 36 fuel elements with uranium enriched in ^{235}U to around 5.0% by weight. The lower left corner fuel assembly or unit is assigned as position (1, 1), with two indexes representing right and up directions. Therefore, all the other assemblies or units are identified by the same position format. For example, the right top corner assembly is denoted as position (24, 3). Besides these assemblies, the array of fuel assemblies is surrounded on three sides by concrete and on the fourth side by water, as shown in the figure. A layer of water is also above and below and in the gaps and channels between fuel assemblies. The fuel assembly is composed of a 1.44cm-pitch, 15-by-15 lattice. In the center of the fuel rod is a 0.44 cm-radius UO_2 fuel pin with 0.05cm-thick Zirconium-clad. Both the fuel and water assemblies have 0.5cm steel channel walls outside. The detailed atom densities for each part of the system are listed in **Table 2.1**. More detailed descriptions can be found in Ref. 8 and Ref. 9.



(a) Top view of the array



(b) Fuel element (with fuel pin) and water channel



(c) Front view from the center of the middle row with water in the top and bottom

Figure 2.1. Geometry specification of the storage fuel pool benchmark problem (unit in cm)

**Table 2.1. Material atom densities of the storage fuel pool benchmark problem
(atoms/10⁻²⁴ cm³)**

Element	Atom Density
Fuel	
²³⁸ U	2.2380e-02
O	4.6054e-02
²³⁵ U	8.2213e-02
Concrete	
H	5.5437e-03
C	6.9793e-03
Si	7.7106e-03
Ca	8.9591e-03
O	4.3383e-02
Water	
H	6.6706e-02
O	3.3353e-02
Iron	
Fe	8.3770e-02
Zirconium	
Zr	4.2910e-02

The description of the benchmark problem not only includes the geometry and material information, but also specifies parameters for simulations, such as initial source distributions, inactive and active number of generations or cycles, and the number of histories per generation. However, these parameters are not requirements; instead they are just guidelines intended to facilitate comparison of results. However, advances in

computational pose led us to modify these simulation parameters in order to better utilize this benchmark problem. However, before illustrating diagnostics results using the benchmark problem, the concept of each diagnostics method needs to be introduced first.

2.2 The Bounding Approach

One attempt that tries to determine the convergence of k_{eff} is to compare the evolution of k_{eff} from multiple bounding runs. In principle, a well-chosen initial source distribution will reduce the computational expense for the convergence. In other words, the bias or distance between the initial source distribution and the converged source distribution would determine the efforts needed for the convergence. Therefore, a poorly-chosen initial source distribution will require more efforts on the convergence, which should be avoided in real-life applications. However, certain special “poorly-chosen” initial source distributions could help to determine the convergence of k_{eff} if based on preliminary analyses or other pre-simulation knowledge one can determine the high and low reactivity regions. One simulation with the initial source concentrated in the high reactivity regions will lead to a higher estimate of k_{eff} at the non-converged period. Similarly, a simulation with the initial source concentrated in the low reactivity region will yield a lower estimate of k_{eff} in the transient period. In some occasions, using the uniform initial source distribution to approximate the lower estimates of k_{eff} is acceptable. This diagnostics method has been recently reintroduced as the “sandwich method” by Ref. 10. However, the bounding approach method may be a more appropriate name for this method.

In this reference, the authors include the storage fuel pool benchmark problem as an illustration example. They first simulated several independent runs with different concentrated initial source to determine the highest reactivity region, which is position (1, 3). This result is a consequence of the higher reflective ability of concrete compared with water. The corner with two sides surrounded by concrete has more neutrons reflected

back, so the multiplication factor in this corner is the largest among all positions. After determining the highest reactivity region, two independent simulations were performed to generate the sandwich bounding. One simulation employed initial sources concentrated in position (1, 3); and the other simulation employed initial source uniformly sampled from all fuel regions. The number of histories per generation was 20,000; and 0 inactive cycles and 2,000 active cycles were used to illustrate the evolution of the estimates of k_{eff} , as shown in **Figure 2.2**.

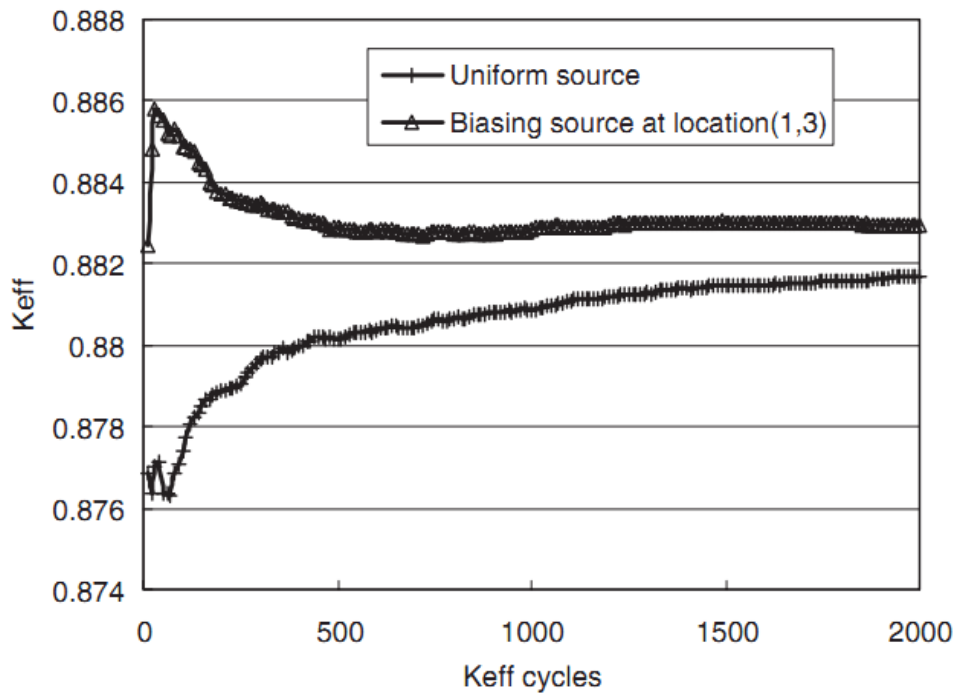


Figure 2.2. Bounding of the sandwich method example (Fig.6 from Ref. 10)

They claimed that the accurate k_{eff} is between the bounds. However, the gap between the two curves is still relative large after 2,000 generations, which demonstrate the slow convergence of the system again. In principle, any simulation with different initial source distributions should be converged if the gap between the upper bounding and the lower bounding are within some specified level, which in this case is much

smaller than the gap. Therefore, 2,000 generations are clearly not sufficient for this problem with these initial source distributions.

The problem with the bounding method is that it requires a prior knowledge or a preliminary analysis to determine the high and low reactivity regions, followed by multiple runs, which is not practical for real life application, but may be useful for analyzing benchmark problems.

2.3 Variance Comparison with Parallel Runs

Taking into account the capability of parallel runs, Shi and Petrovic¹¹ carried research in order to determine how many neutron generations it takes for k_{eff} to converge by comparing the relative variance of these parallel runs. They followed the original description of the benchmark problem about the initial source distributions. Four different source distributions were used to initialize four cases:

- Case 1 Uniform sources sampled over all 36 fuel assemblies
- Case 2 Uniform sources sampled over position (1, 1)
- Case 3 Uniform sources sampled over position (12, 2)
- Case 4 Uniform sources sampled over position (23, 3).

In addition, the number of histories was chosen to be 50,000 in order to cover the large loosely coupled system. Totally, they simulated the four cases for 15,000 active generations without any inactive generations. **Figure 2.3** shows the k_{eff} plots for the four cases. The 1σ error bars for the last 100 generations are also shown in the figure.

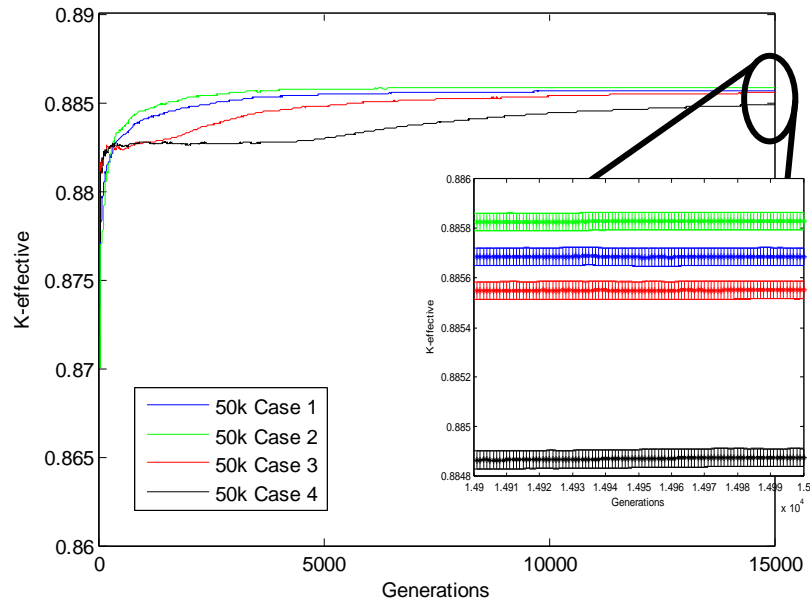


Figure 2.3. Evolution of k_{eff} for the four 50K cases without inactive cycles (Ref. 11)

Unlike the requirement of the sandwich method, the simulations in this reference does not include the case initialized with sources in the highest reactivity region, position (1, 3) in this problem. Despite this, the gap after 15,000 generations is still noticeable, especially for the comparisons involving case 4.

The authors again used the same data set, but treated the first 5,000 generations as inactive generations. **Figure 2.4** plots the similar results as **Figure 2.3** with only 10,000 active generations. The difference between the figures is because of the discarding of the initial non-converged estimates of k_{eff} . Still, the gaps after 10,000 generations are clearly showing the non-convergence of comparisons involving case 4.

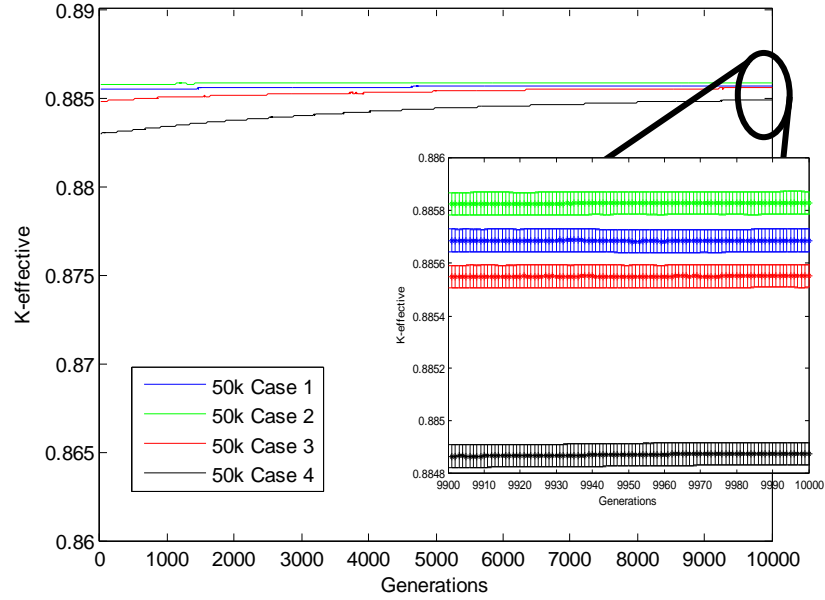


Figure 2.4. Evolution of k_{eff} for the four 50K cases with 5,000 inactive cycles (Ref. 11)

In summary, the bounding approach and parallel runs methods may be capable to indicate the non-convergence of k_{eff} . However, they require significant extra efforts, such as determination of the highest and lowest reactive regions, multiple independent simulations, and different choices of inactive generations. Moreover, relying on k_{eff} convergence to ascertain the convergence of flux distribution is not convincing. Therefore, these methods are inefficient and unreliable for real-life calculations.

2.4 The Shannon Entropy Indicator

In order to utilize the flux distribution, the Shannon entropy concept is introduced¹² to represent the condition of convergence. The entropy value H is defined¹³ as

$$H(S^B) = -\sum_{i=1}^B S^B(i) \log_2(S^B(i)). \quad (2.1)$$

In Eq (2. 1), B is the number of meshes used to divide the entire system; i is the index of each mesh; and $S^B(i)$ is the portion of source generated in the i^{th} mesh after certain cycle.

Therefore, this entropy value represents the entire flux distribution by only one value, which is easier for further analysis. Clearly, this entropy value is dependent on the simulations generations; in MCNP5¹⁴, which is a widely-used Monte Carlo simulation program for neutron calculation developed by the Los Alamos National Laboratory, it is employed as an indicator or warning for non-converged simulations.

In the user manual of MCNP5, the following paragraph describes the computation procedure of the entropy indicator

Upon completion of the problem, MCNP will compute the average value of H_{src} for the last half of the active cycles, as well as its (population) standard deviation. MCNP will then report the first cycle found (active or inactive) where H_{src} falls within one standard deviation of its average for the last half of the cycles, along with a recommendation that at least that many cycles should be inactive. Plots of H_{src} vs. cycle should be examined to further verify that the number of inactive cycles is adequate for fission source convergence. (MCNP — A General Monte Carlo N-Particle Transport Code, Version 5, Volume I: Overview and Theory)

The entropy indicator is intended to determine the non-convergence of the flux distribution, but the criterion used to determine the stationarity of the entropy value is questionable. Therefore, a visual check is frequently more reasonable for diagnostics purposes.

In Ref. 13, they applied the entropy indicator to the benchmark problem. They chose 50,000 histories per generation for 1,500 active generations without inactive generations. Two initial source distributions were used; one is a uniform source sampled over all fuel bundles; the other is a uniform source sampled over position (1, 3), which is the highest reactivity region. The mesh structure used to calculate the entropy is based on the fuel bundle structure: one mesh per fuel bundle. **Figure 2.5** shows the evolution of the cycle-wise entropy indicators for the two cases.

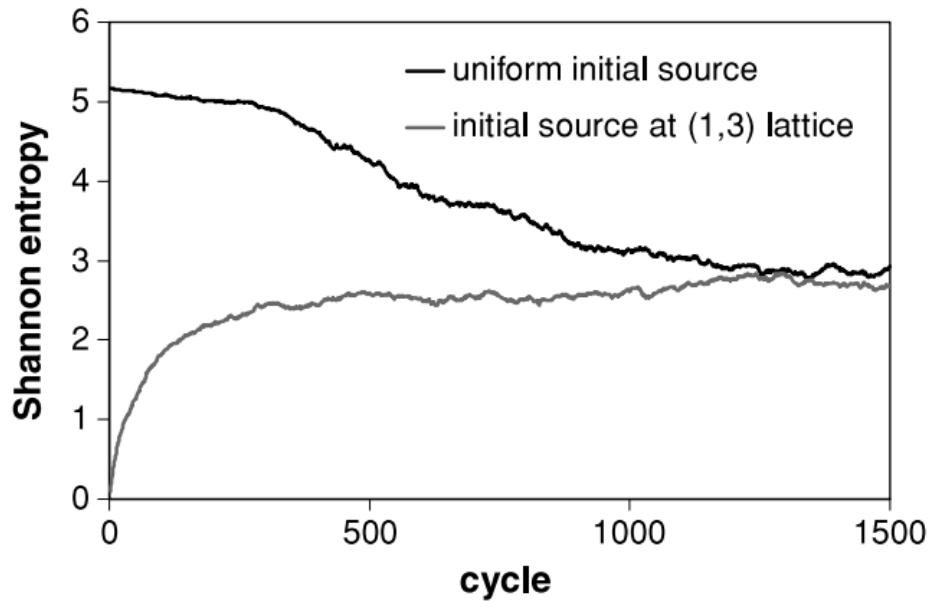


Figure 2.5. Cycle-wise entropies example (Fig. 14 from Ref. 13)

The entropy curve of the uniform initial sources case keeps decreasing throughout the entire 1,500 generations. Thus, they concluded that the flux distribution was not converged after 1,500 generations in this case. On the other hand, the other curve corresponding to the biased initial source distribution seems to be flat between 500th and 1,000th generations. However, this observation does not indicate the convergence of the flux distribution, because a slight jump appears after 1,000 generations. Although the entropy curve seems again flat after ~1,300 generations, convergence conclusion cannot be reached.

This incapability of the entropy indicator is due to the discarding of the local information. Although the computation of the entropy value first gathers the source distribution appearing in each mesh, it eventually condenses this information to one single value. Discarding this valuable information leads to the insensitivity to the slight change of the flux distribution, so this indicator cannot determine the convergence of the flux distribution. Therefore, the “convergence” result reported by the entropy indicator is

misleading because of the probability of the false positive diagnostics. To understand this limitation of the entropy indicator is important for real-life applications.

Despite this drawback of the entropy indicator, the bounding approach can be applied to the indicator plot in order to enhance the reliability. In Ref. 11, the authors plotted the entropy curves, which are shown in **Figure 2.6**, for the four cases described in **Section 2.3**.

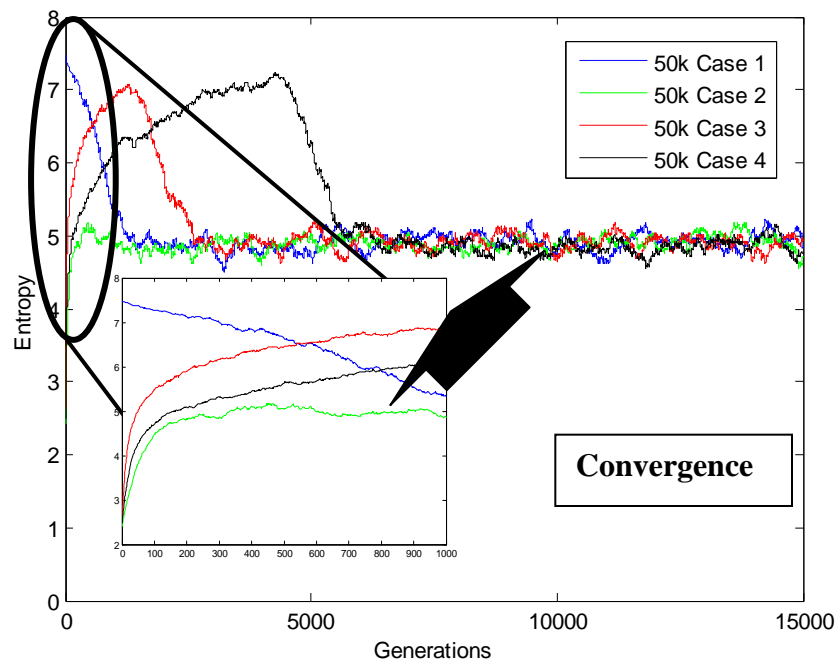


Figure 2.6. Evolution of the entropy values for the four 50K cases (Ref. 11)

At the beginning, the four curves are away from each other. After a while, they merge together and oscillate around certain number. However, if one examines in detail the apparent convergence of the flux distribution at the merging point, ~7,000 generations between case 4 and other cases, he will realize it is premature. In the reference, more information about the detailed mesh tally revealed that the flux distributions from case 4 and those from other cases were still statistically quite different. Therefore, the conclusion of convergence is questionable in this case. This example again demonstrates

the incapability of the entropy indicator to determine convergence of the flux distribution, although it may help to determine non-convergence of the flux distribution. In other words, it is susceptible to false-positive convergence indication, which is non-conservative and therefore of unacceptable.

2.5 Entropy-related Diagnostics Methods

Beside this incapability of the entropy indicator, other downsides are also investigated. As a result, several modified entropy-related diagnostics methods have been proposed. One disadvantage of the entropy indicator is that it lacks a reliable reference value to determine whether the current entropy value is close to it or not. The distance between two flux distributions is defined as a relative entropy¹⁶, which is also known as the Kullback Leibler distance. The expression of the relative entropy is in Eq. (2.2)

$$D(S^B | T^B) = \sum_{i=1}^B S^B(i) \log_2 \left(\frac{S^B(i)}{T^B(i)} \right), \quad (2.2)$$

in which $T^B(i)$ represents the normalized reference flux distribution. In Ref. 13, the authors also defined a so-called maximum stationary level (*mssl*) with certain pre-defined confidence level f . **Figure 2.7** shows the relative entropy plots for the same simulations described in **Section 2.3** from the reference.

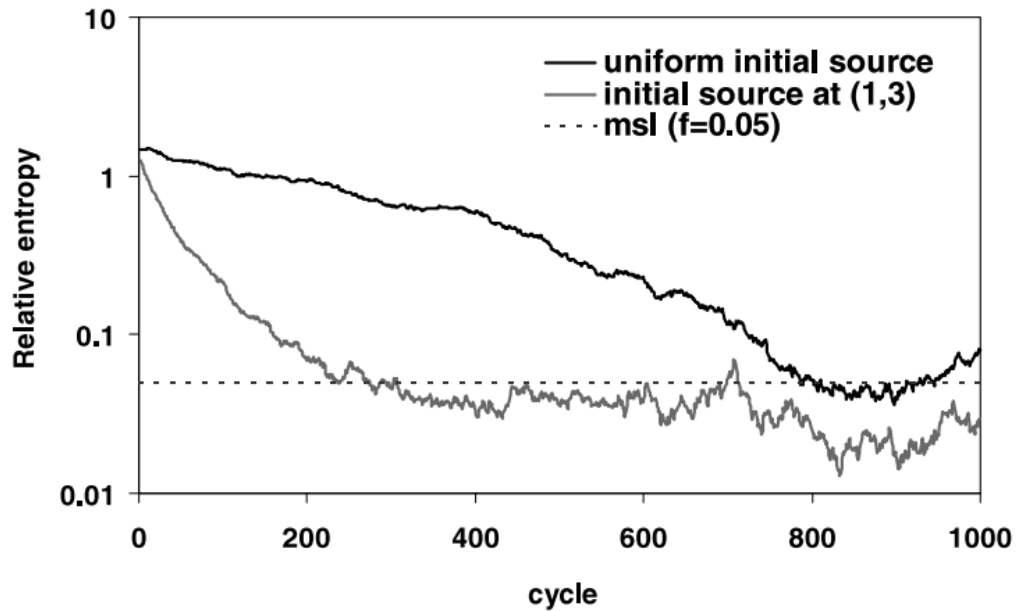


Figure 2.7. Posterior relative entropy example (Fig. 13 from Ref. 13)

The entire 1,000 generations was divided into 500 inactive generations and 500 active generations in order to provide the reference flux distribution. However, based on the analysis in **Section 2.3**, the crossing points in **Figure 2.7** cannot guarantee the convergence of the flux distribution. In other words, although this method could obtain the reference flux distribution, it still relies on the single simulation, which does not resolve this difficulty fundamentally. However, this quantity does provide a tool to measure the distance of two flux distributions, which is precious for further applications.

Another difficulty of the entropy indicator is that it is a posterior diagnostics method. Diagnostics results can only be obtained after the entire simulation. If the indicator reports non-convergence conclusion, re-simulation of the problem from very beginning is necessary. This difficulty is harmful to the efficiency. In Ref. 13, the authors proposed to introduce the concept of progressive relative entropy (*PRE*) with respect to the first active cycle, defined as Eq. (2.3) to assist the diagnostics.

$$PRE = D(S_1^B | \frac{S_1^B + S_j^B}{2}) + D(S_j^B | \frac{S_1^B + S_j^B}{2}) \quad (2.3)$$

In Eq. (2.3), S_1^B represents the fission source distribution at the first active generation; index j represents the progressive relative entropy value for the j^{th} active generation. The criterion for the convergence diagnostics is PRE smaller than $2 * msl$.

In the same reference, two figures are used to illustrate the effects of PRE . **Figure 2.8** shows the PRE plots for the two cases with respect to the first cycle; in other words, no inactive cycles are assigned. The curve corresponding to the uniform initial sources clearly shows an increasing trend, which indicates the non-convergence. The other curve corresponding to the biased initial source distribution, however, shows a rough flat trend after ~ 300 generations. However, due to the previous analysis, this observation could not lead to the convergence conclusion.

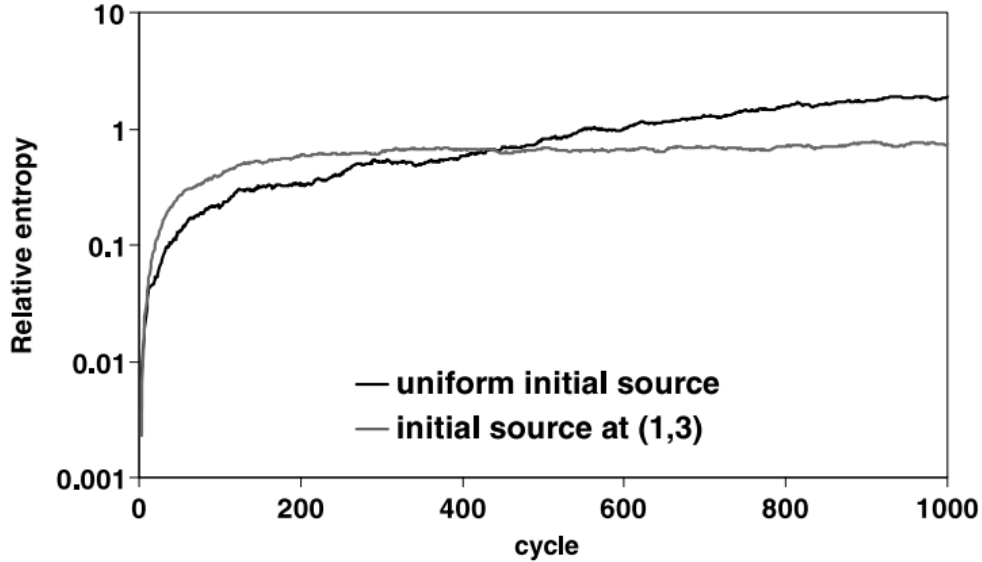


Figure 2.8. PRE with respect to the first cycle example (Fig. 11 from Ref. 13)

Figure 2.9 shows PRE plots with respect to the 501th cycle; in other words, 500 inactive cycles are assigned. This figure indicates similar conclusions: non-convergence

of the flux distribution for the case with uniform initial sources even after discarding 500 generation. On the other hand, *PRE* for the case with biased initial sources stays under the $2*msl$ line all the time, but to conclude the convergence by this observation is hazardous due to the arguments in previous sections.

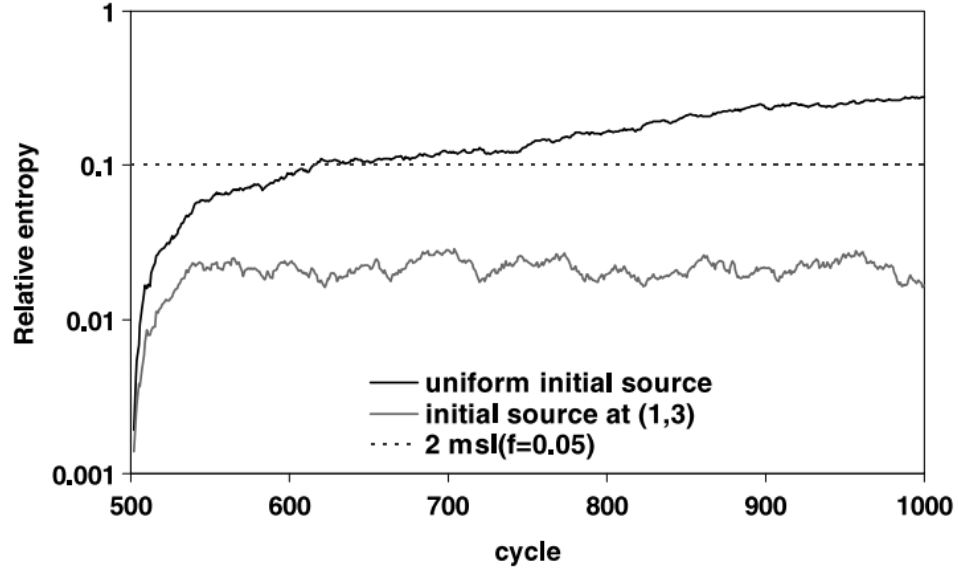


Figure 2.9. *PRE* plots with respect to the 501th cycle example (Fig. 12 from Ref. 13)

2.6 Combined KPSS Method

Because of the drawbacks of the entropy indicator and entropy-related diagnostics methods, other researches aimed to combine other potential diagnostics method with the entropy indicator in order to take advantage of its merits. The combined KPSS (Kwiatkowski-Phillips-Schmidt-Shin) method¹⁶ could work with the entropy indicator together in order to increase the reliability of the convergence diagnostics. According to the definition, a time series y_t is expressed as

$$y_t = \alpha + \beta t + d \sum_{i=1}^t u_i + \varepsilon_t, \text{ where } t=1, \dots, T. \quad (2.4)$$

In Eq. (2.4), u_i and ε_t are covariance stationary and short memory with mean zero; and coefficient d is between 0 and 1. The first two terms represent the linear behavior of the time series; the third term represents the random walk effect of the time series; and, the last term represents the stationary error component.

Table 2.2. Null hypothesis conditions of the KPSS test

Hypothesis	Condition
H_τ : trend stationarity	$d=0$
H_μ : level stationarity	$d=\beta=0$
H_o : zero mean stationarity	$d=\beta=\alpha=0$

Different hypothesis testing can be applied to the time series based on different null hypothesis. **Table 2.2** summarizes the conditions for different null hypothesis. The test statistic is defined as

$$w = \frac{1}{T^2} \sum_{t=1}^T \frac{S_t^2}{\sigma_\varepsilon^2}, \quad (2.5)$$

which can be estimated by

$$w = \frac{1}{T^2} \sum_{t=1}^T \frac{S_t^2}{\hat{\sigma}^2}. \quad (2.6)$$

In these equations, S_t is partial summation of the residuals of a linear regression; and σ^2 is the estimated long run variance, which needs a sophisticated estimation method to be accurate. Under the level stationarity (H_μ), w will converge to the first level Brownian Bridge; and under the trend stationarity (H_τ), w will converge to the second level Brownian Bridge. Different significance levels correspond to different values to reject the null hypothesis.

The time series the authors used is the center of mass (COM), which is defined as

$$|\vec{R}_g| = \frac{1}{M} \sum_{i=1}^{npg} m_i |\vec{r}_i|. \quad (2.7)$$

In Eq. (2.7), g is the generation index; npg is the total number of histories per generation; M is total mass; m_i is the mass of i^{th} history; and r_i represents the position of i^{th} history. In Ref. 17, the authors applied the KPSS diagnostics method to the benchmark problem. They simulated an extreme case with 1,000,000 particles per generation for 2,000 inactive cycles and 5,000 total cycles; and the simulation passed the entropy check but failed the KPSS test. However, this does not mean that the KPSS diagnostics method is much better. The author emphasized that it is best to combine the KPSS method with the entropy indicator in order to enhance the reliability of the diagnostics results.

The KPSS diagnostics method utilizes the COM as the testing time series data, but it can be actually extended to any time series, such as the entropy values and k_{eff} estimates. Nevertheless, it still relies on certain condensed quantities instead of taking advantage of local information. Therefore, this limitation may affect the reliability of the KPSS method. Moreover, the theory basis for the KPSS method is complex, which makes reliable uses difficult.

2.7 Statistical Diagnostics with Mesh Sources

Realizing the significance of the local information, Shim and Kim¹⁸ introduced a statistical diagnostics method based on mesh sources. They defined the mesh-wise fission source intensity as S_m^n , where m is the mesh index and n is the cycle index. As a result, the source convergence is determined based on the relative difference of the mesh-wise source intensities with $L(>0)$ cycles as

$$\frac{S_m^t - S_m^{t-L}}{S_m^{t-L}}. \quad (2.8)$$

The standard deviation of this relative difference can be estimated by complicated mathematical deduction, and represented by σ_S . Moreover, a constant κ is used to

represent the significance level of the diagnostics, which can be chosen as 1, 2, and 3, under normality assumption. Therefore, the convergence of the source intensity in m^{th} mesh can be obtained if

$$\frac{S_m^t - S_m^{t-L}}{S_m^{t-L}} \leq \kappa \sigma_S. \quad (2.9)$$

As a result, the global convergence conclusion can be achieved after verifying all the wish-wise convergence.

This method faces three unresolved difficulties. The first one is the assumption of normality of the mesh intensities, which is not proved by any analysis. Another difficulty is choosing an appropriate L , in order to avoid either premature (false-positive) convergence indication or inefficiency of too many unnecessary generations. In their examples, they divided the system into only 10 regions, which may be too small to capture all the detailed local information. The applicability of the method to systems with more meshes is still unclear.

Considering these difficulties, Shim and Kim¹⁹ updated the diagnostics method by using more sophisticated method to estimate the variance and covariance of the relative intensities. In addition, they proposed one formula to give an optimal L for the computation. Despite these efforts, they still did not resolve the difficulties fundamentally. More testing problems or examples are still necessary in order to validate this diagnostics method. However, the top level approach to the convergence diagnostics by investigating local source distribution is still valuable for later research, especially for the purpose of this dissertation.

CHAPTER 3

LINEAR REGRESSION DIAGNOSTICS METHOD

The purpose of this research topic is to propose an innovative convergence diagnostics method based on local information or local flux distribution. Instead of condensing the detailed information into one or several quantities (such as k_{eff} or entropy), the diagnostics method should observe and maintain mesh-wise information. The diagnostics method in Section 2.6 is also inspiring in terms of the relation between local convergence and global convergence. If the convergence can be determined in each local mesh with sufficient local information, the global convergence can be guaranteed as a consequence. Therefore, the first task is to propose an approach to determine the convergence within any single mesh. One point needs to be noted is that in deterministic methods, the determination of convergence is generally simple; however, for the Monte Carlo method, due to the randomness, the convergence diagnostics becomes a major issue.

3.1 Ordinary Linear Regression Model

The ordinary linear regression model²⁰ seems to be appropriate for this purpose. In this model, X_i represents the predictor and Y_i represent the observation accordingly, which is called responder. These predictors and responders should be independent in order for the model to be valid. The relation between the predictor and responder is assumed to be linear under this model as

$$Y_i = \beta_0 + \beta_1 \times X_i + \varepsilon_i. \quad (3.1)$$

In Eq. (3.1), β_0 is the constant term and β_1 is the linear coefficient. In addition, ε_i is an independent random error term generally following a normal distribution $N(0, \sigma^2)$. In all, three unknown parameters, β_0 , β_1 , and σ^2 need to be determined or estimated in order to fully describe this linear regression relation.

The estimations of these parameters are based on observations. For n sets of observations from (x_1, y_1) to (x_n, y_n) , the least square estimator of the linear coefficient β_1 is

$$\hat{\beta}_1 = \frac{\sum_{i=1}^n (x_i - \bar{x})(y_i - \bar{y})}{\sum_{i=1}^n (x_i - \bar{x})^2}, \text{ where } \bar{x} = \frac{\sum_{i=1}^n x_i}{n} \text{ and } \bar{y} = \frac{\sum_{i=1}^n y_i}{n}. \quad (3.2)$$

In addition, the least square estimator of the constant coefficient β_0 is

$$\hat{\beta}_0 = \bar{y} - \hat{\beta}_1 \times \bar{x}. \quad (3.3)$$

Associated with these estimators, the standard deviation of $\hat{\beta}_1$ is

$$\sigma(\hat{\beta}_1) = \frac{\hat{\sigma}}{\sqrt{\sum_{i=1}^n (x_i - \bar{x})^2}}, \quad (3.4)$$

where $\hat{\sigma}$ is the estimator of the standard deviation of the normal distribution, which describes the behavior of the error term ε_i . This estimator is given by

$$\hat{\sigma}^2 = \frac{\sum_{i=1}^n (y_i - \hat{\beta}_0 - \hat{\beta}_1 \times x_i)^2}{n - 2}. \quad (3.5)$$

With these formulas, the entire model can be fully described with these estimators.

3.2 Hypothesis Testing of the Linear Regression Model

The cycle-wise volume flux estimates in any single mesh could serve as responders. The predictors of this model could be assigned as integers from 1 to n . Therefore, if the observed flux estimates are from a converged flux distribution, no linear term should be observed after fitting the data set accordingly. In other words, the estimated β_1 should be around zero. As a result, the hypothesis test

$$H_0: \beta_1=0 \text{ vs. } H_a: \beta_1 \neq 0$$

can be used to determine the relative amplitude of the linear coefficient. The null hypothesis for this test is that β_1 equals zero, so no linear relation exists between the

predictors and responders. The null hypothesis will be accepted if there is not enough evidence to reject it. However, if there are sufficient evidences to reject the null hypothesis, the alternative hypothesis that β_I not equaling zero will be accepted. As a result, the linear relation would be confirmed, so the cycle-wise flux estimates are not converged.

The test statistic is defined as a t-value

$$t = \frac{\hat{\beta}_1}{\sigma(\hat{\beta}_1)}, \quad (3.6)$$

which follows a t-distribution with $n-2$ degrees of freedom. If the t-value is greater than the $1-\alpha/2$ quantile of the standard t-distribution, $t_{1-\alpha/2, n-2}$, the null hypothesis will be rejected. On the other hand, if the t-value is smaller than the $1-\alpha/2$ quantile, the null hypothesis will be accepted.

3.3 Diagnostics Procedure for Monte Carlo Simulations

Applying this procedure could determine the convergence of the cycle-wise flux estimates. In a real-life application, assuming the total number of generations in Monte Carlo simulation is N , the regression size of the data set n needs to be specified beforehand. To determine when the flux estimate has converged, this diagnostics method is first applied to the first n estimates. If the null hypothesis is rejected, the first estimate will be deleted from the data set. In the meantime, the next estimate outside the previous data set will be included into the data set to maintain the total number of estimates to be n again. This moving window technique continues until the null hypothesis is accepted. At that time, the index of the next generation outside the data set will be reported as the converged point of the cycle-wise flux estimates.

For one nuclear system, the number of meshes used to divide the system should be sufficient to maintain the local information, but the number should not be too large based on two reasons: the computational efforts proportional to the number of meshes

will be costly with too many meshes; and with larger number of meshes, the size of each mesh will be small, so the uncertainty associated with each mesh will be undesirably large. The diagnostics method will be performed in each mesh, and the global convergence can only be guaranteed after all the cycle-wise mesh-based flux estimates are converged. In addition, several initial generations should not be included into the data set because of the inaccurate initial guess of k_{eff} . The choosing of the significance level α and regression size n will be discussed in later sections, after the first example.

3.4 One-dimensional Test Example

The first example²¹ used to illustrate the procedure of the linear regression diagnostics method is a simple one-dimensional, one energy group problem with three regions. **Figure 3.1** shows the geometry structure of this system; the left and right boundaries of the system are located at -4.5cm and +4.5cm. The high reactive material (HRM) fills the -4.5cm to -2.0cm and +2.0cm to +4.5cm regions; and the low reactive material (LRM) fills the central region between -2.0cm and +2.0cm. Vacuum boundary conditions are applied to both boundaries. Table 3.1 lists the material information for both HRM and LRM.

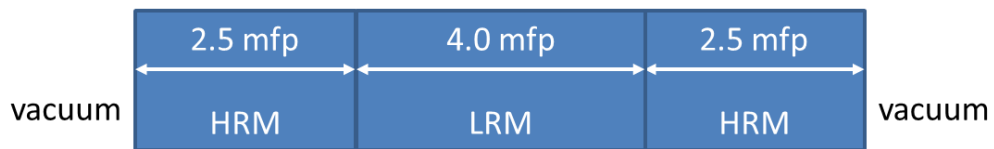


Figure 3.1. Geometry structure of the one-dimensional test problem for the linear regression model (Ref. 21)

Table 3.1. Material information of both HRM and LRM for the one-dimensional testing problem for the linear regression model (Ref. 21)

	HRM	LRM
Σ_t	1.0 cm ⁻¹	1.0 cm ⁻¹
Σ_c	0.1 cm ⁻¹	0.45 cm ⁻¹
Σ_s	0.8 cm ⁻¹	0.5 cm ⁻¹
$v\Sigma_f$	0.3 cm ⁻¹	0.15 cm ⁻¹
Σ_f	0.1 cm ⁻¹	0.05 cm ⁻¹
v	3.0	3.0

This problem exhibits the slow convergence difficulty because of the LRM in the middle of the system. As a result, the communication between the two HRM regions is weak. The Monte Carlo simulation employs initial source located at -4.0cm, so it may take a while for the simulated particles to travel through the LRM region and enter the HRM in the right half part of the system. It may take even longer for the entire flux distribution to converge as a result. The simulation uses 40,000 histories per generation for 400 generations without any inactive generations, because this mesh tally mechanism is used to determine the convergence instead of being used to estimate the desired tally. One hundred uniformly distributed meshes are used to divide the system and obtain cycle-wise mesh tally. The entropy indicator is also used to compute the cycle-wise entropy values and determine convergence in this manner as well. **Figure 3.2** shows the plot of the entropy indicator for this example, which indicates that the flux distribution is not converged for at least ~150 generations.

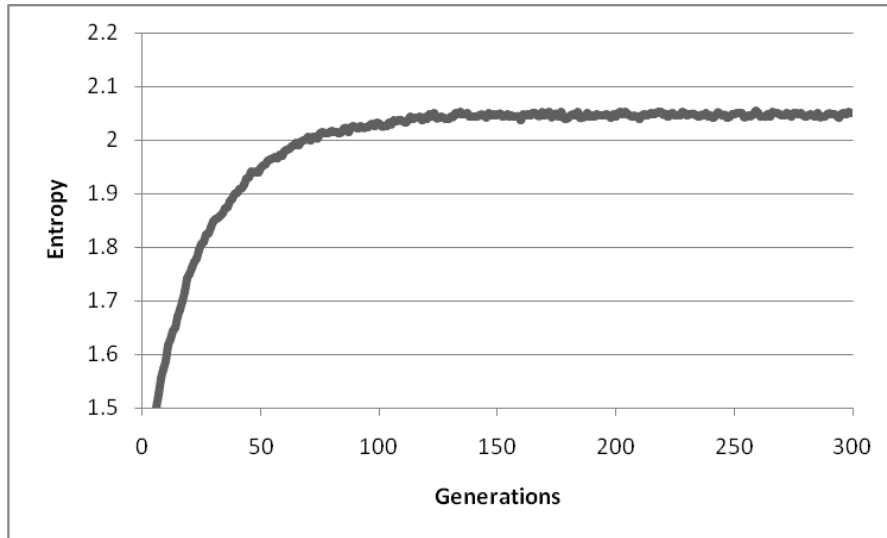


Figure 3.2. Evolution of the entropy values for the one-dimensional test problem for the linear regression model (Ref. 21)

In order to eliminate the initial effect, the first 10 generations are not included into the diagnostics data set. After that, the linear regression diagnostics method is applied to the cycle-wise mesh tallies first with a significance level $\alpha=0.10$. The regression size n is a variable in this case, which is chosen to be an odd number between 3 and 101. **Figure 3.3** plots the index of the first generation, when all the flux meshes have converged. In other words, this figure summarizes the diagnostics result with different regression sizes. Similarly, **Figure 3.4** gives the diagnostics results with different regression sizes under the significance level $\alpha=0.20$.

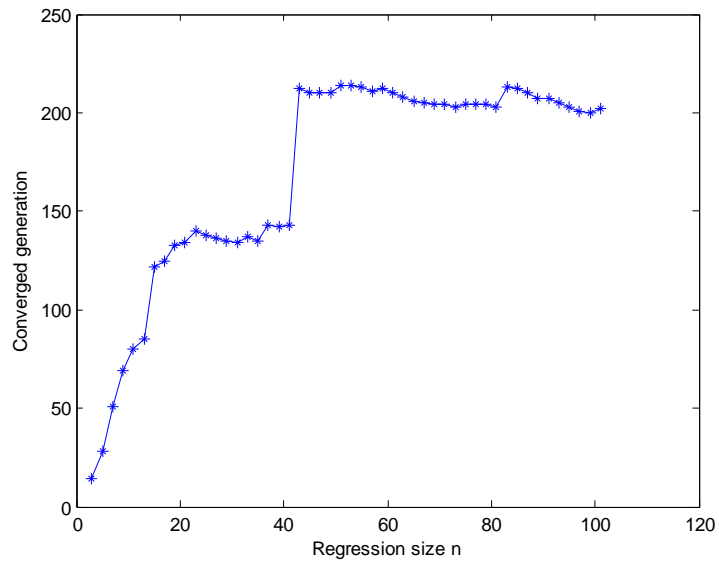


Figure 3.3. Converged generation for one-dimensional testing problem for the linear regression model with $\alpha=0.10$ (Ref. 21)

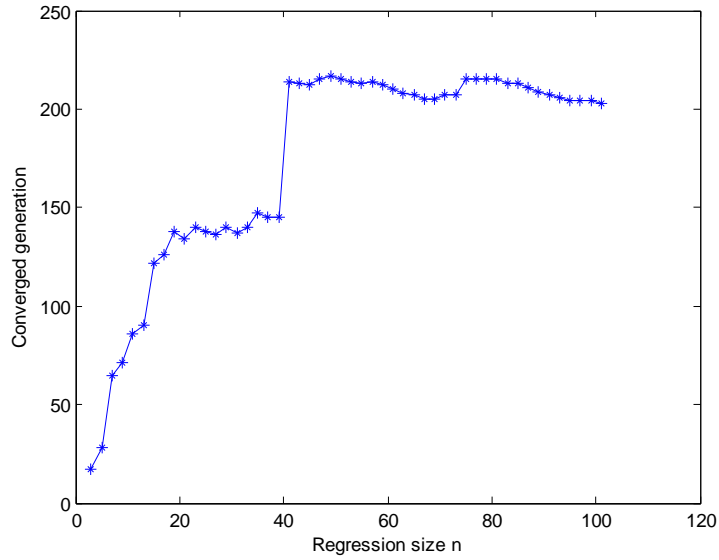


Figure 3.4. Converged generation for one-dimensional testing problem for the linear regression model with $\alpha=0.20$ (Ref. 21)

Observing these two figures reveals that when the regression size n is too small, in these cases smaller than ~ 50 , the predicted number of generations needed for convergence is increasing. Following by this period is a sudden jump, after which the diagnostics results remain roughly constant with regression size changing. The uncertainty of the estimated standard deviation depends on the size of the data set. The reliability of the t-value for a small set is less than that for a large set. Therefore, too small regression size should be avoided. Moreover, the insensitivity of the diagnostics result once the regression size is chosen to be large enough leads to robustness in real-life applications. Therefore, from these two figures, the convergence is reached after ~ 200 generations. This diagnostics result is consistent with the entropy indicator.

Another observation is about the impact of the significance level: a larger significance level will lead to slightly tighter diagnostics. In this case, the average magnitude of the flat region in **Figure 3.4** is slightly higher than that in **Figure 3.3**. This is because of the properties of the hypothesis testing, whose null hypothesis is $\beta_1=0$. In other words, before performing the hypothesis test, the null hypothesis is assumed to be accepted unless strong enough evidence says to reject it. One effect of this feature is that reducing the significance level is actually making the convergence criterion looser. However, since the tail part of the t-distribution is relatively small, changing of the significance level in the tail part should not affect the diagnostics results much. As a result, in real-life applications, a significance level equaling between 0.10 and 0.20 is in general acceptable. The other effect of the hypothesis test is that the diagnostics method is non-conservative and tends to make under-estimate of the convergence diagnostics.

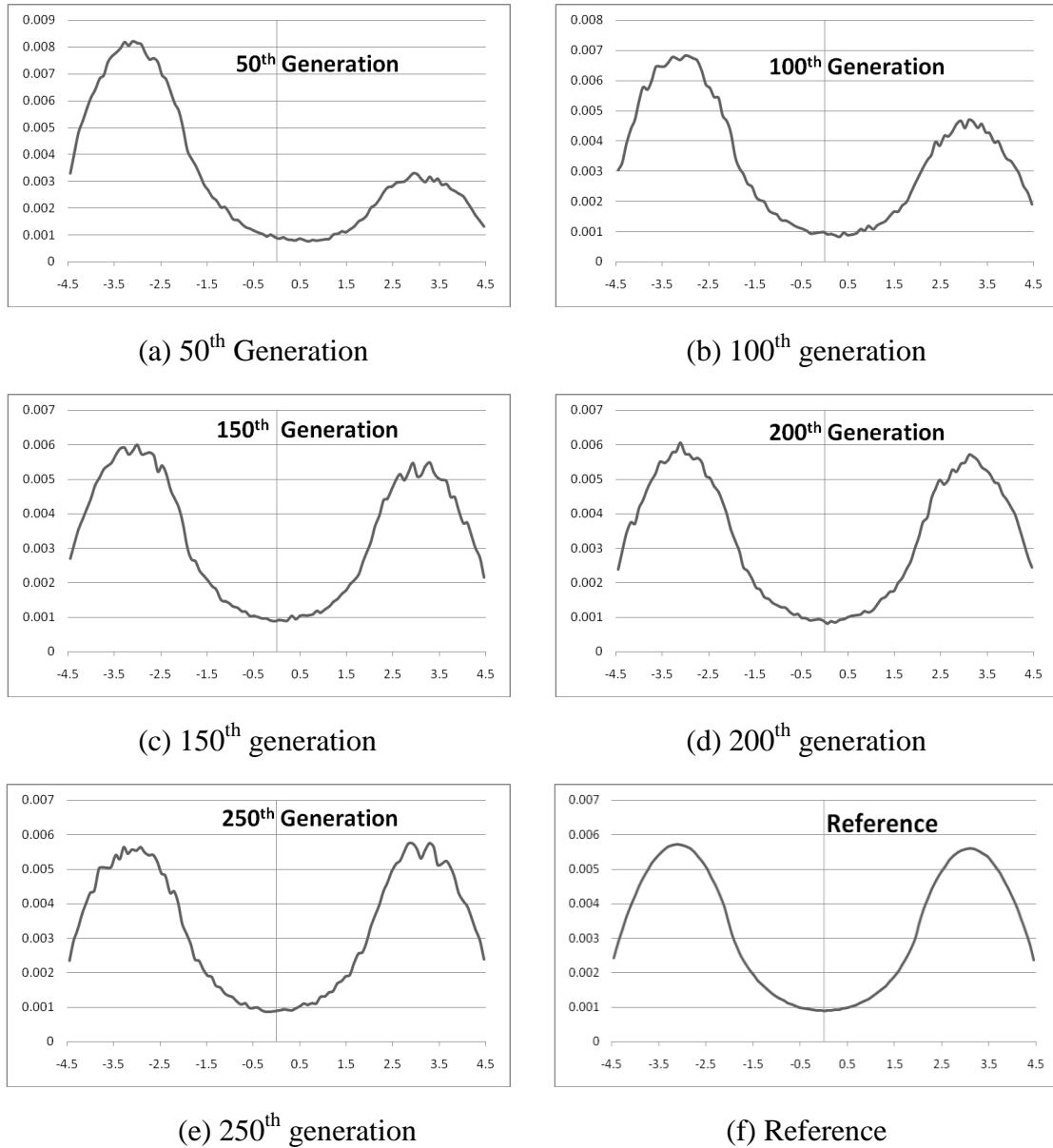


Figure 3.5. Changes of the flux distribution from different generations with a reference flux distribution for one-dimensional testing problem for the linear regression model

Until now, although several diagnostics results have been obtained, there is still no clear indication for the flux convergence. In order to illustrate the changing of the flux distribution, **Figure 3.5(a)-(e)** shows the flux distributions from the 50th, 100th, 150th, 200th, and 250th generations, respectively, while **Figure 3.5(f)** shows a reference flux

distribution from another simulation with 40,000 particles per generation with 500 inactive generations and 500 active generations. The changing trend of the flux distribution is quite clear. The mesh tally from the 150th generation still shows unequal peaks in the two HRM regions. However, the entropy indicator in this case fails to report this non-convergence. This difference is diminishing along with the simulation, and after 200 generations, this difference is even smaller and acceptable for tallying purpose. To verify this statement, a comparison between the flux distribution reported after the 250th generation and the reference flux distribution in terms of relative variance is listed in **Table 3.2**. 58 out of 100 meshes have relative differences of the fluxes smaller than 1σ ; and all of the meshes have relative differences of the fluxes smaller than 3σ . This is consistent with the standard normal distribution, which supports the conclusion that convergence has been achieved by 250th generation.

Table 3.2. Summary of the relative differences of the flux distributions between the 250th generation and a reference simulation for one-dimensional testing problem for the linear regression model

	$<1\sigma$	$<2\sigma$	$<3\sigma$
Number of meshes (out of 100)	58	92	100

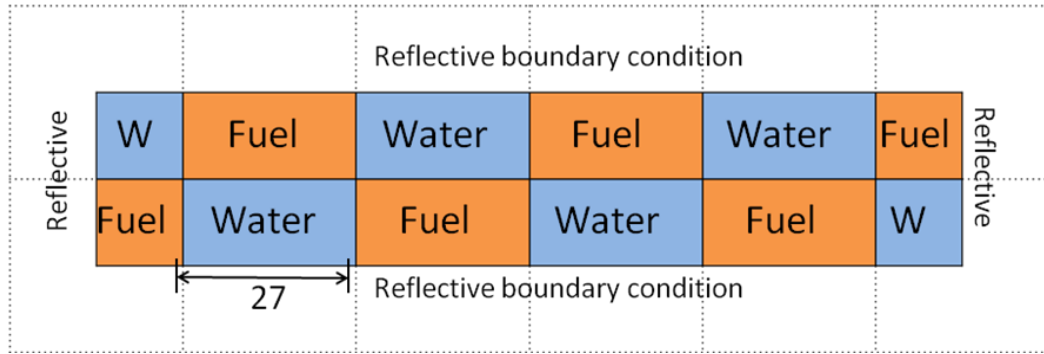
Therefore, the diagnostics result from the linear regression model is valid, and it performs more reliably than the entropy indicator as well. If considering the under-estimation effect due to correlation, mesh tally should be reported after additional inactive generations. In this case, 250 generations was selected rather than 200 generations as inactive generations before any tallying. From this figure, no noticeable difference exists between the two peaks, so the flux distribution seems converged by then.

This example is quite simple compared to three-dimensional, continuous energy problems. However, it provides a proof of principle and preliminarily demonstrates the

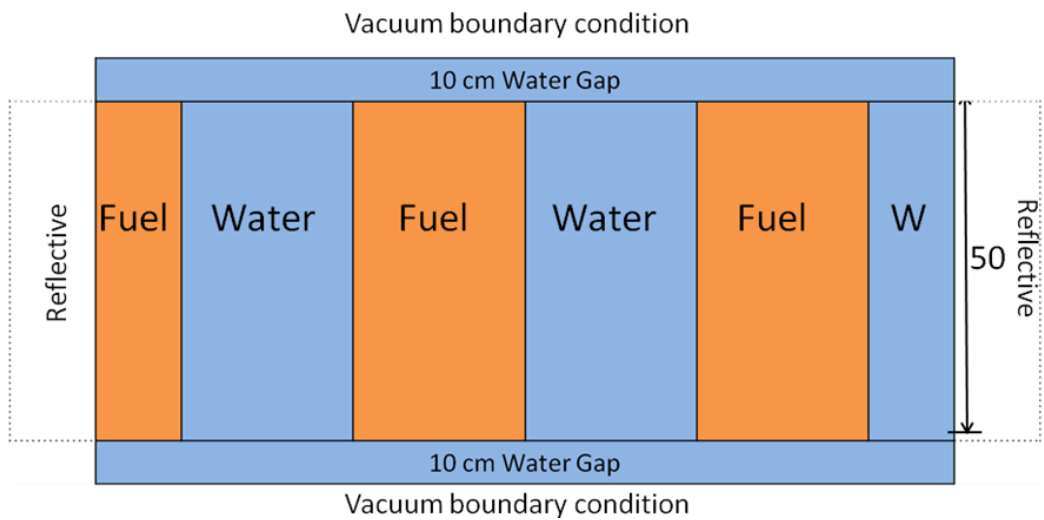
capability and advantages of the linear regression diagnostics method. This does not complete all the arguments about this method; more investigation and analysis are provided in the following examples and sections.

3.5 Simplified Benchmark Problem—50,000 Case

The second example to test the linear regression diagnostics method is a simplified OECD/NEA benchmark problem. This problem is based on the storage fuel pool benchmark problem but with a smaller size. Therefore, it still possesses some slow convergence issue, but the computational effort needed will be less than for the original problem. The geometry and components of the individual fuel assembly and water channel remain the same as shown in **Figure 2.1(b)**; while the geometry of the whole problem is shown in **Figure 3.6**. This system is composed of two rows of fuel assemblies and water channels, which are half the size of the original lattice structure due to the reflective boundary condition. The corner elements are only quarter size of the original lattice structure. All the four boundaries are reflective along this view direction to maintain the geometry property. Axially, the size of the fuel assemblies and water channels is shortened to 50cm with two 10cm-thick water gaps on the top and bottom with vacuum boundary conditions. The materials of the system remain the same as shown in **Table 2.1**. Thus, the volume of this system is about 100 times less than the original benchmark problem. This simplification reduces the difficulty of choosing an insufficient number of histories per generation and enhances the communication between different regions.



(a) Horizontal cross section view of the system



(b) Vertical front view of the system

Figure 3.6. Geometry of the simplified storage fuel pool benchmark problem (Ref. 21)

The Monte Carlo simulations are performed with MCNP5 with 50,000 histories per generation. Initially, 300 total generations are specified as the analysis data set. The initial source distribution is biased: radially, 99% of the initial source is uniformly sampled from the very left row of the system and only 1% of the initial source is sampled from the rest of the system; axially, all initial sources are sampled uniformly. This biased initial source distribution needs many generations to spread over the entire system and converge to the correct distribution. The system is divided into 150 meshes (10 by 3

radially, and 5 axially) for mesh tally and diagnostics purpose. As a reference **Figure 3.7** shows the entropy indicator plot of the simulation, which indicates that the flux distribution is converged after ~150 generations.

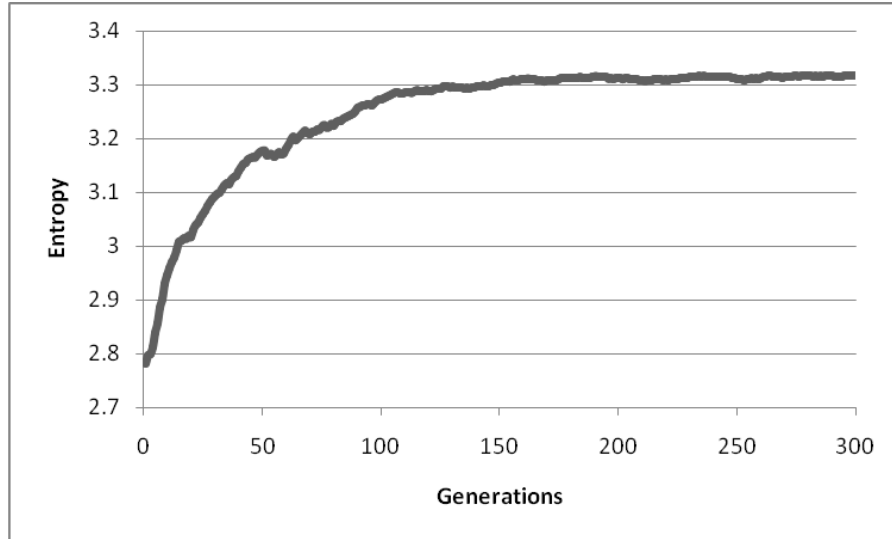


Figure 3.7. Evolution of the entropy values of the simplified benchmark problem for the linear regression model (Ref. 21)

The linear regression model is applied to this simulation as before. However, for some choices of regression sizes in this case, the mesh tally from 300 generations could not provide diagnostics. In other word, for these regression sizes, no t-value is smaller than the criterion for corresponding significance level. For now, these cases will throw a warning message indicating the insufficient data set. **Figure 3.8** shows the number of generations required for the flux distribution to converge under significance levels $\alpha=0.10$ and 0.20 . The regression size is chosen to be odd numbers between 3 and 85. Observations from this figure indicate that when the regression size is chosen to be large enough, in this case larger than ~40, ~155 generations are needed for the convergence, which is consistent with the entropy indicator. The diagnostics result with the significance level $\alpha=0.20$ is slightly tighter than that with $\alpha=0.10$, again.

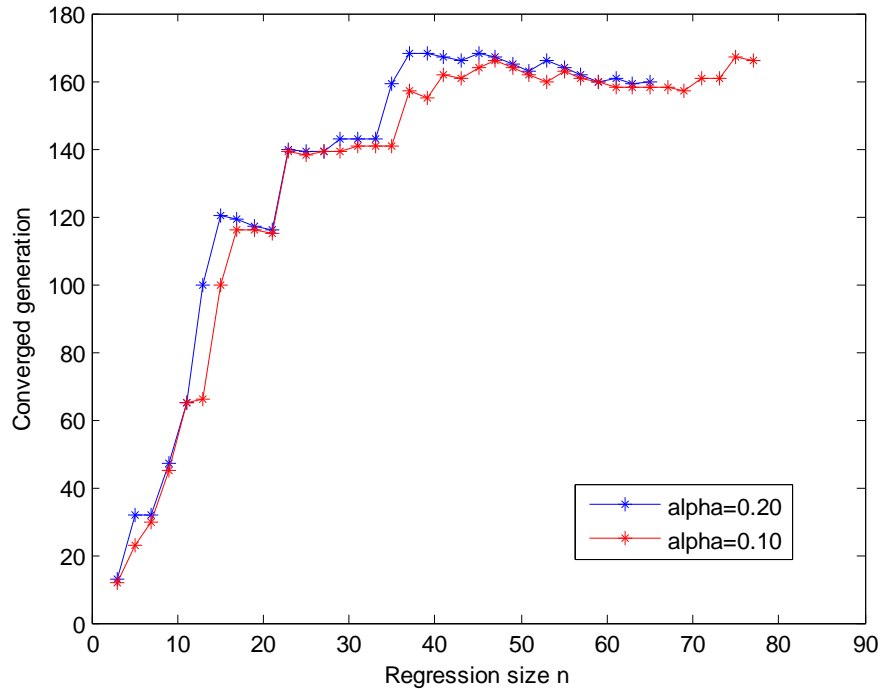
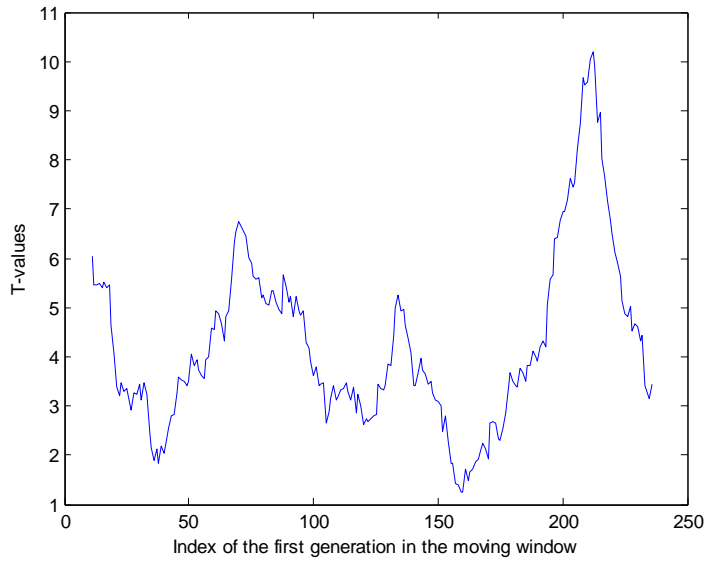
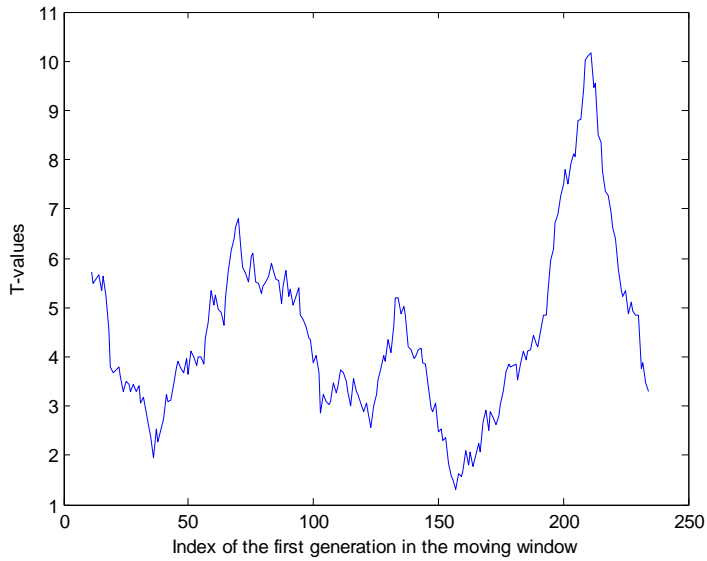


Figure 3.8. Converged generation for the simplified benchmark problem for the linear regression model (regression size n between 3 and 85)

One question needs to be answered in this case is the relation between the regression size and the amount of required data. From what regression size the diagnostics procedure requires for more data. Taking $\alpha=0.20$ case as an example, when the regression size is 65, it still reports valid diagnostics result, but when the regression size increases to 67, it flags the warning. Obviously, this change is caused by the change of t-values in some meshes, or even in one mesh. After investigation, mesh no. 138 is responsible for this change. Therefore, investigation of the behavior of t-values for $n=65$ and 67 in mesh no. 138 is necessary. **Figure 3.9** shows the corresponding evolution of t-values under these two regression sizes.



(a) T-values for regression size $n=65$



(b) T-values for regression size $n=67$

Figure 3.9. Changes of T-values for regression sizes $n=65$ and 67 with mesh no. 138 for the simplified benchmark problem for the linear regression model, under $\alpha=0.20$

The two curves in **Figure 3.9** both have minimal values when the index of the first generation in the moving window is slightly larger than 150. **Table 3.3** summarizes

these minimal values and corresponding criteria for significance level $\alpha=0.20$. The difference due to α value is much less than the difference between the minimal t-values. Thus, the root cause of the above warning is the changing of the t-values. Indeed, both **Figure 3.9(a)** and **(b)** show that after 150 generations, the t-values increase dramatically, which is the result of the statistical noise masking the actual (“average”) t-values. **Figure 3.10** shows the flux evolution of mesh no. 138. Clearly, a moving window with length ~ 60 generations starting from $\sim 150^{\text{th}}$ generation includes an almost flat data set. After ~ 230 generations, the flux increases again. This example shows the limitation of the regression model, especially the dependence of the regression size.

Table 3.3. Summary of the minimal t-values for regression sizes $n=65$ and 67 with mesh no. 138 for the simplified benchmark problem for the linear regression model, under $\alpha=0.20$

Regression size	Minimal t-value	Criterion
n=65	1.2414	1.2951
n=67	1.3055	1.2947

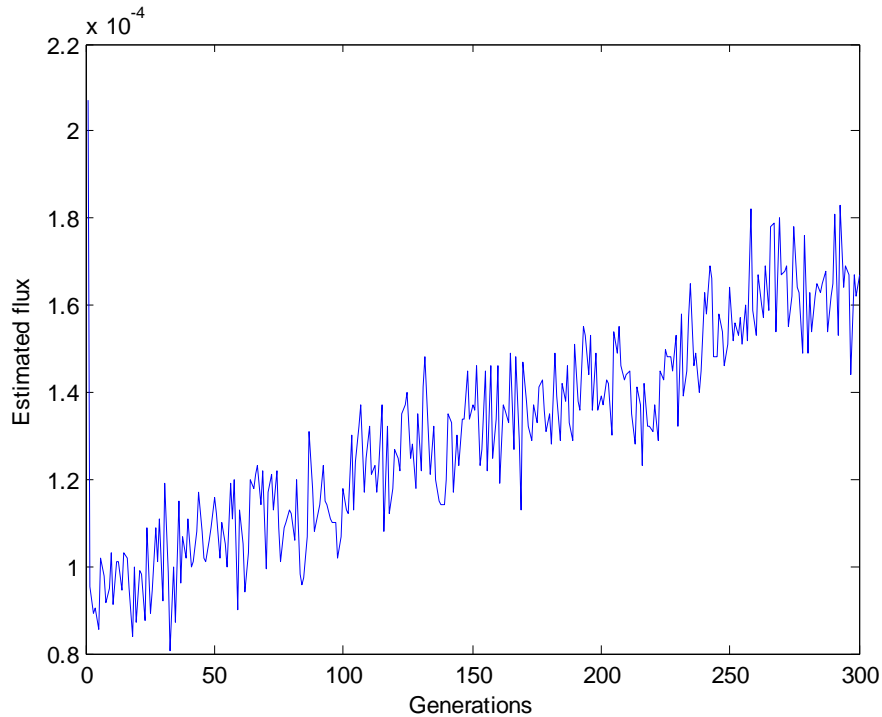


Figure 3.10. Evolution of the estimated flux in mesh no. 138 for the simplified benchmark problem for the linear regression model, up to 300 generations

In order to better understand this problem, the simulation has been continued up to 2,000 generations. **Figure 3.11** shows the extensive flux evolution in mesh no. 138. It shows large fluctuations of the flux estimate in this mesh. It is therefore difficult to determine the convergence of the flux distribution by examining mesh no. 138. Although it seems to be flat after ~1,600 generations, other observations from other meshes also show some trend after ~1,600 generations. One speculation of this behavior is due to undersampling. In this case, 50,000 histories per generation may not be sufficient for the system. Although the undersampling effect is not so severe in this case, it does cause noticeable local fluctuations larger than the change one would like to observe. This behavior violates the assumption of this diagnostics method that after convergence, the flux estimates in one mesh should oscillate around certain number within some small

interval. Therefore, the diagnostics method tends to report convergence for a relative flat interval of generations whose size is larger than the regression size.

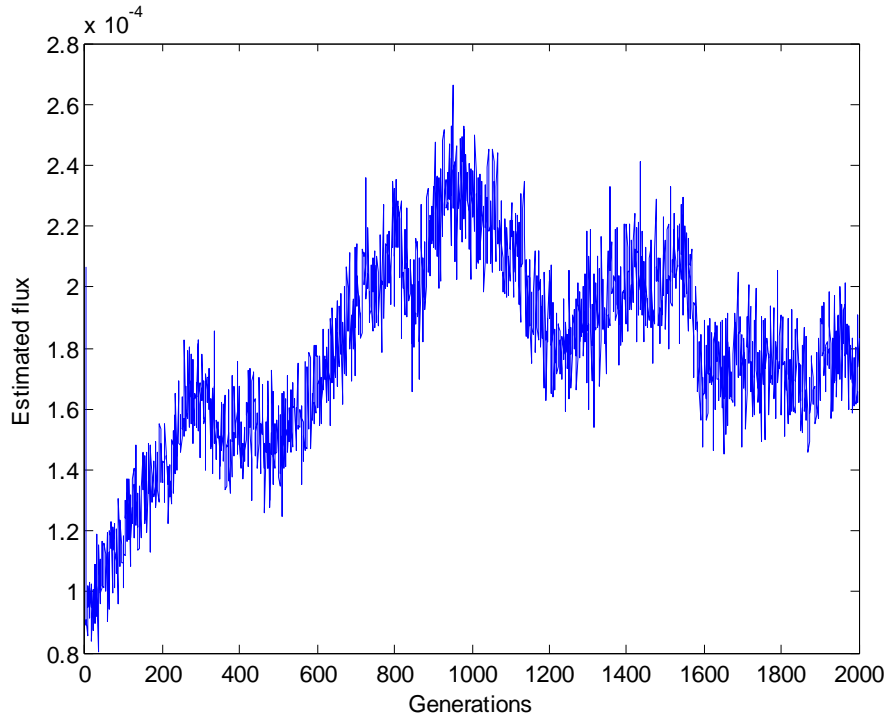


Figure 3.11. Evolution of the estimated flux in mesh no. 138 for the simplified benchmark problem for the linear regression model, up to 2,000 generations

With this larger data set, new diagnostics procedure is executed with regression size chosen as odd numbers from 51 to 151. **Figure 3.12** shows the corresponding suggested converged generation in this case. As a continuation of **Figure 3.8**, when the regression size is less than ~ 70 , the regression diagnostics method indicates the convergence as ~ 160 generations. When the regression size is between ~ 80 and ~ 120 , the suggested converged generation is ~ 250 . When the regression size is between ~ 120 and ~ 150 , the suggested converged generation is ~ 380 . This comparison explicitly demonstrates the role of the allowed regression size: it is the user expected length of generations with relatively flat flux estimates that will be accepted as convergence. In

other words, the user should have some idea about the period of random oscillations (noise) and specify the regression larger than that. Otherwise, the diagnostics method would give him the message when this criterion is by chance met for the first time.

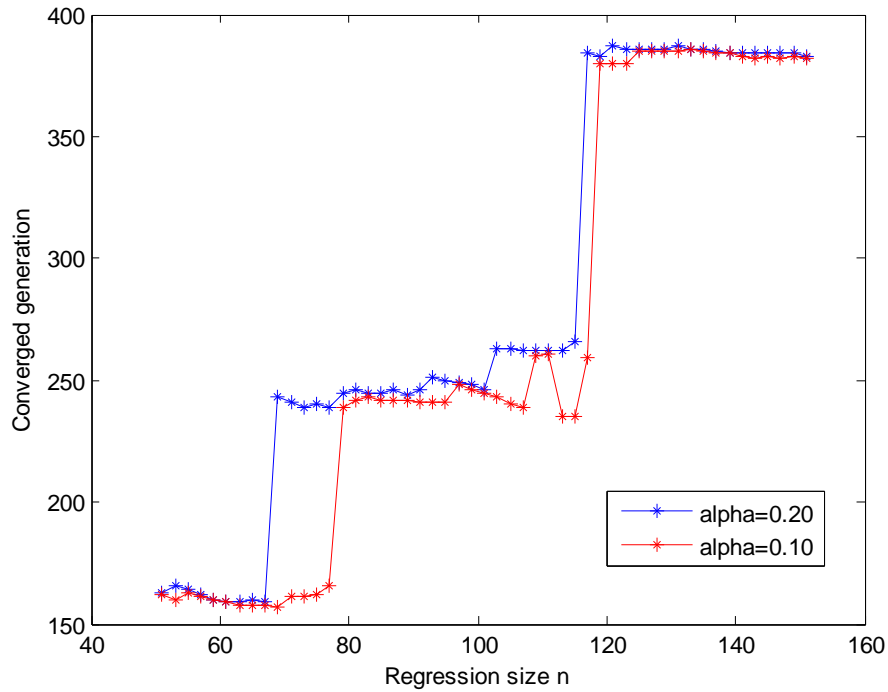
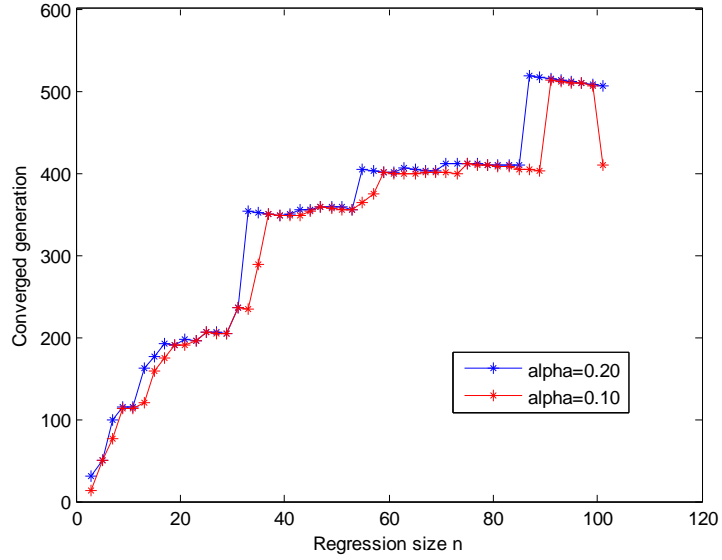


Figure 3.12. Converged generation for the simplified benchmark problem for the linear regression model (regression size n between 51 and 151)

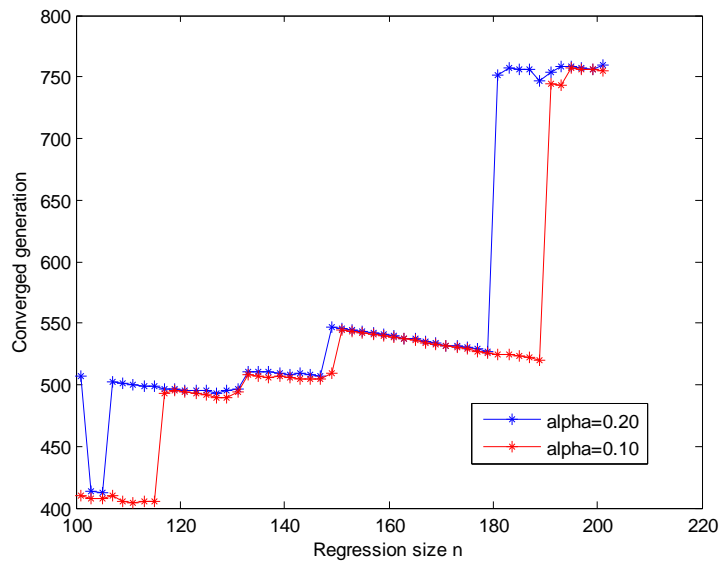
3.6 Simplified Benchmark Problem—500,000 Case

In order to reduce the undersampling effect, another run with 500,000 histories per generation is simulated for 1,600 total generations without any inactive generations. All the other parameters are the same as the previous run. **Figure 3.13** shows the suggested converged generations for this simulation when the regression size n is chosen to be odd numbers from 3 to 301. Along with the increasing of the regression size, the suggested number of generations needed for convergence is in general increasing as well.

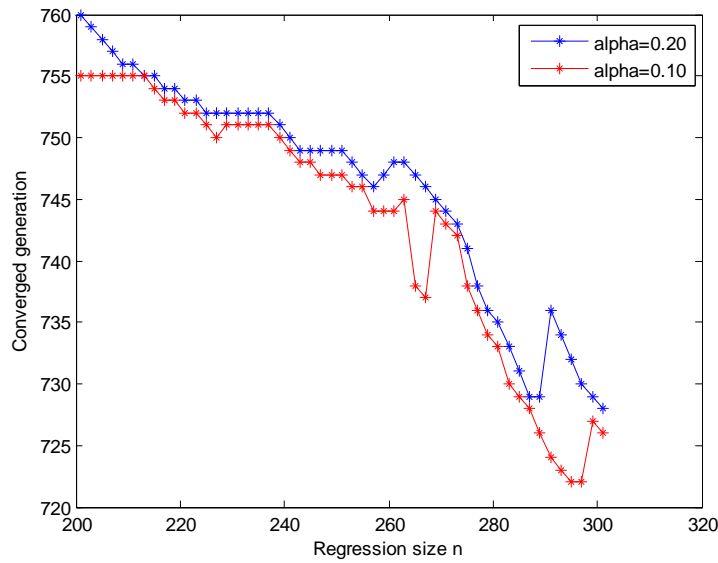
After each jump, a relative platform exists for some region of regression sizes, which is demonstrating the consistency of this method.



(a) Regression size n between 3 and 101



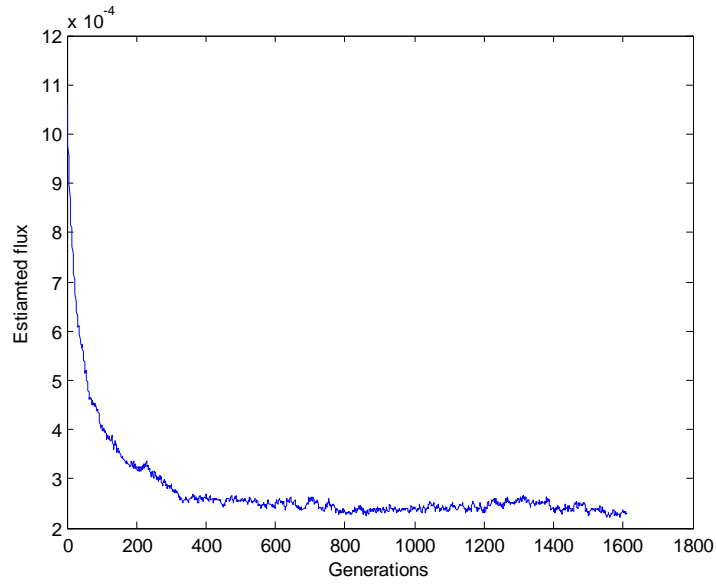
(b) Regression size n between 101 and 201



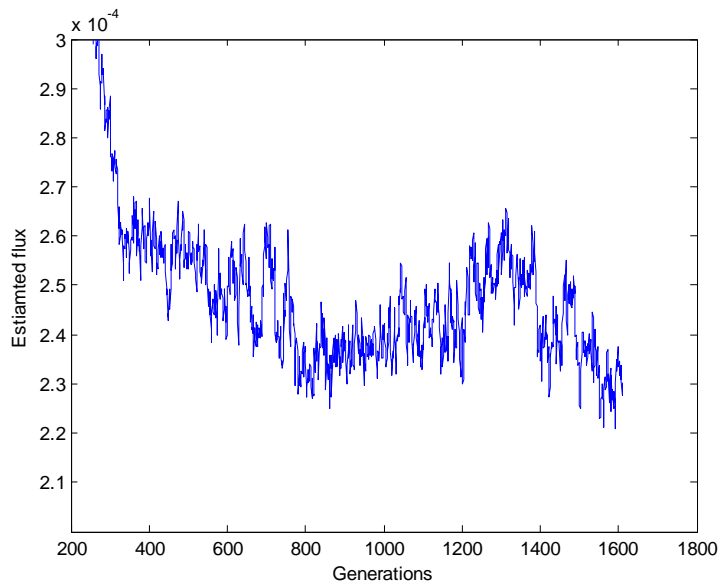
(c) Regression size n between 201 and 301

Figure 3.13. Converged generation for the simplified benchmark problem with 500K histories per cycle for the linear regression model (regression size n between 3 and 301)

The first mesh is actually responsible for the diagnostics results ~ 750 when the regression size is between 201 and 301. **Figure 3.14(a)** shows the flux evolution in the first mesh for this case. In order to illustrate the trend of the flux estimates, **Figure 3.14(b)** uses a different axis scale instead. From **Figure 3.14(a)**, it seems that the flux is converged after ~ 400 generations, despite the fluctuations. However, **Figure 3.14(b)** shows that the difference between the maximum and minimum after discarding the first 400 generations is about 15% of the average flux estimate. Compared to **Figure 3.11**, this fluctuation is moderate due to the fact of using more histories per generation, but still this may cause some premature false convergence.



(a) Original axis scale



(b) Amplified axis scale

Figure 3.14. Evolution of the estimated flux in mesh no. 1 for the simplified benchmark problem with 500K histories per cycle for the linear regression model, up to 1,600 generations

3.7 Auto-correlated Linear Regression Model

Previous analysis only focuses on the impact of the regression size, but another property, the independence assumption of the linear regression model needs to be addressed. The independence of the data set that validates the linear regression model is actually not satisfied because the flux estimates used as the responders are indeed dependent due to the inter-generation auto-correlation effect of Monte Carlo criticality simulations. As a result, the estimated standard deviation tends to be under-estimated, and eventually affects the t-values. Shi and Petrovic²² introduced the auto-correlated linear regression model in order to remove some of the auto-correlation effect from the linear regression model. The Hildreth-Lu method²³ is used to estimate the auto-correlation parameter, and then, the estimated auto-correlated components are removed from the data set. Therefore, an updated set of data is used for the diagnostics based on the linear regression model.

The same mesh tallies as in **Section 3.5** with 300 generations are used for the illustration purpose. **Figure 3.15** shows the comparison of the suggested converged generation from the ordinary linear regression model and this auto-correlated linear regression model (also called as transformed model) for regression size of the transformed model chosen as odd numbers from 5 to 71 and significance level $\alpha=0.10$. Due to the estimate of the auto-correlation parameter, the number of degrees of freedom for this model is $n-3$ instead of $n-2$ for the ordinary linear regression model given the same regression size n . **Figure 3.15** also includes the diagnostics results from the ordinary linear regression model by setting the auto-correlation parameter equaling zero in order to have the same number of degrees of freedom. This is the reason that the curve for the ordinary linear regression mode is slightly different than the curve in **Figure 3.8**. At each regression size, the transformed model requires less generations than the linear regression model does because the estimated variance is larger for the transformed model

after removing some underestimate effect. As a result, the t-values tend to be smaller and null hypothesis tends to be accepted with larger probability than before. However, this difference is insignificant with regression size not presenting jumps, compared to the reported converged generation.

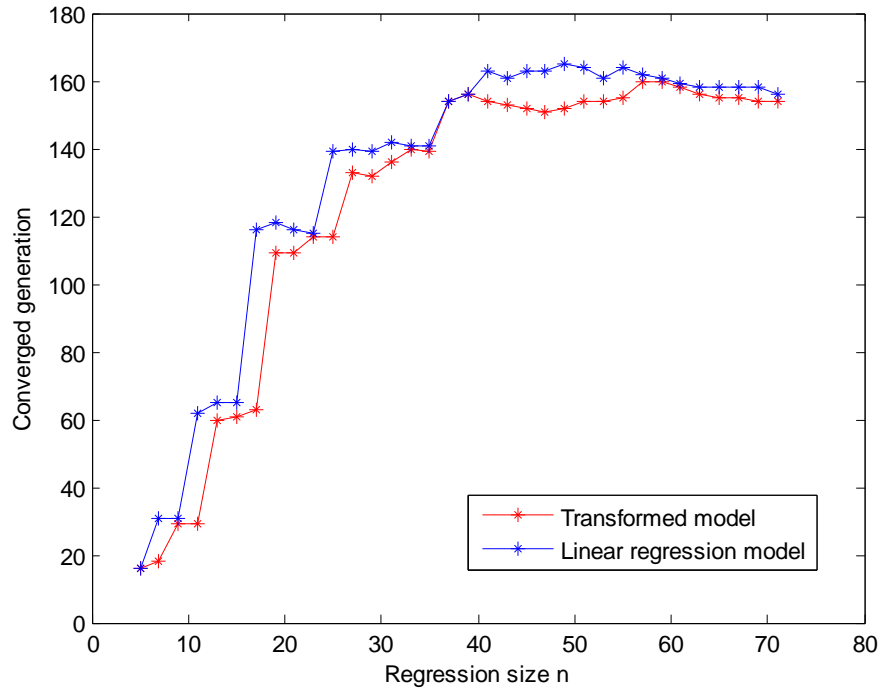


Figure 3.15. Comparison of the linear regression model and the transformed model for the simplified benchmark problem

In addition, the estimation and removal of the auto-correlation using the Hildreth-Lu method requires extra computational effort, which is more than the diagnostics based only on the linear regression model. Other sophisticated methods are also applicable in this case, but their requirements are even more costly. Based on these two reasons, the ordinary linear regression model is chosen to be the primary tool for the diagnostics purpose. While the expected benefit of auto-correlated regression method has not been

observed in this analysis, it should in principle provide more accurate results, and future work may try to establish conditions when its use would be justified.

3.8 Conclusions and Future Work

The linear regression model is utilized for the convergence diagnostics purpose based on the cycle-wise mesh tally. Two parameters need to be specified for the linear regression model, the significance level α , and the regression size n . The significance level, which represents the strictness of the diagnostics, could be chosen to be between 0.10 and 0.20 in general applications without significantly impacting the diagnosed number of generations to convergence. The maximum regression size is specified by the user as a criterion used when testing for the convergence. A larger regression size indicates a tighter convergence criterion and may lead to more generations required for the convergence. Future work should address automated selection of the regression size.

Two problems, a one-dimensional problem and a simplified benchmark problem, are used in this chapter to illustrate the diagnostics procedure and results. For the simple problem, a relatively large regression size and a reasonable significance level result in a comparable conclusion with other convergence indicators, such as the entropy indicator. In complex problems, the undersampling effect, and locally auto-correlation effect may be noticeable. Therefore, the diagnostics mainly depends on the regression size. The acceptable regression size magnitude still has to be determined by the user experience. This auto-correlation could be partially removed by using sophisticated tools. However, these tools have not noticeably improved the diagnostics and usually are computationally costly. Moreover, the removal of the auto-correlation effect tends to give larger variance estimate in the denominator of the t-value. Therefore, the transformed model provides looser diagnostics compared to the ordinary linear regression model, which is undesired based on the property of the hypothesis testing.

Future work on this diagnostics method may include more testing examples to verify the applicability and limitations of this method, development of an auto-determined regression size generator, and implementation to standard packages for its distribution. Moreover, some other potential topics could also be extended. One possible approach is the utilization of some well-developed Markov Chain Monte Carlo (MCMC) convergence diagnostics methods in order to achieve the ultimate reliability goal. Another possible research topic will be the on-the-fly monitoring scheme. Instead of determining the convergence and then assuming that all the data collected from subsequent generations are valid, an on-the-fly monitoring scheme could help to make sure this assumption is valid while collecting data. If the violation is reported by this scheme, the outcome from the simulation would be flagged as potentially non-reliable, or the start of the data accumulation would be postponed.

CHAPTER 4

REVIEW OF THE CONVERGENCE ACCELERATION METHODS

Reliable fission source distribution convergence diagnostics methods are needed not only because of the required accuracy, but also due to the limited computational capabilities, especially for large loosely-coupled problems. Convergence acceleration is another, synergistic methods to reduce the computational expense. Moreover, acceleration of the convergence transient process also assists the convergence diagnostics, because inter-generation correlation is reduced. This chapter reviews several approaches to accelerate the convergence of the fission source distribution based on different theories. Although the purpose of these methods is to accelerate the Monte Carlo simulation, some of them are a combination of the deterministic and Monte Carlo method.

4.1 Fission Matrix Method

One of the oldest attempts to accelerate the convergence of the fission source distribution is the well known fission matrix method²⁴. Technically, this method does not belong to the hybrid method category, although the method does include numerical computations, which are not treated as conventional deterministic methods, besides the Monte Carlo simulations. However, the fission matrix method is sometimes still classified as a hybrid method, because it indeed includes not only Monte Carlo simulations.

The fission matrix method requires dividing the entire simulated system into a number of small meshes or bins. The probability that one simulated particle generated in i^{th} bin will lead to one fission source for the next cycle in j^{th} bin is of interest. This probability is computed by a Monte Carlo simulation: a large number of particles will be sampled uniformly with in i^{th} bin for the simulation first; then, the number of fission

sources generated in each j^{th} bin will be recorded; eventually, the ratio of these quantities gives the probability of interest. This probability can be represented by $P_{i,j}$; as a result, if the number of bins of the system is n , all of these probabilities could yield a large n -by- n matrix, denoted as the fission matrix.

Instead of using the Monte Carlo simulation to converge the fission source distribution, this fission matrix is used for the convergence. Actually, this matrix can be viewed as a discretization of the continuous system or operator in the neutron transport equation. Therefore, the eigenvalues and eigenfunctions of this fission matrix are also eigenvalues and eigenfunctions of the nuclear system. Thus, by using the power iteration method, the fundamental eigenpair of the fission matrix can be obtained. The estimated fundamental eigenfunction of the fission matrix could approximate the fission source distribution in the original system with meshes; and the estimated fundamental eigenvalue could also provide a preliminary estimate of k_{eff} . One more point that needs to be noted is that by standard linear algebra techniques, all the other higher eigenpairs of the fission matrix can also be obtained, but these algebra techniques are not as straightforward as the power iteration method for computing the fundamental eigenpair. These eigenpairs can also be viewed as approximations of the higher eigenmodes of the nuclear system.

After the convergence of the fission matrix, a new Monte Carlo simulation with the biased fission source distribution according to the estimated fundamental eigenfunction of the fission matrix will be performed. Clearly, this Monte Carlo simulation still requires inactive generations, because the initial fission source distribution is just an approximation. However, this initial distribution is close to the converged fission source distribution; thus, the number of inactive cycles is reduced dramatically for loosely-coupled problems.

The fission matrix method takes advantage of the fast calculation of the linear algebra portion. The fast convergence of the fission matrix by the power iteration method

replaces the slow convergence of the Monte Carlo simulation. The accuracy of this approximation depends on the number of meshes. A small number of meshes results in a large difference between the estimated eigenfunction of the fission matrix and the converged fission source distribution of the nuclear system. On the other hand, a large number of meshes face the difficulty of computing many elements of a large size matrix, with sufficient statistical precision, which not only requires computational efforts, but also demands a large storage space. Despite these disadvantages, the fission matrix method is still widely-used in many Monte Carlo simulation packages as a convergence acceleration option because of its ease and convenience.

The fission matrix method serves as a simple example of combining deterministic calculations with Monte Carlo simulations in order to improve the convergence speed. Such combination methods are generally referred to as hybrid method. The deterministic calculations could employ the spherical harmonics method (known as P_N method), the discrete ordinates method (known as S_N method), or other well developed deterministic methods for approximate preliminary calculations in order to obtain an approximate fission source distribution to initialize later Monte Carlo simulations. Since the precision requirements of the preliminary calculations are not so strict, the computational cost is inexpensive in general. By using this scheme, the convergence of the fission source distribution is easier to achieve by using the Monte Carlo method for tallying purpose. Other attempts include using forward approximate deterministic method to generate importance map²⁵ to be used for later Monte Carlo method. As a result, the efficiency and reliability of the Monte Carlo simulation may be improved.

4.2 Anchoring Method

Other hybrid acceleration method, which implement the deterministic calculation into the entire Monte Carlo simulation are pursued to accelerate the convergence. The anchoring method²⁶ is one example of such hybrid methods; it contains the partial

current-based coarse mesh finite difference (p-CMFD) method²⁷ as the deterministic method. The anchoring method is based on the steady-state neutron transport equation Eq (1.4), which is rewritten here as Eq. (4.1).

$$\hat{\Omega} \cdot \bar{\nabla} \psi(\bar{r}, \hat{\Omega}, E, t) + \sigma(\bar{r}, E) \psi(\bar{r}, \hat{\Omega}, E, t) = \int_0^{+\infty} dE' \int d\Omega \left[\sigma_s(\bar{r}, E' \rightarrow E, \hat{\Omega}' \rightarrow \hat{\Omega}) + \frac{1}{k} \nu \sigma_f(\bar{r}, E' \rightarrow E, \hat{\Omega}' \rightarrow \hat{\Omega}) \right] \psi(\bar{r}, \hat{\Omega}', E', t) \quad (4.1)$$

The right hand side of Eq. (4.1) describes the source terms, consisting of the scattering source term and fission source term, for the neutron transports. The scattering source term is determined by Monte Carlo simulation, so no action is taken to change this term. However, the fission source term is decomposed into two contributions in the anchoring method, which are the Monte Carlo simulated source and deterministically calculated source.

The following Eq. (4.2) describes this decomposition as

$$\frac{1}{k} \nu \sigma_f \psi = (1 - \alpha) \frac{1}{k} \nu \sigma_f \psi + \alpha Q. \quad (4.2)$$

In the right hand side of Eq. (4.2), the first term represents the contribution from the conventional or ordinary Monte Carlo simulation, and the second term Q represents the deterministic source obtained by using the p-CMFD method. The factor α , which is referred to as anchoring factor, determines the portion of this decomposition: if $\alpha=0$, the whole fission source for the next cycle is from previous Monte Carlo simulation, so the anchoring method reduces to the normal Monte Carlo method; if $\alpha=1$, the whole fission source is from the deterministic computation, so the fission source generated by the Monte Carlo simulation is discarded. By adjusting the anchoring factor α , the deterministic source from the p-CMFD method and the Monte Carlo source together contribute to the next cycle simulation.

The deterministic source from p-CMFD method can be either fixed or updated after every several generations. Either way, the fission computed from the p-CMFD

method is an approximation of the converged fission source distribution. Therefore, by applying this approximation into the Monte Carlo simulation, number of generations required for the convergence procedure will be reduced as expected. Apparently, the accuracy of the approximated fission source from the p-CMFD method depends on the pre-specified performance of the deterministic method. Moreover, a better approximation does require more computational expense. Although the better approximation could lead to an even faster convergence rate for the anchoring method, considering the total computational expense, a good enough approximation is actually optional in terms of efficiency. This argument is reasonable, because if the p-CMFD could provide the exact converged fission source distribution, no extra generations would be required for Monte Carlo simulation.

To sum up, the anchoring method, which combines the p-CMFD deterministic method and the Monte Carlo method, is capable to accelerate the fission source convergence. The efficiency and performance of this hybrid method depends on the specifications from both the deterministic and the Monte Carlo method. In addition, the concept of the anchoring method could inspire more hybrid methods. Many other deterministic methods could also provide an approximation of the fission source distribution that could be used for Monte Carlo simulations in order to reduce the efforts for fission source convergence.

4.3 Wielandt's Method

In addition to these hybrid methods, there are also other methods based primarily on Monte Carlo simulations. Only certain modifications are required to be applied to the conventional Monte Carlo method in order to accelerate the source convergence. One well known example of such methods is the Wielandt's method²⁸. Considering the neutron transport equation, the fission source term is again divided into two separate terms as shown in Eq. (4.3)

$$\frac{1}{k} \nu \sigma_f \psi = \left(\frac{1}{k} - \frac{1}{k_w} \right) \nu \sigma_f \psi + \frac{1}{k_w} \nu \sigma_f \psi. \quad (4.3)$$

An arbitrary parameter k_w is introduced into Eq. (4.3) as a coefficient of this fission source division. Further manipulation²⁹ changes the purpose of the Monte Carlo simulations from estimating $1/k$ (k_{eff}) to estimating $1/k-1/k_w$, as the coefficient of the first term in Eq. (4.3). Since the parameter k_w is user-specified, the estimates of k is easily available afterwards.

The dominance ratio of the manipulated form, which determines the convergence rate for the power iteration method in the Monte Carlo simulation, for the Wielandt's method is changed to

$$\left| \frac{k_w - k_2}{k_w - k_1} * \frac{k_2}{k_1} \right|. \quad (4.4)$$

As long as the introduced factor k_w is smaller than one, the convergence of the fission source is accelerated. Generally, the choice of the parameter k_w requires that it is greater than both k_1 and k_2 . However, since k_1 is not known beforehand, a large enough but not too large k_w is chosen for simulations.

The implementation of the Wielandt's method in the Monte Carlo method requires modifying the source sampling and storing procedures. In the conventional Monte Carlo method, all the fission source positions will be recorded in the fission bank in order to serve as source points for the next generation. After this procedure, the current generation is officially finished; and the next generation will start over with only the fission bank. For the Wielandt's method, this procedure is slightly changed by computing two expected numbers of fission source points: one is the expected number of fission source points stored in the fission bank; the other is the expected number of fission source points simulated in the current generation. New histories, which are generated according to the second expected number, will be simulated as parts of the current

generation. This procedure continues until the number of reproduction in one generation reaches certain limit.

Therefore, the traveling path from one initial source position is longer in one generation of the Wielandt's method than that in one generation of a conventional Monte Carlo simulation. Thus, the Wielandt's method could reduce the number of cycles required for the fission source distribution to convergence. However, the total computational expense of the Wielandt's method is almost the same as (in some cases, may be larger than) the computational expense in a conventional Monte Carlo simulation. Despite this disadvantage, the Wielandt's method is still useful for convergence diagnostics because of the more information contained in one simulation generation. In addition, the auto-correlation effect between consecutive generations is also reduced in the Wielandt's method because of the less connection between the fission sources.

4.4 Smoothed Residual Acceleration Method

Another acceleration method inspired by the linear extrapolation method, is called the smoothed residual acceleration (SRA) method introduced in Ref. 30 and 31. This method aims to accelerate the convergence based on the trend of the mesh-wise source distributions. By recalling Eq. (1.7), the estimate of the fundamental eigenfunction can be expressed as Eq. (4.5) after n iterations

$$\hat{\psi}_1 = \frac{1}{k_1^n} A^n \psi = \sum_{i=1}^{\infty} \left(\frac{k_i}{k_1} \right)^n a_i \psi_i, \quad (4.5)$$

where the coefficients a_i are defined as in Eq. (1.6) for the well-behaved function Ψ . An iterative expression of Eq. (4.5) is

$$\hat{\psi}_1^{m+1} = \frac{1}{k_1} A \hat{\psi}_1^m, \quad (4.6)$$

where m denotes the generation index. Therefore, the extrapolation expression of Eq. (4.6) is

$$\hat{\psi}_1^{m+1} = \frac{1}{k_1} A \hat{\psi}_1^m + \alpha \left(\frac{1}{k_1} A \hat{\psi}_1^m - \hat{\psi}_1^m \right) \quad (4.7)$$

with a certain value for the extrapolation coefficient α . As a result, a similar estimate as in Eq. (4.5) is

$$\hat{\psi}_1^{m+1} = \sum_{i=1}^{\infty} \left((1 + \alpha) \frac{k_i}{k_1} - \alpha \right)^n a_i \psi_i. \quad (4.8)$$

As long as the extrapolation coefficient satisfies

$$\max \left(\left| (1 + \alpha) \frac{k_i}{k_1} - \alpha \right| \right) < \left| \frac{k_2}{k_1} \right|, \quad (4.9)$$

the SRA method accelerates the convergence.

The implementation of the SRA method in the Monte Carlo simulation employs the mesh estimates of the fission source density. According to the extrapolation theory, the weights of the fission sources will be adjusted to satisfy the density trend within the certain mesh. New sources are re-sampled evenly in each mesh according to the weights adjustments. This procedure forces the source distribution to follow the previous changing direction. In other words, if the mesh-wise fission source density is increasing in the last two generations, the new fission sources will carry more weights in order to follow the increasing trend. As a result, this process leads the source distribution to the convergence faster than the conventional Monte Carlo simulations.

A constant or decreasing extrapolation coefficient α is used in the acceleration process, but eventually, the SRA technique should be turned off in order to prevent further pollution of the source distribution by extrapolation after convergence. However, when to turn off the SRA method depends on the reasonable convergence diagnostics method. The SRA acceleration method has been only recently proposed, so more testing and validations are necessary for the method to be widely accepted.

CHAPTER 5

THE MODIFIED POWER ITERATION ACCELERATION METHOD

In addition to the acceleration methods discussed in **Chapter 4**, a recently-developed modified power iteration method could also accelerate the convergence by using mainly the Monte Carlo method.

5.1 Review of the Modified Power Iteration Method

The modified power iteration method^{5, 32} is based on the ordinary power iteration method. However, unlike Eq. (1.6), the decomposition of a well-behaved function Ψ is given as

$$\Psi = \sum_{i=1}^{\infty} (a_i + b_i x) \psi_i. \quad (5.1)$$

Two sets of decomposition coefficients, a_i and b_i , are used in Eq. (5.1). In addition, a new unknown parameter x is introduced in the equation in order to balance the estimates. Applying the matrix or operator A to function Ψ as in the ordinary power iteration method will provide again the estimates of the eigenfunctions and eigenvalues. After convergence, only the two lowest eigenfunction components remain

$$\lim_{n \rightarrow \infty} \frac{1}{k_1^n} A^n \Psi = \lim_{n \rightarrow \infty} \frac{1}{k_1^n} \left((a_1 + b_1 x) k_1^n \psi_1 + (a_2 + b_2 x) k_2^n \psi_2 \right). \quad (5.2)$$

In this case, the estimate of eigenvalues is

$$\lim_{n \rightarrow \infty} \frac{A^n \Psi}{A^{n-1} \Psi} = \lim_{n \rightarrow \infty} \frac{(a_1 + b_1 x) k_1^n \psi_1 + (a_2 + b_2 x) k_2^n \psi_2}{(a_1 + b_1 x) k_1^{n-1} \psi_1 + (a_2 + b_2 x) k_2^{n-1} \psi_2}. \quad (5.3)$$

In this equation, different choices of the unknown parameter x would lead the estimate to a different eigenmode. For example, if x is determined to be $-b_1/a_1$, the fundamental eigenfunction components in Eq. (5.2) and Eq. (5.3) will be eliminated, so the estimate of the eigenfunction Eq. (5.2) will be the second eigenfunction, and the estimate of the

eigenvalue Eq.(5.3) will be k_2 . Likewise, if x is chosen to be $-b_2/a_2$, the estimates of the eigenfunction and eigenvalue will be the fundamental eigenmode.

The remaining question is how to choose x in order to be either $-b_1/a_1$ or $-b_2/a_2$. This task can be fulfilled by two separate estimates of the eigenvalue in two different regions, which are neither necessarily mutually exclusive nor necessarily covering the full space. Thus, by setting the two estimates equal, a quadratic equation of unknown x is obtained. One root of the equation is close to $-b_1/a_1$ as an estimate and the other root is close to $-b_2/a_2$ as an estimate. Hence, the fundamental eigenmode and the second eigenmode can be estimated simultaneously by applying these roots. Moreover, this procedure of the power iteration has the potential to increase the convergence rate to the fundamental mode, in terms of the dominance ratio, from k_2/k_1 to k_3/k_1 ³³ as a significant achievement.

5.2 Derivations of the Convergence and Convergence Rate⁵

Section 5.1 only gives the theory, procedures, and conclusions of the modified power iteration method. This section will provide more detailed demonstration and derivation of this scheme.

Based on Eq. (5.1), the following change of variables is used:

$$y = a_2 + b_2x, \quad (5.4)$$

$$\alpha_i = a_i - \frac{a_2}{b_2} * b_i, \quad (5.5)$$

$$\text{and } \beta_i = \frac{b_i}{b_2}. \quad (5.6)$$

A new unknown parameter y replaces the position of x in previous expression; and two sets of new coefficients α_i and β_i take places of the old coefficients a_i and b_i . As a result, the decomposition expression in Eq. (5.1) will change to

$$\psi = \sum_{i=1}^{\infty} (\alpha_i + y^* \beta_i) \psi_i = (\alpha_1 + y^* \beta_1) \psi_1 + y^* \psi_2 + \sum_{i=3}^{\infty} (\alpha_i + y^* \beta_i) \psi_i . \quad (5.7)$$

This new expression simplifies the coefficients of the second component due to the fact that $\alpha_2=0$ and $\beta_2=1$.

In order to estimate the eigenvalues, integrals or estimates are necessary. The integral of one eigenfunction ψ_j in region R_i is defined as N_{ij} , as given in Eq. (5.8).

$$\int_{R_i} \psi_j = N_{ij} \quad (5.8)$$

In the two pre-specified not exclusive regions R_1 and R_2 , the integrals of the initial well-behaved function ψ are

$$V_1 = \int_{R_1} \psi = \sum_{i=1}^{\infty} (\alpha_i + y^* \beta_i) N_{1j} \quad (5.9)$$

$$V_2 = \int_{R_2} \psi = \sum_{i=1}^{\infty} (\alpha_i + y^* \beta_i) N_{2j} . \quad (5.10)$$

Thus, the estimates of the eigenvalues in the two regions will be

$$k_{R_1} = \frac{\sum_{i=1}^{\infty} (\alpha_i + y^* \beta_i) N_{1i} * k_i}{\sum_{i=1}^{\infty} (\alpha_i + y^* \beta_i) N_{1i}} \quad (5.11)$$

$$k_{R_2} = \frac{\sum_{i=1}^{\infty} (\alpha_i + y^* \beta_i) N_{2i} * k_i}{\sum_{i=1}^{\infty} (\alpha_i + y^* \beta_i) N_{2i}} . \quad (5.12)$$

After convergence, these two estimates should be the same. Thus, by setting Eq. (5.11) and (5.12) to be equal, the solution of the quadratic equation about unknown parameter y will lead the estimates to convergence. Clearly, this quadratic equation includes coefficients with infinite summation, which cannot be solved in general. However, reconsidering the iterative procedure reveals that after several iterations, one root of y will approach to zero, which leads all the high order harmonics to disappear.

As a result, only the first two eigenmode components remain in the following approximation of the quadratic equation after sufficient number of iterations. The coefficient of the y^0 term turns to

$$\left(\sum_{i=1}^{\infty} \alpha_i N_{1i} k_i \right) * \left(\sum_{j=1}^{\infty} \alpha_j N_{2j} \right) - \left(\sum_{i=1}^{\infty} \alpha_i N_{2i} k_i \right) * \left(\sum_{j=1}^{\infty} \alpha_j N_{1j} \right) = \sum_{i=1}^{\infty} \sum_{j=1}^{\infty} \alpha_i \alpha_j N_{1i} N_{2j} (k_i - k_j). \quad (5.13)$$

Likewise, the coefficient for the y^1 term turns to

$$\sum_{i=1}^{\infty} \sum_{j=1}^{\infty} \alpha_i \beta_j (k_i - k_j) (N_{1i} N_{2j} - N_{1j} N_{2i}). \quad (5.14)$$

Another alternative expression for Eq. (5.14) is

$$\sum_{i=1}^{\infty} \sum_{j=1}^{\infty} k_i (\alpha_i \beta_j + \alpha_j \beta_i) (N_{1i} N_{2j} - N_{1j} N_{2i}). \quad (5.15)$$

Since the root close to zero is of interest here, the y^2 term is neglected, because it is small compared with other terms. Thus, the estimate of this root will be

$$\begin{aligned} r &= - \frac{y^0 \text{ term coefficient}}{y^1 \text{ term coefficient}} \\ &= - \frac{\sum_{i=1}^{\infty} \sum_{j=1}^{\infty} \alpha_i \alpha_j N_{1i} N_{2j} (k_i - k_j)}{\sum_{i=1}^{\infty} \sum_{j=1}^{\infty} k_i (\alpha_i \beta_j + \alpha_j \beta_i) (N_{1i} N_{2j} - N_{1j} N_{2i})}. \end{aligned} \quad (5.16)$$

Certain restrictions still apply to this estimate for further simplification:

When $i=j$, then $N_{1i} N_{2j} = N_{1j} N_{2i}$; $\alpha_2 = 0$ and $\beta_2 = 1$ hold all the time. As a result, the dominant portion of the numerator are the terms corresponding to $i=1, j=3$ and $i=3, j=1$ cases

$$\begin{aligned} &\alpha_1 \alpha_3 N_{11} N_{23} (k_1 - k_3) + \alpha_3 \alpha_1 N_{13} N_{21} (k_3 - k_1) \\ &= \alpha_1 \alpha_3 (N_{11} N_{23} - N_{13} N_{21}) (k_1 - k_3). \end{aligned} \quad (5.17)$$

Likewise, the dominant portion of the denominator are the terms corresponding to $i=1, j=2$ and $i=2, j=1$ cases

$$k_1 (\alpha_1 \beta_2) (N_{11} N_{22} - N_{12} N_{21}) + k_2 (\alpha_1 \beta_2) (N_{12} N_{21} - N_{11} N_{22})$$

$$= \alpha_1 \beta_2 (k_1 - k_2) (N_{11} N_{22} - N_{12} N_{21}). \quad (5.18)$$

With these approximations, Eq. (5.16) turns to be

$$r \approx -\frac{\alpha_1 \alpha_3 (N_{11} N_{23} - N_{13} N_{21}) (k_1 - k_3)}{\alpha_1 \beta_2 (k_1 - k_2) (N_{11} N_{22} - N_{12} N_{21})} = -\frac{\alpha_3 (k_1 - k_3) (N_{11} N_{23} - N_{13} N_{21})}{\beta_2 (k_1 - k_2) (N_{11} N_{22} - N_{12} N_{21})}. \quad (5.19)$$

Going back to the Eq. (5.1), after one iteration, the well-behaved function for the next iteration changes to be

$$\frac{A\psi}{k_1} = \sum_{i=1}^{\infty} (a_i + x * b_i) \frac{k_i}{k_1} \psi_i. \quad (5.20)$$

Thus, the coefficients are updated by

$$\alpha_i \rightarrow \frac{k_i}{k_1} \alpha_i \text{ and } \beta_i \rightarrow \frac{k_i}{k_2} \beta_i. \quad (5.21)$$

The new estimated root by Eq. (5.16) changes to be

$$r \rightarrow -\frac{\sum_{i=1}^{\infty} \sum_{j=1}^{\infty} \frac{k_i}{k_1} \alpha_i \frac{k_j}{k_1} \alpha_j N_{1i} N_{2j} (k_i - k_j)}{\sum_{i=1}^{\infty} \sum_{j=1}^{\infty} k_i \left(\frac{k_i}{k_1} \alpha_i \frac{k_j}{k_2} \beta_j + \frac{k_j}{k_1} \alpha_j \frac{k_i}{k_2} \beta_i \right) (N_{1i} N_{2j} - N_{1j} N_{2i})}. \quad (5.22)$$

According to the same restrictions, the dominant remaining of the numerator are $i=1, j=3$ and $i=3, j=1$ cases

$$\begin{aligned} & \frac{k_1}{k_1} \alpha_1 \frac{k_3}{k_1} \alpha_3 N_{11} N_{23} (k_1 - k_3) + \frac{k_3}{k_1} \alpha_3 \frac{k_1}{k_1} \alpha_1 N_{13} N_{21} (k_3 - k_1) \\ &= (k_1 - k_3) \alpha_1 \alpha_3 \frac{k_3}{k_1} (N_{11} N_{23} - N_{13} N_{21}). \end{aligned} \quad (5.23)$$

Similarly, the denominator has its dominant parts with $i=1, j=2$ and $i=2, j=1$ cases

$$\begin{aligned} & k_1 \left(\frac{k_1}{k_1} \alpha_1 \frac{k_2}{k_2} \beta_2 \right) (N_{11} N_{22} - N_{12} N_{21}) + k_2 \left(\frac{k_1}{k_1} \alpha_1 \frac{k_2}{k_2} \beta_2 \right) (N_{12} N_{21} - N_{11} N_{22}) \\ &= \alpha_1 \beta_2 (k_1 (N_{11} N_{22} - N_{12} N_{21}) + k_2 (N_{12} N_{21} - N_{11} N_{22})) \\ &= \alpha_1 \beta_2 (k_1 - k_2) (N_{11} N_{22} - N_{12} N_{21}). \end{aligned} \quad (5.24)$$

If taking Eq. (5.19) as the “old” root, the updated “new” root by plugging in Eq. (5.23) and (5.24) will be

$$\begin{aligned}
 r_{new} &\approx -\frac{(k_1 - k_3)\alpha_1\alpha_3\frac{k_3}{k_1}(N_{11}N_{23} - N_{13}N_{21})}{\alpha_1\beta_2(k_1 - k_2)(N_{11}N_{22} - N_{12}N_{21})} \\
 &= -\frac{\frac{k_3}{k_1}\alpha_3(k_1 - k_3)(N_{11}N_{23} - N_{13}N_{21})}{\beta_2(k_1 - k_2)(N_{11}N_{22} - N_{12}N_{21})}. \tag{5.25}
 \end{aligned}$$

Clearly, the comparison between Eq. (5.19) and (5.25) indicates that the convergence rate of the desired root of y , which leads the eigenvalue estimate to k_{eff} , to approach to zero is k_3/k_1 .

With this result, the estimate of the fundamental eigenfunction is

$$\frac{A^n \psi}{k_1^n} = \sum_{i=1}^{\infty} \left(\frac{k_i}{k_1}\right)^n \alpha_i \psi_i + \sum_{i=1}^{\infty} \left(\frac{k_i}{k_2}\right)^n y^* \beta_i \psi_i. \tag{5.26}$$

The only desired remaining component in this estimate is the fundamental component, so all the other high eigenmodes are undesired error. One dominant undesired component is the second eigenmode component with coefficient

$$\left(\frac{k_2}{k_1}\right)^n \alpha_2 + \left(\frac{k_2}{k_2}\right)^n y^* \beta_2. \tag{5.27}$$

However, by taking the conditions about the coefficients as $\alpha_2=0$ and $\beta_2=1$, Eq. (5.27) decays to zero with the same convergence rate as the root of y converges to zero, which is k_3/k_1 . The other dominant undesired components is the third eigenmode component with coefficient

$$\left(\frac{k_3}{k_1}\right)^n \alpha_3 + \left(\frac{k_3}{k_2}\right)^n y^* \beta_3. \tag{5.28}$$

The convergence rate for the second term in Eq. (5.28) is smaller than that for the first term. Therefore, the component for this coefficient to converge to zero is also k_3/k_1 .

Similarly, all the high eigenmode components have coefficients converging to zero even faster. Overall, the convergence rate for the undesired components in Eq. (5.26) is k_3/k_1 as claimed in Section 5.1.

A similar approach could also be applied to the estimate of the second eigenmode, the convergence rate of which will be k_3/k_2 . However, due to the repetition of the derivation, it is not included here.

5.3 Matrix Example and Collapse

As the first example to illustrate the capability of the modified power iteration method, the same matrix example as in Ref. 34 is used again in this section. The matrix A used here is given as

$$A = \begin{pmatrix} -1.1500 & -0.6250 & -3.0250 & -1.9500 \\ 0.5167 & 1.3750 & 0.6417 & 0.7167 \\ 2.6833 & -0.8750 & 4.0583 & -0.1167 \\ -0.9833 & 2.1250 & 0.3917 & 4.2167 \end{pmatrix}.$$

As a reference, the eigenvalues of the matrix A are 4, 3, 1, and 0.5. Two arbitrary initial vectors $\mathbf{a}=(1 \ 1 \ 1 \ 1)$ and $\mathbf{b}=(1 \ 0 \ 1 \ 1)$ before renormalization are used for the modified power iteration scheme, and the unknown parameter x is assigned in front of \mathbf{b} . The first component of each vector is taken as the first group and the last three components of the vector are taken as the second group. These two groups correspond to the integral regions R_1 and R_2 in **Section 5.2** in order to estimate the eigenvalues. Under this scheme, 100 iterations are used for the convergence of the estimates of the eigenvalues.

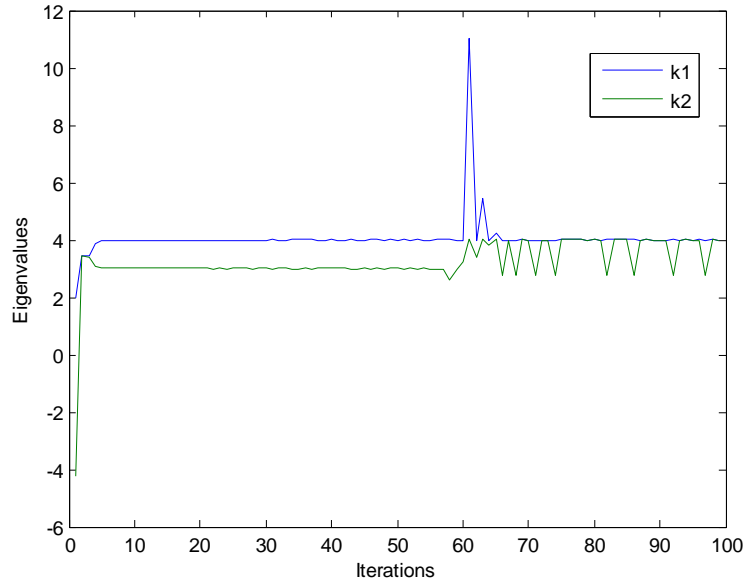


Figure 5.1. Eigenvalue estimates for the matrix problem using the modified power iteration method (Ref. 34)

Figure 5.1 shows the estimated k_1 and k_2 after each iteration for this computation. After the initial transient stage, the two estimates converge to k_1 and k_2 respectively for ~ 50 iterations. However, after ~ 55 iterations, the estimates behave abnormally with oscillations. This behavior, which is referred to as collapse of the modified power iteration method, is due to the fact that both \mathbf{a} and \mathbf{b} converge to the fundamental eigenfunction; after sufficient iterations, the difference between \mathbf{a} and \mathbf{b} is smaller than the numerical accuracy of the computational platform. Therefore, the estimates after the collapse are meaningless.

The collapse of the scheme may not be a big issue for a deterministic method, such as in this matrix example, because in general, deterministic method has a stopping criterion for the computation. Before the collapse of the scheme, the computation has typically converged; in other words, the computational error has met the stopping criterion. Therefore, accurate results for the deterministic calculation may be obtained. However, this is not the case for the Monte Carlo method because of the uncertain

property associated with the method. In order to reduce the uncertainty, Monte Carlo simulations require sufficient number of iterations. In this case, the collapse of the scheme will prevent obtaining an accurate solution. Thus, certain refinements are necessary in order to apply the method to Monte Carlo simulations successfully.

5.4 Refinements to Avoid the Collapse

In Ref. 33, two refinements were proposed in order to avoid the collapse.

The First Refinement

In the original scheme, the two initial vectors \mathbf{a} and \mathbf{b} will be changed to $A*\mathbf{a}$ and $A*\mathbf{b}$ after one iteration. Then, $A*\mathbf{a}$ and $A*\mathbf{b}$ are treated as \mathbf{a} and \mathbf{b} for the next iteration. The two roots of the unknown parameter x are denoted as x_1 and x_2 ; as a result, $\mathbf{a}+x_1*\mathbf{b}$ estimates the fundamental eigenfunction Ψ_1 , and $\mathbf{a}+x_1*\mathbf{b}$ estimates the fundamental eigenfunction Ψ_2 . The first refinement keeps $A*\mathbf{b}$ the same for the next iteration but takes $A*\mathbf{a}+x_2*A*\mathbf{b}$ to be the other vector for the next iteration. This refinement prevents vectors \mathbf{a} and \mathbf{b} from merging together to the fundamental eigenfunction after several iterations, which would cause the failure of the scheme with the finite computational accuracy. The parameter x_2 could also serve as a convergence criterion, because the vector \mathbf{a} is converging to the second eigenfunction, and consequently x_2 is converging to zero.

Figure 5.1 shows another computational example of the matrix problem with different initial vectors $\mathbf{a}=(1\ 1\ 0\ 0)$ and $\mathbf{b}=(0\ 0\ 1\ 1)$ under the first refinement for 100 iterations. After the transient stage, the two estimates converge to the first two eigenvalues, respectively.

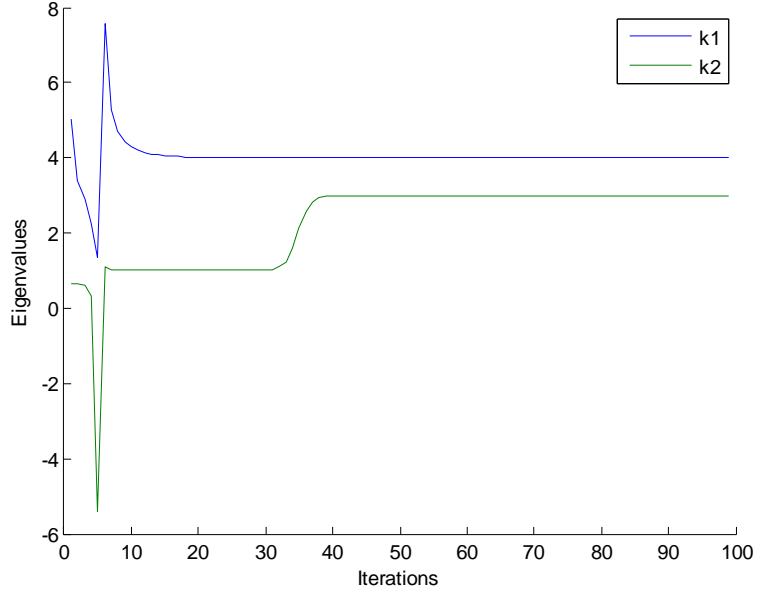


Figure 5.2. Eigenvalue estimates for the matrix problem using the first refinement from of the modified power iteration method (Ref. 34)

Following the derivations in **Section 5.2**, the updated coefficients after one iteration are

$$a_i \rightarrow \frac{k_i}{k_1} a_i + R \frac{k_i}{k_1} b_i \text{ and } b_i \rightarrow \frac{k_i}{k_1} b_i. \quad (5.29)$$

In Eq. (5.29), the notation R represents the root of the equation x , which comes from the root r about changed unknown parameter y . Similar to Eq. (5.21), the updated new set of coefficients is

$$\begin{aligned} \alpha_i &\rightarrow \frac{k_i}{k_1} a_i + R \frac{k_i}{k_1} b_i - \frac{\frac{k_2}{k_1} a_2 + R \frac{k_2}{k_1} b_2}{\frac{k_2}{k_1} b_2} \times \frac{k_i}{k_1} b_i \\ &= \frac{k_i}{k_1} a_i + R \frac{k_i}{k_1} b_i - \frac{a_2 + R b_2}{b_2} \frac{k_i}{k_1} b_i = \frac{k_i}{k_1} \alpha_i, \end{aligned} \quad (5.30)$$

and

$$\beta_i \rightarrow \frac{\frac{k_i}{k_1} b_i}{\frac{k_2}{k_1} b_2} = \frac{k_i}{k_2} \beta_i. \quad (5.31)$$

Comparing Eq. (5.30) and (5.31) with Eq. (5.21) reveals that the expressions of these coefficients are identical. Thus, the estimated root of y , which is noted as r , converges with the same rate, k_3/k_1 , to zero. The convergence rate of the estimate of the eigenfunction is based on the definition of R as

$$R = \frac{r - a_2}{b_2}. \quad (5.32)$$

Under this relation, the estimate of the eigenfunction is

$$\psi_{new} = \sum_{i=1}^{\infty} (a_i + R b_i + x^* b_i) \frac{k_i}{k_1} \psi_i = \sum_{i=1}^{\infty} \frac{k_i}{k_1} \alpha_i \psi_i + \sum_{i=1}^{\infty} y^* \frac{k_i}{k_2} \beta_i \psi_i. \quad (5.33)$$

This expression is actually the same as the estimate in Eq. (5.26). Therefore, the convergence rate of the estimate of the fundamental eigenfunction is still k_3/k_1 for the first refinement.

The Second Refinement

The second refinement is based on the first refinement. In addition to the replacement of $A^* \mathbf{a}$ by $A^* \mathbf{a} + x_2^* A^* \mathbf{b}$, the second refinement also replace $A^* \mathbf{b}$ by $A^* \mathbf{a} + x_1^* A^* \mathbf{b}$, in which x_1 is the other root of the unknown x that leads the eigenfunction estimate to the fundamental one. The derivation of the second refinement is even more complex than that for the original scheme and the first refinement. Therefore, this section will not include the detailed derivation. Even though, the convergence rate under the second refinement does not change, so this refinement could achieve the fast convergence without the collapse described in previous section.

Unfortunately, this refinement contains a drawback for numerical implementations. As the iterations proceed, vector \mathbf{b} converges to Ψ_1 and vector \mathbf{a}

converges to Ψ_2 , which results in the parameter x_j in A^*a+x_j*A*b converging to infinity and eventually out of the computational range. This drawback was not crucial for deterministic applications, because the estimated results should have reached the stopping criterion before this happens. However, when using this refinement for Monte Carlo simulations, one has to be aware of this drawback when increasing the number of iterations to improve the confidence interval. However, because of the statistical uncertainty, the root x_j in Monte Carlo simulation cannot reach infinity. Instead, it jumps from one very large number to another. The impact of this effect to the Monte Carlo simulation is not quite clear; for now, it seems that one could take this effect as acceptable.

5.5 Net-Weight Calculation Schemes

One issue that arises in the iterative procedure with the refinements is that it requires basic numerical computation of summation and deduction. This may not be significant for the matrix problem, for example if A^*a+x_j*A*b is desired, because the computation is explicit with the known matrix, vectors, and value of x_j . However, this issue is difficult to resolve for Monte Carlo simulations, because the simulation can be viewed as a continuous procedure, and explicit quantities are not available for computations. For instance, in one simple simulation, the refinements will introduce “negative” histories or particles that travel within the system. Thus, the contribution of this “negative” particle to normal “positive” regions can needs somehow to be determined. Therefore, schemes that allows to compute the net effects from both “positive” regular particles and imagined “negative” particles are necessary. The calculation of the net-weight distribution is referred to as “weight cancellation” in previous literatures. However, it seems that using the term “net-weight” calculation is more appropriate since the purpose is not to obtain a result close to zero, which is the general meaning of cancellation. Therefore, “cancellation” is only used in the following

discussion for consistency to name the methods described in the references as weight cancellation methods. These schemes could either be mesh-wise or point-wise depending on the design of the simulation.

Point Detector Cancellation Scheme

In Ref. 35, a net weight calculation scheme similar to the point detector concept was proposed. Considering one single Monte Carlo simulation with N particles per generation, each particle possesses two weights, positive and negative, representing the two sets of different weights or flux distributions. Before starting the new simulation generation, N new points, which are treated as point detectors, are sampled randomly over the entire system. Thus, along with the simulation, each point detector records two net contributions from all the simulated particles with different sets of weights. After finishing the simulation, these point detectors will serve as fission sources for the next generation with renormalized weights accordingly. Since the positions of the point detectors are randomly determined, and they record all the contributions, this scheme computes the net-weight from positive and negative contributions exactly. However, the computational effort for point detectors is very high compared to other types of tallies. By using this scheme, N point detectors exist in the system within only one generation. Thus, the total computational expense is costly despite the accuracy of this net-weight calculation scheme.

Mesh-wise Cancellation Scheme

Another set of net-weight calculation schemes is based on the mesh-wise tally proposed in Ref. 36 and 32. Basically, two sets of mesh-wise tallies, which are either flux tallies or fission density tallies, record the contributions for the two sets of weights carried by the simulated “positive” and “negative” particles. After each simulation generation, the two sets of mesh-wise tallies are used to represent the net weight or flux

distribution. Moreover, these two sets of mesh-wise tallies can be easily applied to summation and deduction. Therefore, the new fission sources for the next generation will carry the appropriate weights according to the mesh-wise weight distribution. In Ref. 36, the new fission sources are re-sampled evenly within the mesh with different weights. In Ref. 32, the fission sources are determined by the previous simulations. Only the weights are changed according to the mesh-wise tallies. This scheme is relatively easy to implement and the computational requirement is not too high. However, the accuracy of the mesh-wise tallies depends on the number of meshes or the size of meshes. For a fine mesh structure, this net-weight calculation is a good enough approximation, but it is computational intensive. For a coarse mesh structure, computational effort is reduced, but so is the accuracy. Thus, an optimal choice of the size of meshes is necessary to balance efficiency and accuracy.

Exact Regional Weight Cancellation Scheme

Recently, Booth and Gubernatis³⁷ proposed a new exact regional weight cancellation technique. Basically, the method combines the mesh-wise weight tally and point sources together to represent the weight or flux distribution. Essentially, one fission source generated after simulation can be treated as from either a flat fission density in the mesh or a changing fission density that represents the actual fission density. Therefore, with certain probability, the fission source will be preserved or deleted. If the fission source is deleted, it is treated as generated from the flat fission density. Thus, in order to maintain the entire weight contribution, the mesh-wise tally will record the contribution of this fission source. Together, the sets of fission sources and mesh-wise weights are used for the required computations.

According to the reference, this net-weight calculation scheme maintains all the information of the fission source distribution, so it is an exact scheme. In addition, the

required mesh structure is coarse, so no large storage is necessary for scheme. However, since this method has been proposed only recently, it has not been evaluated in this work.

5.6 One-dimensional Two-group Monte Carlo Simulation Examples

In order to validate the modified power iteration method, two one-dimensional examples³⁸ are used in this section. The examples are using two energy groups, which has not been tested before, to verify the applicability of the method for multi-group energy structure. Indeed, the concept of fundamental eigenfunction cannot be represented by any single group-wise flux distribution alone. Instead, the fission source distribution, which in simulations is treated as energy-independent once it is generated, is used to represent the eigenfunction. The mesh-wise net-weight calculation method is used in these examples with re-sampling sources in each mesh. The tally used is not a cell flux; instead, in order to contain all the energy-independent fissions, the fission density with collision estimator

$$\text{Fission Density} = \frac{1}{V * N} * \sum_i \sum_g \frac{w_i * \nu_g * \Sigma_{f,g}}{\Sigma_t} \quad (5.33)$$

serves as the mesh-wise tally. In Eq. (5.33), V is the mesh volume; N is the total number of particles per generation; i represents collisions taking place in the specific mesh; w_i is the weight of a particle colliding; g represents the energy group the collision happens in; and $\nu \Sigma_t$ is the average number of fission neutrons per fission times the total cross section for each collision.

Single Region Example

The first example is a one-dimensional two-group nuclear system with only one type of fission material. **Table 5.1** lists all the postulated information about this fission material. The system extends from -4.5cm to 4.5cm with vacuum boundary conditions on both ends. Two sub-regions, the left one (-4.5cm to 0cm) and the right one (0cm to 4.5cm), are used to estimate the eigenvalues separately in order to obtain the quadratic

equation. Evenly distributed one hundred meshes are used for the flux estimate and mesh-wise net-weight calculation.

Table 5.1 Fissionable material information for one region example used for the modified power iteration method (Ref. 38) (cross-section in cm^{-1})

Group 1						
Σ_{t1}	Σ_{c1}	Σ_{f1}	ν_1	Σ_{1-1}	Σ_{1-2}	χ_1
1.0	0.05	0.05	3.0	0.1	0.8	1.0
Group 2						
Σ_{t2}	Σ_{c2}	Σ_{f2}	ν_2	Σ_{2-1}	Σ_{2-2}	χ_2
1.0	0.2	0.1	3.0	0.0	0.7	0.0

The simulation with the modified power iteration method employs 10,000 particles per generation for 50 inactive generations and 100 active generations. For comparison, MCNP5 is used to obtain reference k_{eff} , with 50,000 particles per generation for 1,000 active generations after the convergence of the fission source distribution.

Table 5.2 summaries the k_{eff} estimates from both methods. The results are consistent, which indicates the validity of the modified power iteration method.

Table 5.2. Comparison of k_{eff} for one region example using the modified power iteration method (Ref. 38)

MCNP5	Modified method	Difference
0.94386 ± 0.00008	0.94401 ± 0.00019	0.7σ

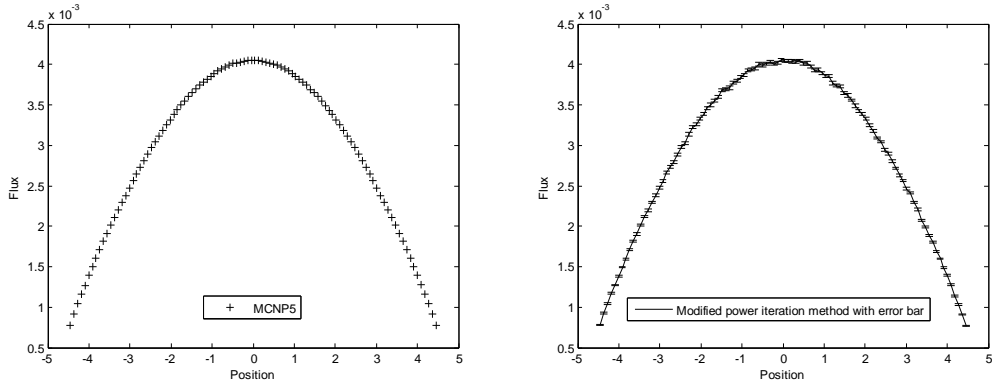
In addition to the estimates of the fundamental eigenvalue, the second eigenvalue is also obtained from the computation. The fission matrix method, which is also using

100 meshes, is used to obtain the reference result for comparison. Based on the previous discussion, this reference result is just an approximation, but still, it could indicate the applicability of the modified power iteration method for computing the second eigenvalue. **Table 5.3** summarizes the comparison of k_2 , the results in which again agree with each other.

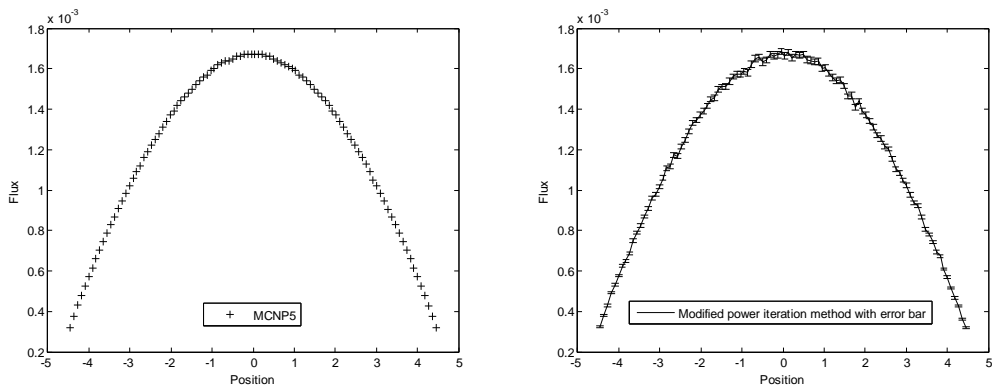
Table 5.3. Comparison of k_2 for one region example using the modified power iteration method (Ref. 38)

Reference	Modified method	Difference
0.71894	0.71907 ± 0.00040	$<0.3\sigma$

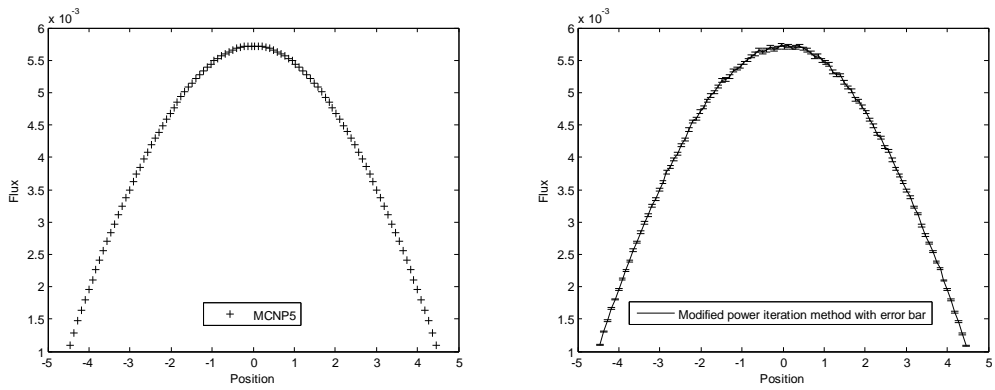
Besides the comparisons of estimates of eigenvalues, the estimates of the fundamental and second eigenfunctions are also consistent with the reference. **Figure 5.3** shows the comparisons of the estimates of the total flux and group-wise fluxes from the modified power iteration method and MCNP5. By visual inspection, the curves seem consistent with each other. In order to quantify the consistency, **Table 5.4** lists the fractions of meshes that have the relative distance within 1σ , 2σ , and 3σ combined standard deviations. Clearly, this distribution agrees well with a standard normal distribution, which again indicates the correctness of the method and the accuracy of the flux estimates.



(a) Comparison of thermal fluxes



(b) Comparison of fast fluxes



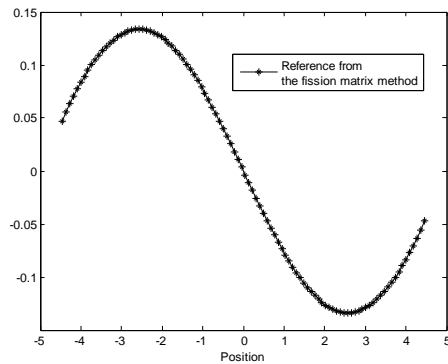
(c) Comparison of total fluxes

Figure 5.3. Comparisons of reference fluxes and computed fluxes for the fundamental eigenmode for one region example using the modified power iteration method (Ref. 38)

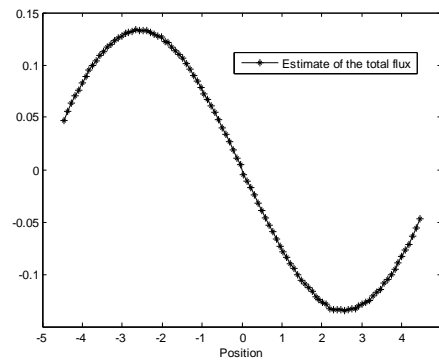
Table 5.4. Fractions of relative distances in combined standard deviations for one region example (in %) using the modified power iteration method (Ref. 38)

	Fast flux	Thermal flux	Total flux
Within 1σ	67	72	67
Within 2σ	92	95	93
Within 3σ	99	100	100

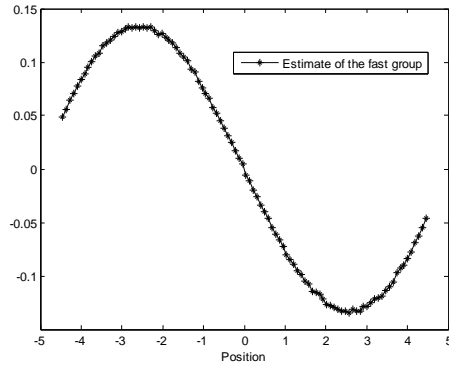
In addition to the estimate of the fundamental flux distribution, the estimated second eigenfunction is also available. **Figure 5.4** shows the estimated total flux and group-wise fluxes with a reference result from the fission matrix method. This reference is only for total flux, because the computation is based on all the simulated particles. Also, the magnitudes in **Figure 5.4** have been renormalized according to the sum of squares of mesh-wise tallies (L_2 norm). Therefore, only the shapes of these estimates are of interest. Again, good agreement may be obtained.



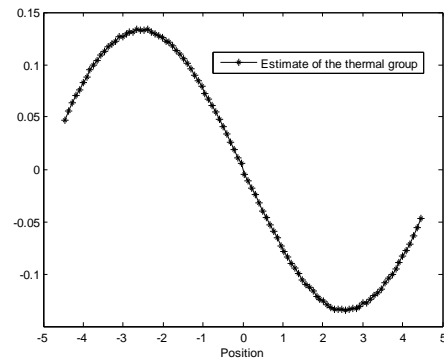
(a) Reference



(b) Estimate of the total flux



(c) Estimate of the fast group



(d) Estimate of the thermal group

Figure 5.4. Comparisons of reference fluxes and computed fluxes for the second eigenmode for one region example using the modified power iteration method (Ref. 38)

Multiple Regions Example

The next example is still one-dimensional, but includes multiple regions with different materials. The system again extends from -4.5cm to $+4.5\text{cm}$ with three regions and vacuum boundary conditions: one fissionable region in the middle (-3.0cm to $+3.0\text{cm}$) and two non-fissionable regions left and right (-4.5cm to -3.0cm and $+3.0\text{cm}$ to $+4.5\text{cm}$). The structure of this example is shown in **Figure 5.5**. The fissionable material used is the same as in the previous example, with all information listed in **Table 5.1**. In addition, **Table 5.5** shows the required information for the non-fissionable material. This example is trying to mimic the situation for a multiplying system with a reflector outside, although the specified cross-sections are not quite realistic.



Figure 5.5. Geometry structure of multiple regions example used for the modified power iteration method (Ref. 38)

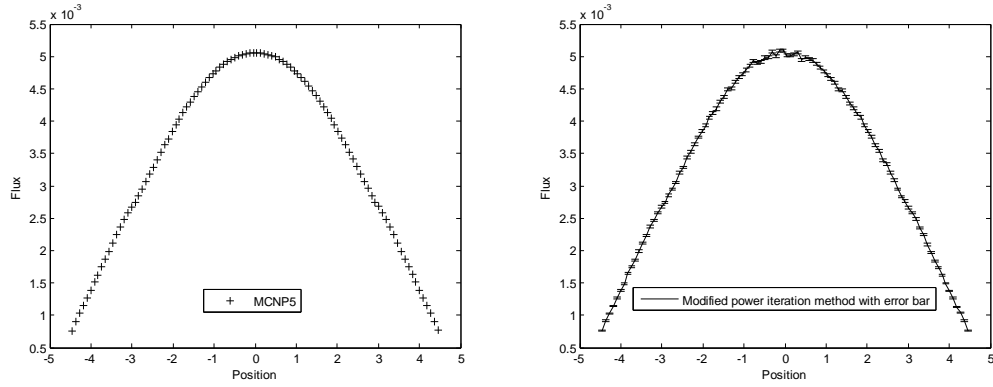
Table 5.5 Non-fissionable material information for multiple regions example used for the modified power iteration method (Ref. 38) (cross-section in cm^{-1})

Group 1						
Σ_{t1}	Σ_{c1}	Σ_{f1}	ν_1	Σ_{1-1}	Σ_{1-2}	χ_1
1.0	0.05	0.0	0.0	0.05	0.9	0.0
Group 2						
Σ_{t2}	Σ_{c2}	Σ_{f2}	ν_2	Σ_{2-1}	Σ_{2-2}	χ_2
1.0	0.1	0.0	0.0	0.0	0.9	0.0

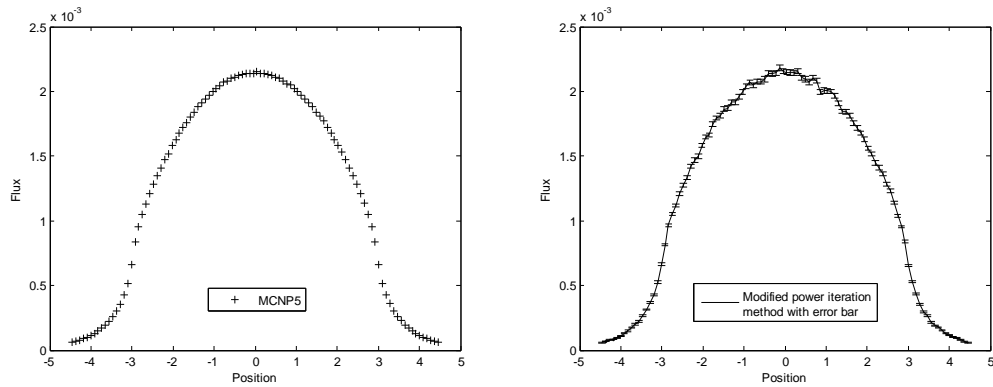
MCNP5 is used to provide a reference k_{eff} from one simulation with 50,000 particles per generation for 1,000 generations after convergence. The Monte Carlo simulation with the modified power iteration method employs 10,000 particles per generation for 100 active generations after 50 inactive generations. **Table 5.6** summarizes the results of the comparison, which are again consistent. The comparisons of the flux estimates are shown in Figure 5.6, from which the agreements can be observed. Moreover, the different shapes of the flux distributions in different energy groups are because of the geometry structure.

Table 5.6. Comparison of k_{eff} for multiple regions example using the modified power iteration method (Ref. 38)

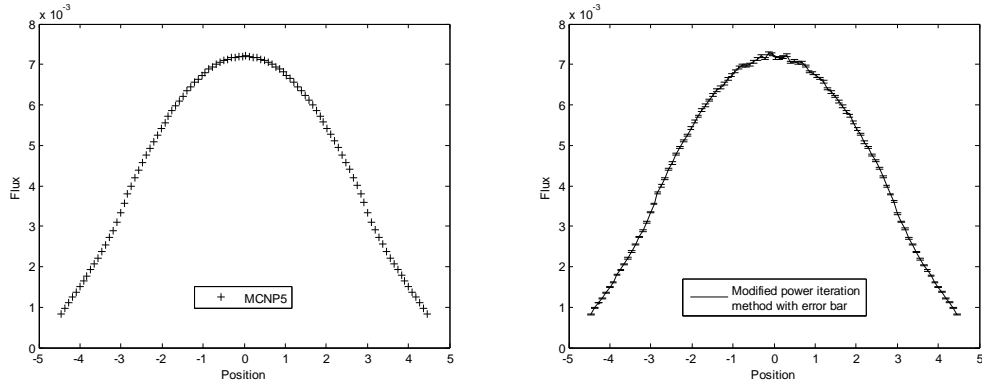
MCNP5	Modified method	Difference
0.90898 ± 0.00009	0.90878 ± 0.00029	0.7σ



(a) Comparison of thermal fluxes



(b) Comparison of fast fluxes



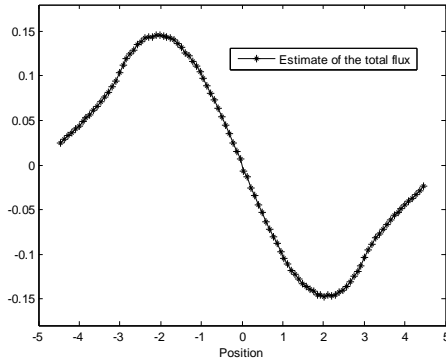
(c) Comparison of total fluxes

Figure 5.6. Comparisons of reference fluxes and computed fluxes for the fundamental eigenmode for multiple regions example using the modified power iteration method (Ref. 38)

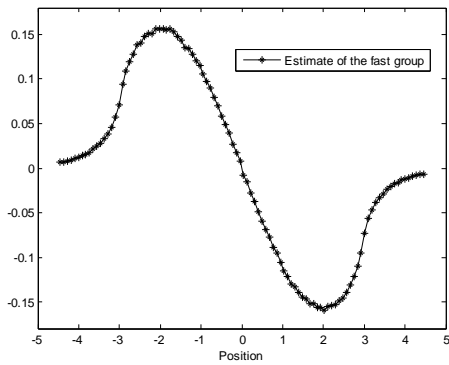
In addition to these computations, the fission matrix method is again used to compute the second eigenvalue and eigenfunction as a reference. **Table 5.7** lists the estimated k_2 from the modified power iteration method and the fission matrix method, which are agreeing well with each other. **Figure 5.7** shows the estimated second eigenfunction. Since the fission matrix method could only give the eigenfunction estimate based on the fission source distribution, it could not provide a valid estimate in reflector regions. Thus, **Figure 5.7** does not include any reference results. Nevertheless, the agreement in k_2 and physical shape of the eigenfunction suggest that **Figure 5.7** could serve as reference for further verifications.

Table 5.7. Comparison of k_2 for multiple regions example using the modified power iteration method (Ref. 38)

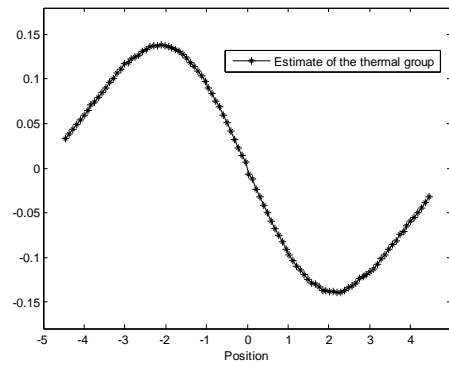
Reference	Modified method	Difference
0.61943	0.61963 ± 0.00063	$< 0.3\sigma$



(a) Estimate of the total flux



(b) Estimate of the fast group



(c) Estimate of the thermal group

Figure 5.7. Comparisons of reference fluxes and computed fluxes for the second eigenmode for multiple regions example using the modified power iteration method (Ref. 38)

5.7 Convergence Acceleration Illustration

The previous examples demonstrate the capability of the modified power iteration method for estimating the fundamental and second eigenvalues and eigenfunction for one-dimensional problems. However, the acceleration capability is only illustrated with simple matrix problem, not actual Monte Carlo simulations. Indeed, the acceleration effect is more difficult to analyze due to several reasons. First of all, most codes calculate only the fundamental eigenpair. Secondly, the random noise associated with the modified

power iteration method is quite large compared to the conventional Monte Carlo simulations. Thirdly, choosing of an appropriate example, which possesses high dominance ratio, but a small k_3/k_1 ratio, is generally hard. Fortunately, other researchers have established some examples for the illustration purpose of the acceleration effect. This section will show one mono-energetic example from the literature followed by the multi-group problem.

In Ref. 32, the authors used a multi-region one-dimensional mono-energetic problem to illustrate the convergence acceleration. The advantage of the problem is that the first several eigenvalues have been computed using a deterministic Green's function method in previous works¹⁵. The dominance ratio of this problem is $k_2/k_1=0.993$ and $k_3/k_1=0.306$. The flux distribution is estimated based on 901 meshes and they use the Eq. (5.34), the mean squared error, to represent the difference between the current estimated flux distribution and a converged flux distribution. In Eq. (5.34), $\Psi_{estimated}(i)$ represents the estimated flux in i^{th} mesh, and $\Psi_{converged}(i)$ represent the converged flux in i^{th} mesh.

$$\text{MSE} = \sqrt{\frac{\sum_{i=1}^{901} (\Psi_{estimated}(i) - \Psi_{converged}(i))^2}{901}} \quad (5.34)$$

The MSEs (noted as rms error in their example) for a simulation using the standard power iteration method and a simulation with the modified power iteration method are shown in **Figure 5.8**. The dash line shows the slow convergence of the conventional Monte Carlo simulation and the red line shows accelerated convergence using the modified power iteration method. Although the exact convergence rate is not listed in this example, clearly, the acceleration has been achieved by using the modified power iteration method.

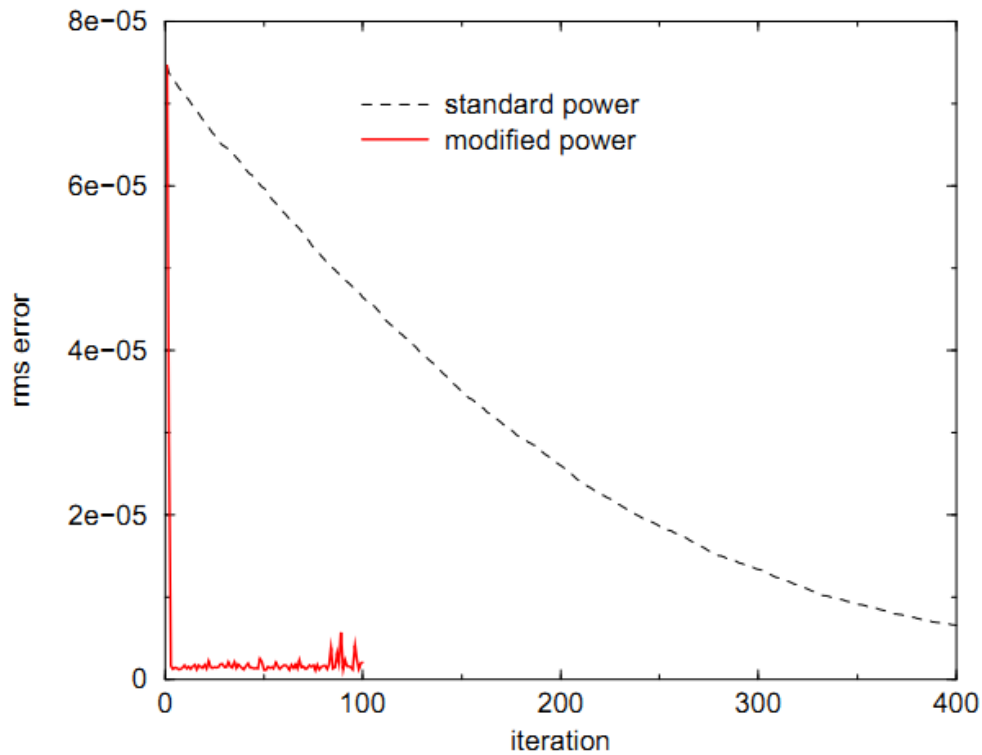


Figure 5.8. Convergence acceleration example (Fig. 5 from Ref. 32)

Thus far, the acceleration has been demonstrated with this mono-energetic problem. The following part analyzes the two-group multi-region problem from the previous section. The reference converged flux distribution is again obtained from the MCNP5 simulation with 50,000 histories per generation for 1,000 generations after convergence. Another two simulations with 500,000 histories per generation with the conventional Monte Carlo method and the modified power iteration method are carried out, respectively, for comparison. The flux estimates after each generation, without the unstable results from the first few generations from these two runs are normalized and compared to the normalized reference flux distribution. **Figure 5.9** shows the differences, in terms of the MSE in logarithmic scale. This figure clearly shows the convergence acceleration effect of the modified power iteration method compared to the conventional Monte Carlo method. The MSE between the flux estimates and the reference flux

distribution decreases faster for the modified power iteration method. Since this illustration example does not have a dominance ratio close to one, the gain from the acceleration is not so significant. However, this demonstration of the acceleration in this two-group example still verifies the capability of the modified power iteration method to accelerate convergence for multi-group or continuous energy problems.

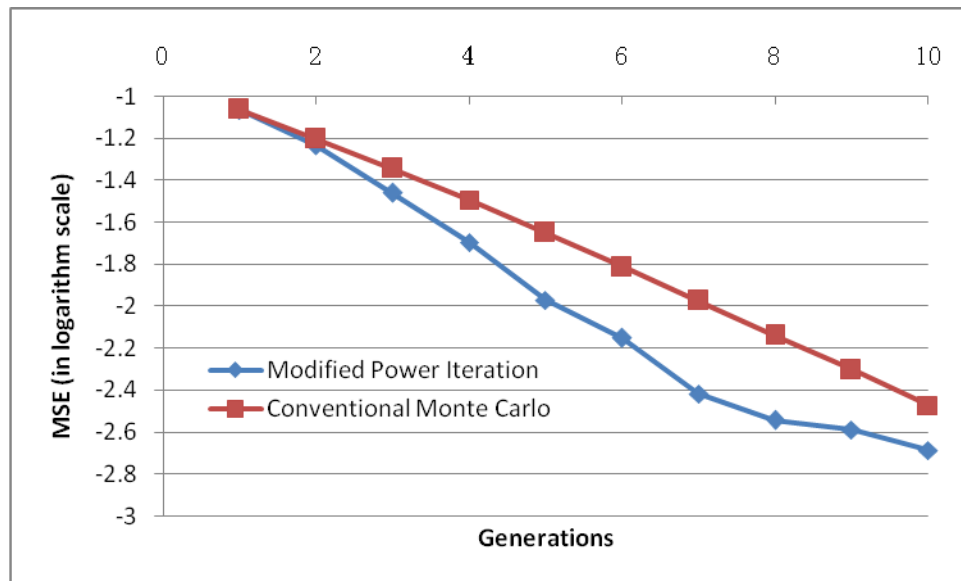
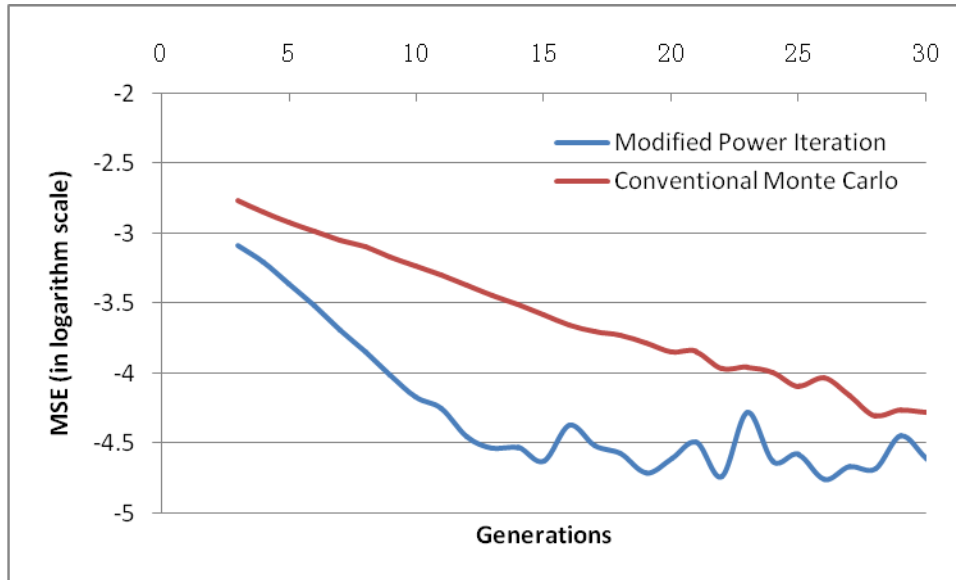
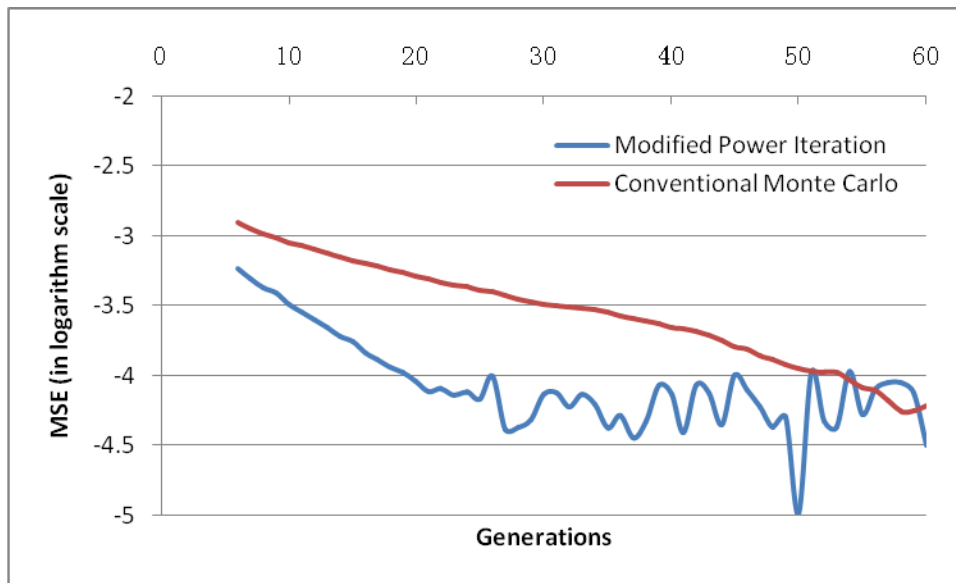


Figure 5.9. Convergence acceleration shown with MSE of the flux distribution in logarithmic scale using the modified power iteration method (problem size 9 MFP)

In order to demonstrate the acceleration effect even more clearly, all the cross-sections for the same example are multiplied by a factor of two and four, respectively, to increase the optical dimension of the system (in mean free path units) and thus enhance the loosely-coupled property. **Figure 5.10** shows the convergence acceleration with MSE of the flux distribution in logarithmic scale for both cases.



(a) Two times increased cross-sections (problem size 18 MFP)



(b) Four times increased cross-sections (problem size 36 MFP)

Figure 5.10. Convergence acceleration shown with MSE of the flux distribution in logarithmic scale using the modified power iteration method with increased cross-sections

Table 5.8 summarizes the fitted convergence rates for the above three cases for the conventional Monte Carlo method and the modified power iteration method. The

fitted convergence rate was obtained using the approximately linear portion of each curve, i.e., before the statistical noise becomes dominant. Additionally, the corresponding numbers of generations needed for the MSE to decrease by one order of magnitude (10 times) is shown. As the dominance ratio increases, the convergence rates for both the conventional Monte Carlo method and the modified power iteration method decrease. However, the impact of the acceleration mechanism will be more significant when the dominance ratio approaches one. Given this fact, the total gain from the modified power iteration method is still a problem-dependent factor, but in all three cases it would take about between two and three times less iterations to achieve the same convergence level using the modified power iteration method.

Table 5.8. Summary of the convergence acceleration effect

Problem size	Conventional Monte Carlo		Modified power iteration method		Speedup factor
	Fitted convergence rate	Number of generations for the MSE decrease by 10 times	Fitted Convergence rate	Number of generations for the MSE decrease by 10 times	
9 MFP	0.686	6.1	0.333	2.1	2.90
18 MFP	0.859	15.1	0.710	6.7	2.25
36 MFP	0.947	42.5	0.874	17.1	2.49

5.8 Recent Developments of Related Methods

Using the modified power iteration method and power iteration related schemes to accelerate the convergence of the fission source distribution has been a topic of interest over the past several years. The work presented in this dissertation along with efforts from other researcher has contributed to this topic significantly. Booth^{39, 40} has used

another similar scheme to primarily estimate the fundamental eigenpair with the convergence acceleration feature, and his testing examples with both matrix problems and MCNP runs have proved the capability of this scheme. The advantage of this scheme is that it does not explicitly estimate the second eigenpair. As a result, the net-weight calculation does not include any negative contributions. Therefore, this implementation is quite straightforward and easy to understand. One disadvantage of this scheme is that it lost the capability of estimating the second eigenpair, which may be crucial in some transient and safety analysis for reactor physics. Another point needing to be pointed out is that this scheme is not fully completed. Although the testing examples seem to be convincing, more derivations and demonstrations are still necessary to understand the applicability and limitations of this scheme.

Another method proposed by Booth⁴¹ is a superfast power iteration method. This method is still based on the previous modified power iteration method with further manipulations. In some situations, an ad hoc bounding condition is necessary to assist the convergence. As a result, the convergence rate could exceed that of the standard modified power iteration method. The improvement of this method is impressive, but the presented work is not quite sufficient to fully understand this method; more analysis and investigations are necessary.

Another modification of the power iteration method has been recently proposed by Booth⁴². This method does not include any negative particles, so the net-weight calculation issue does not exist. This new version requires a set of coefficients assigned to all estimation meshes and sets the estimate of eigenvalue to be equal within these meshes. As a result, a set of multi-variable equations is constructed. By solving these equations and applying the solutions as weights to the source points, this method could also accelerated the convergence, as shown in a simple one-dimensional problem in the reference. However, more investigation is still necessary to validate the method for complex problems and identify the gain out of this scheme.

5.9 Conclusions and Future Work

This chapter demonstrates the capabilities of the modified power iteration method as a power tool to accelerate the convergence of the fission source distribution and compute the higher eigenpairs in the same time. The theoretical foundation of the standard version and refinement version of the method are solid. Testing matrix problems have also verified the convergence acceleration and computational capability. One-dimensional nuclear systems, either with single material or multiple regions of different materials, are used to illustrate the performance of the modified power iteration method. In addition, the application of this method is also successfully extended to two energy group problems as a demonstration of the applicability of the method for multi-group or continuous energy problems. This is a big step forward for the method to be used for practical problems.

Despite these achievements, some questions remain open to be answered as future works as following:

1. Implementation of the modified power iteration method to two-dimensional or three-dimensional problems is still not available. Although the confidence of the method to be working for multi-dimensional problems is strong, implementation examples are still necessary to complete the applicability analysis of the method.
2. The behavior of the variance estimate, both for the fundamental eigenpair and the second eigenpair, still needs more investigation. In general, the conventional Monte Carlo method gives an underestimate of the variance. The variance estimates in the modified power iteration method yet needs to be addressed.
3. The recent developments and improvements based on the modified power iteration method may provide deeper understanding of this method. The analyses of these set of method should be combined together in order to determine the best scheme out of these similar candidate in terms of efficiency, robustness, and requirements.

4. The net-weight calculation with mesh structure is not practical for large scale real-life problems since it requires fine mesh structure for the accuracy of the approximation. As a result, the requirements of the storage space will increase dramatically. Additionally, the estimate of the mesh tally also requires extra computational expense, which sometime is not desired.
5. In order to determine the accuracy of the higher eigenpairs, other practical methods are desired to provide reference results for the higher eigenpairs, such as the second eigenvalue and eigenfunction. Development of this kind of methods is beneficial not only to the modified power iteration method, but also to the other nuclear engineering fields requiring the higher eigenpairs for analysis, such as transient analyses.

The remaining portion of this thesis aims to attack these open questions and difficulties one by one. The next chapter is the current effort trying to at least partly resolve the last two points.

CHAPTER 6

THE SOURCE POINTS PAIRING SCHEME FOR NET-WEIGHT CALCULATION TO OBTAIN THE SECOND EIGENMODE

This chapter aims to develop innovative approach for net-weight calculation, previously referred as cancellation, when the imaginary negative particles are present in the Monte Carlo simulations. Meanwhile, this chapter is also trying to provide some alternative way to compute the second eigenpair for nuclear systems using only the Monte Carlo method.

6.1 Taking into Account the Negative Neutrons

The conventional Monte Carlo method used for nuclear engineering is trying to mimic the behavior of real neutrons, so apparently there should not be any “negative” neutrons in the simulations. The neutron flux distribution should also be non-negative everywhere, which could be represented well by using simulated neutrons. However, the transient states, or higher harmonics of the nuclear system always have some negative regions. These functions may be represented using positive and imaginary “negative” neutrons. These problems with deterministic methods are not as challenging as that with the Monte Carlo method because of the quantitative representations of the deterministic methods. To compute the net-contribution or net-weight from both positive and negative particles can be easily conducted by simple numerical computations. However, the process of the Monte Carlo method includes discrete and random source points, which makes the net-weight calculation difficult to conduct.

In previous chapter, several approaches to compute the net-weight are introduced. Some of them require point-detector like mechanism³⁵ to fulfill the task, which is quite computational expensive when the number of particles used in each generation is large.

Other approaches require a mesh-wise flux or fission density distributions^{32,36} to represent the contributions from either positive or negative particles. As a result, the net-weight calculation is conducted by numerical computation based on the mesh tally structure. Since these approaches are using approximate distribution estimate, the successes of these approaches highly depends on the mesh structure. Only fine mesh could give an accurate approximation in order to achieve accurate results. Thus, storage requirements and computational cost are both increasing along with the complexity of the nuclear system. Further development³⁷ using combination of source points and mesh-wise estimates could relax the fine mesh requirements, but even with this improvement, a coarse mesh structure is still necessary for the net-weight calculation purpose. Other data process techniques such as the histopolating splines⁴³ method could also be used based on the mesh-wise estimates, and provide a more accurate result than the simple histogram estimates with a coarse mesh structure.

Recently, the kernel density estimator⁴⁴ is used for the net-weight calculation by Yamamoto⁴⁵ in order to remove the mesh structure for the estimations. This approach attempts to use the kernel density estimator to accumulate the contributions for simulated particles, either positive or negative particles, and conduct the quantitative computations. Since choosing the kernel density is arbitrary, it still introduces some level of approximations. Fortunately, a well chosen kernel density could lead to acceptable level of accuracy for practical applications. Yamamoto also pointed out that the functional expansion tally method⁴⁶ could also be used as an alternative tool to estimate the distributions, although no direct implementation is available at this point.

Indeed, Monte Carlo simulations with negative particles are not a totally new aspect. Some attempts have been carried out to deal with negative particles in other fields such as in chemistry. The eigenvalue problem nuclear engineers are trying to solve using the Monte Carlo method is similar to the eigenvalue problems that chemists are trying to solve for simple symmetric Bose or antisymmetric Fermi systems. The ground state of a

symmetric Bose system just corresponds to the fundamental eigenmode in a symmetric nuclear system, which is an everywhere non-negative symmetric function. Therefore, a simple Monte Carlo approach⁴⁷ is capable to solve for this ground state. However, when one is interested in the first excited state of a symmetric Bose system or the ground state of an antisymmetric Fermi system, which include both positive and negative values for the functions, the imaginary negative particles have to be taken into account in the Monte Carlo simulation. In Ref. 48, the authors provided their perspectives and possible solutions for this kind of problems, which is the foundation of the following extensions.

6.2 Pairing Net-Weight Calculation

The following analysis focuses on only one-dimensional problems, but the concept is applicable to multi-dimensional problems. However, the implementation may vary for one-dimensional and multi-dimensional problems. The general form of the eigenvalue problem is described in **Chapter 1** from Eq. (1.5) to Eq. (1.7). For convenience, Eq. (6.1) shows the function that eigenvalues k_i and corresponding eigenfunctions Ψ_i should satisfy

$$A \psi_i = k_i \psi_i, \quad (6.1)$$

where $|k_1| > |k_2| > \dots$ is defined in order. Instead of estimating the fundamental eigenpair k_1 and Ψ_1 using the power iteration method, the eigenpair of interest in this chapter is the second one, k_2 and Ψ_2 . For the simplicity of the description, two initial functions, Ψ^+ and Ψ^- , consisting of only the first two eigenfunction components are given as

$$\psi^+ = a_1 \psi_1 + \frac{1}{2} \psi_2 \quad \text{and} \quad \psi^- = a_1 \psi_1 - \frac{1}{2} \psi_2. \quad (6.2)$$

In this equation, the coefficient a_1 is chosen such that both functions are everywhere positive. Therefore, the difference of these two functions is

$$\psi_2 = \psi^+ - \psi^-, \quad (6.3)$$

which is exactly the target eigenfunction in the computation. Thus, if the operator A is applied to Eq. (6.3), the resulting equation will be

$$A\psi_2 = A(\psi^+ - \psi^-) = k_2\psi_2. \quad (6.4)$$

By applying the operator A iteratively to the difference, the estimates of the second eigenvalue and eigenfunction could be obtained just as the traditional power iteration method. If the two functions ψ^+ and ψ^- initially have higher eigenmode components, they will be “powered” out by the iterative method. The key feature here is that the operator A has to be applied to the difference as an entity. Calculating the $A\psi^+$ and $A\psi^-$ separately and computing the difference will not give the desired answer because without effectively compute the difference, each one will converge to the fundamental eigenmode eventually.

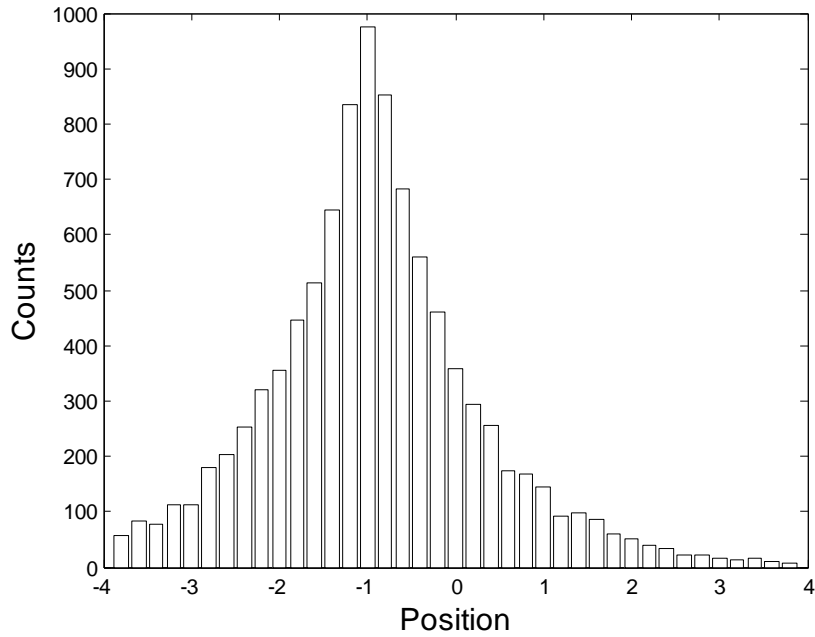
Assuming the two functions ψ^+ and ψ^- are represented with discrete points instead of analytical expression, the calculation of the difference have to be conducted with separate points. To illustrate the pairing scheme, one simple one-dimensional problem without boundaries is considered, which consists of a uniform absorber with $\Sigma_t=1.0 \text{ cm}^{-1}$. Neutrons could only travel in either positive or negative direction; in other words, the system has bi-directional angular dependence. One positive point source is located at $x_1= -1 \text{ cm}$ and another negative point source is located at $x_2=+1 \text{ cm}$. Although x_1 and x_2 are symmetric around zero in this example, the symmetry property is not necessary in general. The collision density distribution or the absorption density distribution for this pure absorber example, corresponding to positive particles from the positive source at $x_1= -1 \text{ cm}$ is

$$f^+(x) = \frac{1}{2} e^{-|x-x_1|}. \quad (6.5)$$

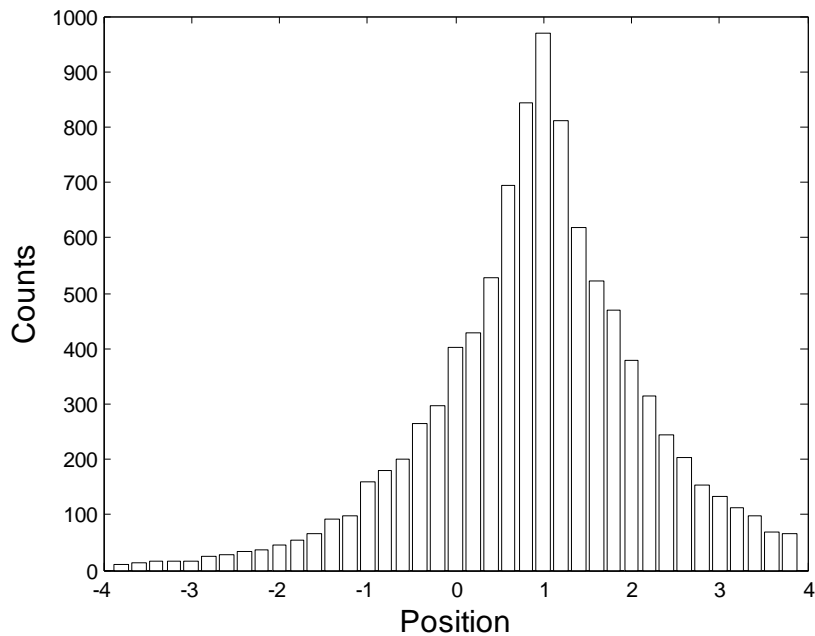
Similarly, the collision density distribution corresponding to negative particles from the negative source at $x_2=+1 \text{ cm}$ is

$$f^-(x) = \frac{1}{2} e^{-|x-x_2|}. \quad (6.6)$$

10,000 collision positions each are sampled according to these two density distributions. **Figure 6.1** shows the histogram of the two sets of samples in the neighborhood of the two point sources. Although the **Figure 6.1(b)** shows the counts as positive numbers, the collision should still be regarded as “negative” collisions, and treated in the opposite way to the positive collisions. Clearly, these histograms represent the shapes of the corresponding density distributions.



(a) Histogram of the collision position samples for positive particles



(b) Histogram of the collision position samples for negative particles

Figure 6.1. Histograms of the collision position samples (Ref. 49)

Therefore, the combination of these two histograms gives the shape of the net collision distribution when taking the sign of counts accordingly. **Figure 6.2** shows the combined histogram, which contains both positive and negative count numbers. When the x coordinate of a collision is smaller than zero, the probability to have a positive collision is higher than the probability to have a negative collision because the position is closer to the positive source position. As a result, the combined histogram has positive counts in this region. A similar argument also applies to the position larger than zero. When the collision position is around zero, the middle of the positive and negative point sources, the probabilities to have either a positive or a negative collision are theoretically the same. Thus, the number of expected counts at positions around zero is almost zero, or relatively small compared to other positions. One more point still needs to be emphasized is that this histogram only represent the shape of the net collision distribution; the number of counts could change according to the initial number of samples.

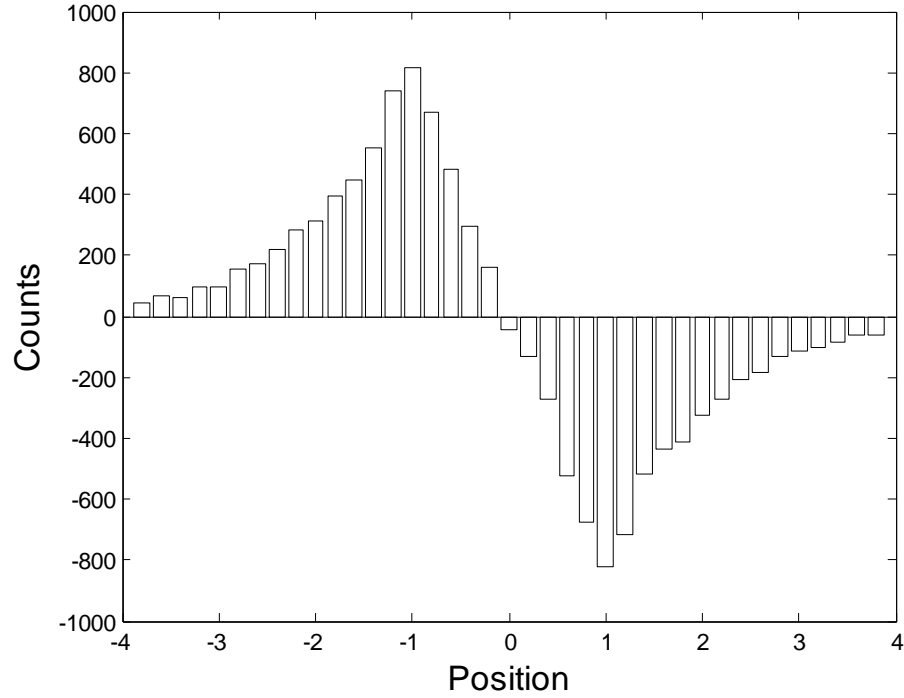


Figure 6.2. Combined histogram of the collision position samples (Ref. 49)

In addition to the above first sampling, then combining procedure, one could actually reverse the procedure to find the shape of the net collision density distribution. From Eq. (6.5) and (6.6), the combined collision “density distribution” is

$$f^{\pm} = f^{+}(x) - f^{-}(x) = \frac{1}{2}e^{-|x-x_1|} - \frac{1}{2}e^{-|x-x_2|}. \quad (6.6)$$

This equation does not represent the conventional density distributions because the function has both positive and negative parts. However, it is still appropriate to represent the collision densities in this example. **Figure 6.3** shows these functions of positive collisions, negative collisions, and combined collisions. The combined function in Eq. (6.6) is positive when x is smaller than the middle of the two point sources, in this case zero; and the function is negative when x is larger than zero. This sign is again determined by the relative distance between the collision position and the point sources:

when the collision is closer to the positive point source, the collision should be regarded as a positive collision.

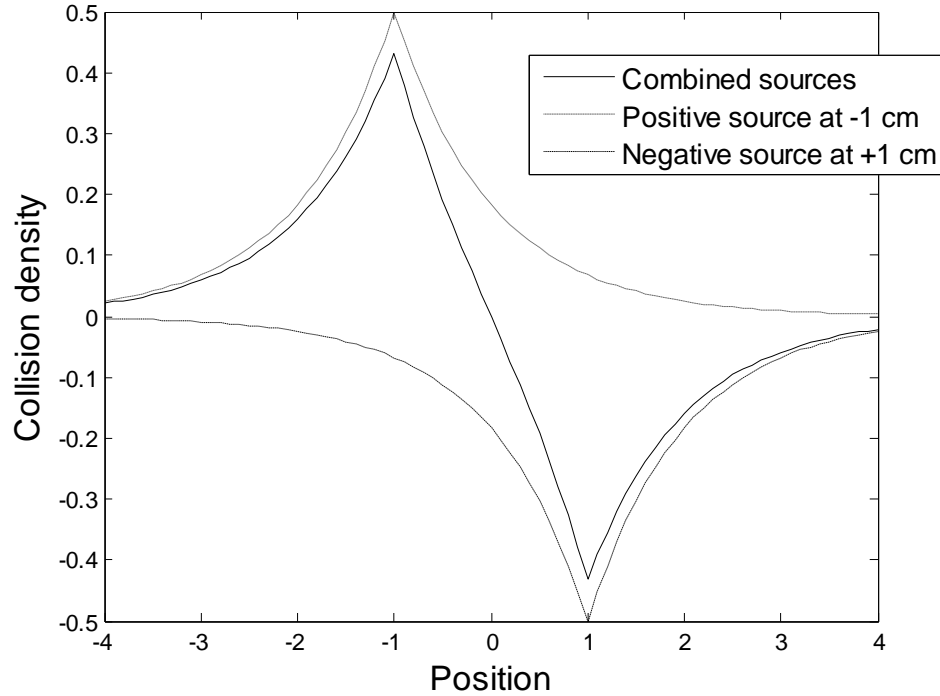


Figure 6.3. Collision density functions for collisions from positive, negative, and combined sources (Ref. 49)

In order to sample the combined collision appropriately, the absolute value of the function in Eq. (6.6) is taken to serve as a conventional density distribution after renormalization using a certain number C , as shown in Eq. (6.7).

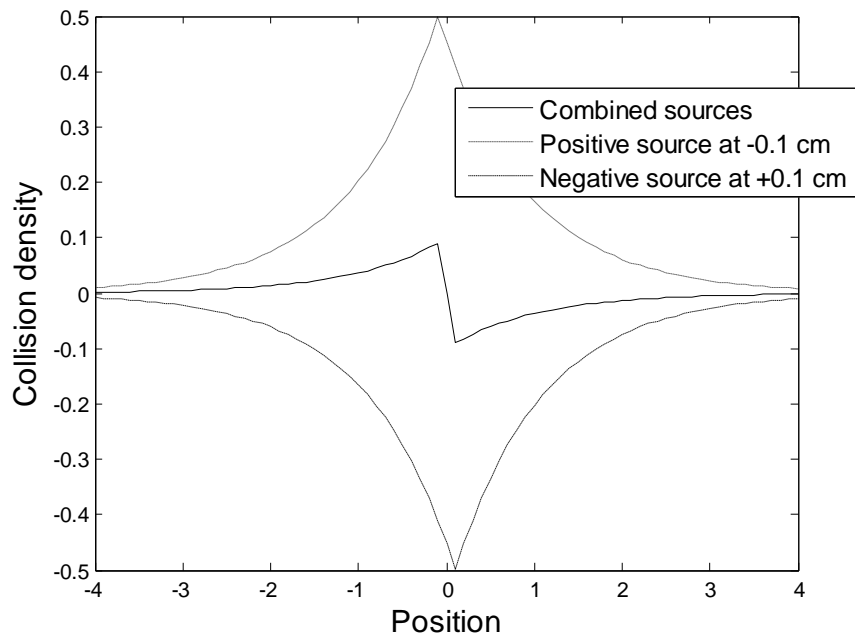
$$|f^\pm| = \frac{1}{C} \left| \frac{1}{2} e^{-|x-x_1|} - \frac{1}{2} e^{-|x-x_2|} \right| \quad (6.7)$$

As a result, collision positions could be sampled from this density distribution. In addition, the type of the collision, either positive or negative, will be determined again according to its relative position to the positive and negative point sources, as before.

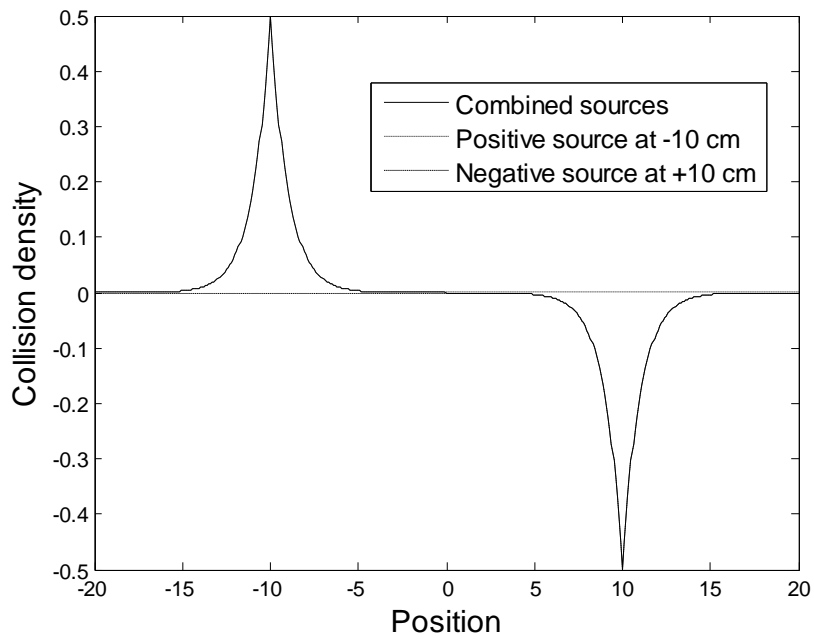
The above sampling technique is called a pairing mechanism. Instead of first

taking samples from two density distributions and calculating the difference, the collision positions are sampled after the combination of density distributions with paired point sources. By reversing the order of actions, this pairing mechanism is actually capable to achieve the previous goal for the net-weight calculation: taking the difference in Eq. (6.4) as an entity first, and applying the operator A, in this case sampling collision positions, to the difference of Ψ^+ and Ψ^- , in this case the two density distributions, $f^+(x)$ and $f^-(x)$.

The efficiency of the sampling depends on the distance between the positive and negative point sources. For example, if the positive and negative point sources are located at the same position, ideally, the net-weight from the collision should be everywhere zero. With the previous taking samples and calculating differences procedure, certain number of collision positions has to be sampled first, and the difference histogram will oscillate around zero, not exactly zero. On the other hand, using the pairing scheme, the computed combined density distribution is everywhere zero. No further sampling procedure is necessary at all to determine the net-collision density. This extreme example illustrates the improvement of the efficiency, and also accuracy to some extent. **Figure 6.4** shows another comparison with positive and negative point sources located at ± 0.1 cm and ± 10.0 cm, respectively. The combined density distribution in **Figure 6.4(b)** is almost the same as the individual density distribution. Therefore, the pairing scheme does not gain much compared to no pairing calculation for distant sources. The other case shown in **Figure 6.4(a)** on the other hand clearly shows the effect of the pairing mechanism in terms of the effective absolute area under the combined density distribution function. Thus, the net-weight calculation will be more effective in this case. To sum up, when the paired positive and negative point sources are close to each other, the pairing mechanism is more efficient for Monte Carlo simulations than when the paired sources are far from each other.



(a) Sources located at ± 0.1 cm



(b) Sources located at ± 10.0 cm

Figure 6.4. Comparison of collision density functions of different point source positions (Ref. 49)

6.3 Issues and Adjustments Prepared for Application to Symmetric One-Dimensional Problems

In order to apply the pairing mechanism to one-dimensional problems, several issues or related adjustments have to be clarified first.

Changes to Conventional Monte Carlo Simulations

Unlike the conventional Monte Carlo simulations, which have only one set of sources as the source bank after each generation, the pair scheme requires two sets of sources, one containing only positive source points and the other containing only negative source points, after each generation. The pairing and sampling technique is applied once to determine the first collision position and the type of collision, either positive or negative. After that, the conventional Monte Carlo simulation resumes to determine the reaction at this collision position and the following traveling and reaction of this simulated history until it is terminated. If the simulated particle causes any fission reaction, the fission position will be recorded in the corresponding source bank.

The number of collision points sampled from one pair is no longer exactly one. Actually, this number depends on the initial weight of the source points and the effective area under the combined density function. Due to this combination, it is most likely that the number of collisions is smaller than one; therefore, weight adjustment has to be performed after each generation to maintain the same total weights to initialize each generation.

Sorting the Source Positions

Based on the efficiency argument in the previous section, it is highly desired to pair the closest positive and negative point sources. However, this desire may not be feasible in general. Arnow investigated several pairing schemes⁵⁰ by comparing their effectiveness and efficiency. It turns out for one-dimensional problems, sorting the

positive sources and negative sources separately, and pairing one positive source with one negative source by the order would be one effective choice for the pair mechanism. For example, two sets of sources, both positive and negative, have five sources each, as shown in **Figure 6.5**. The relative positions of these sources are illustrated according to their true positions. Therefore, the arrows are indicating the pairs according to their orders used under this framework.

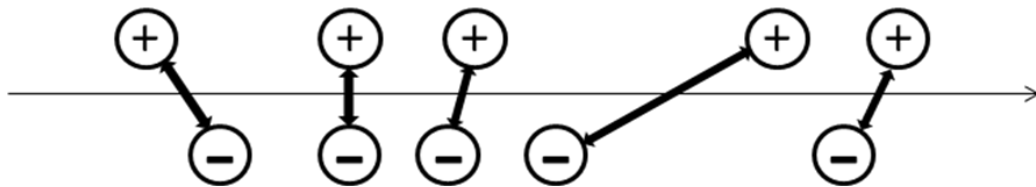


Figure 6.5. Sorting and pairing example (Ref. 49)

This sorting and pairing scheme requires extra computational cost apparently. The quicksort algorithm is used in this dissertation to finish the one-dimensional sorting problem. The complexity of this algorithm is expected to be $O(N \log N)$ in average, where N represents the number of elements in the set. Despite the capability of this sorting and pairing scheme for one-dimensional problems, it may not be suitable for multi-dimensional problems. In multi-dimensional cases, no explicit criterion could be relied on in terms of organizing the pairs. Speculation of one possibility to resolve this difficult is using certain optimization algorithm to minimize the total distance within all pairs. However, this dissertation only addresses only one-dimensional geometries.

Angular Dependence

The previous example using only two point sources assumes that the simulated neutrons travel bi-directionally. In other words, neutrons either travel along the positive direction or the negative direction. Therefore, for one-dimensional problems with bi-

directional angular dependence, the same procedure can be easily applied. When the angular dependence changes to a general one-dimensional case, the sampling procedure becomes more complicated. In general, the cosine of the angle between the travelling direction and positive direction, denoted by μ , needs also to be determined in the sampling procedure. **Figure 6.6** is an illustration of this sampling procedure. After pairing two point sources, μ is sampled first, before the sampling of the collision position. Then, the direction axis is rotated around the mid-point of the source pair from the original solid line to the dash line according to μ . The positive and negative point sources are projected to rotated direction as shown in the figure. The sampling procedure then is conducted along this rotated direction with the projections of the point sources. For instance, a collision position is sampled as the small dash circle in the figure, so it will be back-projected to the original direction as the resulting collision position, denoted with the large dash circle, in the one-dimensional problem. The sign of this collision position is determined the same way as for bi-directional case. By using this rotation, projection, and back-projection technique, the sorting and pairing mechanism could be applied to angular dependent one-dimensional problems.

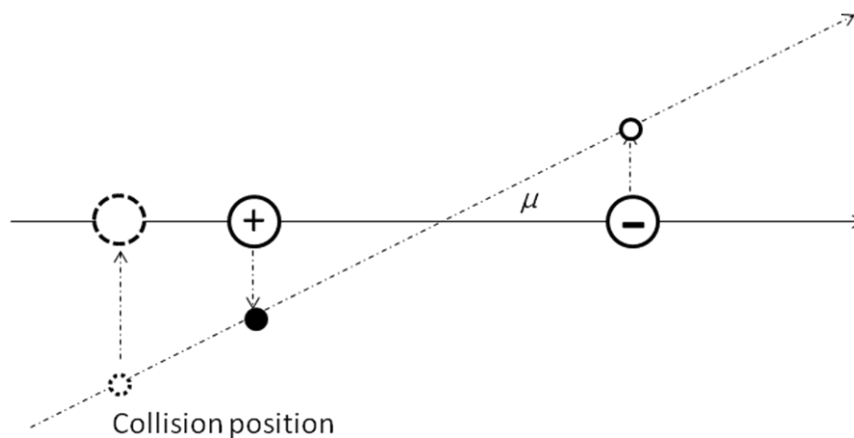


Figure 6.6. Illustration of the sampling procedure with angular dependence (Ref. 49)

Source Renormalization

Due to the statistical feature of the Monte Carlo method, the number of positive and negative source points is generally not the same. However, the pairing scheme requires one-to-one pairing. Therefore, adjustment is necessary for the pairing scheme to work. Let us assume that after one generation, the positive source bank contains n_1 positive sources and the negative source bank contains n_2 negative sources. Without losing generality, here n_1 is assumed to be larger than n_2 . Therefore, $n_1 - n_2$ sources are randomly picked out from the positive source bank and discarded in order to make the numbers of sources in either bank the same. This re-sampling and discarding procedure does not introduce any bias to the simulation because of the randomness, the following renormalization and weight adjustments. Although this adjustment seems to work, it is not the optimal way to deal with the fission source renormalization. However, for now, this simple approach is used for the simplicity.

Estimates of the Eigenfunction and Eigenvalue

The estimate of the eigenfunction still needs a mesh structure. However, this mesh structure is determined based on the objectives of the calculation. If one is only interested in the flux estimate in a certain region, a single mesh could obtain the desired estimation. Under the pairing framework, the positive and negative histories contribute to the tally estimates separately, using the collision estimator. The net flux estimate is calculated using the numerical computation based on the two sets of estimates, considering the sign of the weights contribution to the tally.

The estimate of the eigenvalue is more complicated. Only one set of contributions is recorded, using collision estimator for now, to estimate the eigenvalue. If one weight contribution is from a positive particle in a positive region, or a negative particle in a negative region, this weight contribution is considered positive. On the other hand, if one weight contribution is from a positive particle in a negative region, or a negative particle

in a positive region, this weight contribution is considered negative. In the end, the total net-weight contribution is recorded for further computation. Since the eigenvalue estimate requires some general knowledge of the simulated problem, i.e. of the positive and negative region, it may be more feasible to first roughly determine the boundaries separating these regions, in the inactive generations, and then appropriately reduce the regions' size to effectively discard the contributions close to the boundaries in order to achieve better accuracy and smaller variance. In addition, the number of effective starting sources for one generation, which is the net number of source points in the eigenvalue estimate regions, should also be recorded before initializing each generation. With all these procedures, the estimate of the eigenvalue after one generation could be obtained by dividing the net-weight contribution in the tally region with the effective number of starting sources.

6.4 Application to One-Dimensional Problems

With all the necessary issues and adjustments addressed in the previous section, the pairing net-weight calculation method is ready for computing simple one-dimensional testing problems.

Uniform Mono-energetic Problem

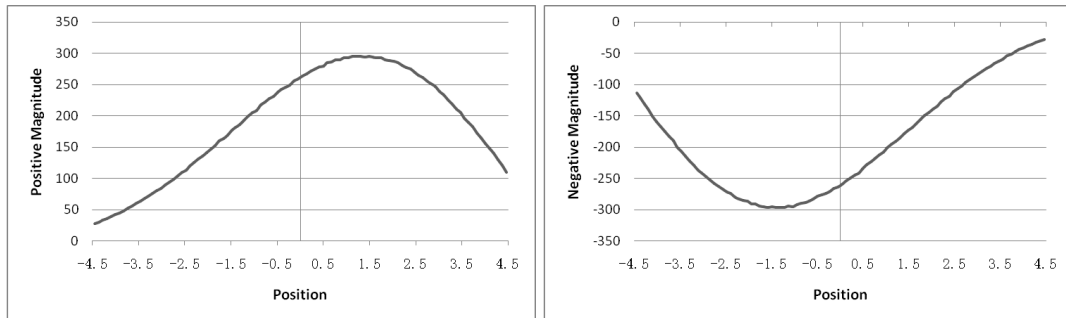
The first one-dimensional example is mono-energetic with bi-directional angular dependence. The system extends from -4.5 cm to +4.5 cm, and only one kind of fissionable material is used to fill the system. The properties of this fissionable material are listed in **Table 6.1**. The simulation initially uses uniformly distributed 20,000 particles per generation per, and is performed for 100 inactive generations and 400 active generations. The eigenfunction estimate is based on 100 equal-size meshes. For this simple example, it is well-known that the eigenfunction changes its sign at zero, so the

small region around zero, in this case chosen to be between -0.5 cm and +0.5 cm, is discarded for the estimate of the eigenvalue.

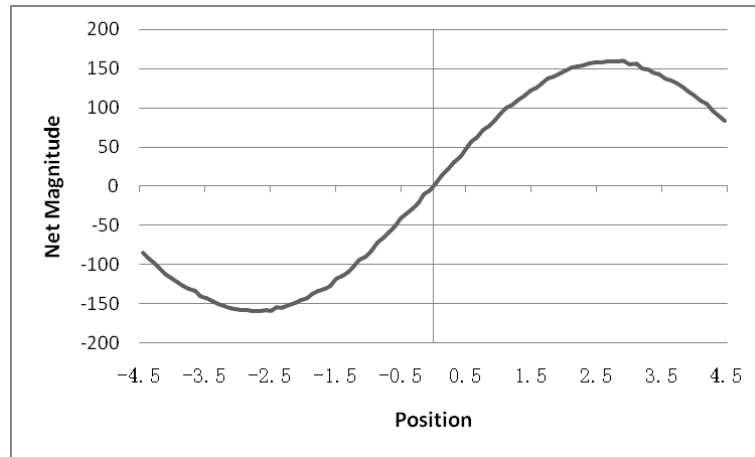
Table 6.1. Properties of the fissionable material used for the mono-energetic example with pairing scheme (Ref. 49)

Σ_t	Σ_c	Σ_s	Σ_f	ν
1.0 cm^{-1}	0.1 cm^{-1}	0.8 cm^{-1}	0.1 cm^{-1}	3.0

Two pairing schemes are chosen to illustrate the efficiency of the net-weight calculation. The first one is the sorting and pairing scheme as described in the previous section. **Figure 6.7** shows the second eigenfunction estimate under this pairing method. The estimate of the second eigenfunction is not renormalized because it is the shape one is trying to calculate. **Figure 6.7(a)** shows the contribution distribution for positive and negative particles, respectively, and **Figure 6.7(b)** shows the net-weight contribution distribution, which is a chopped-sine distribution as expected.



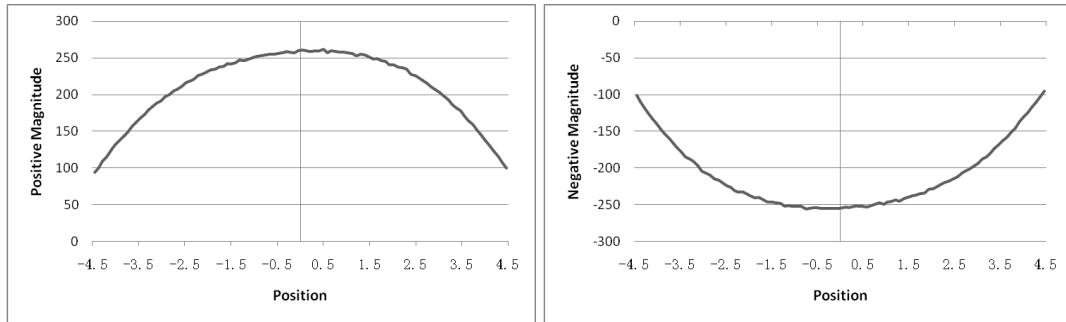
(a) Flux of the positive and negative particles, respectively, tallied over 100 meshes



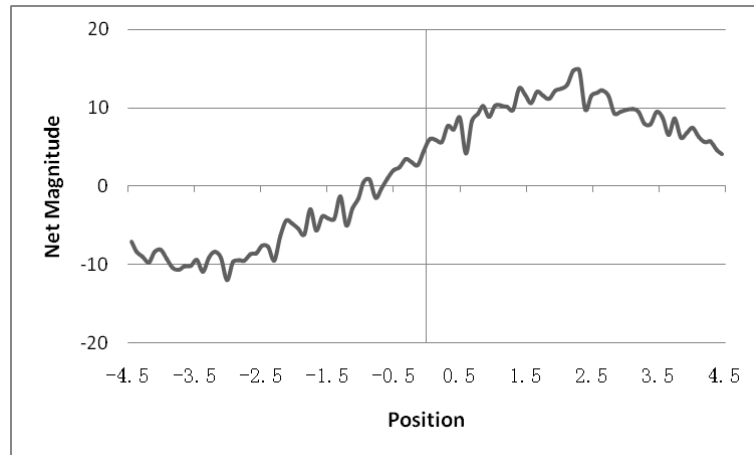
(b) Estimates of the second eigenfunction without normalization

Figure 6.7. Second eigenfunction estimate of the mono-energetic problem using sorting and pairing scheme (Ref. 49)

The comparison example uses a different pairing criterion. This time, choosing the pairs of positive and negative source points is random. In other words, each positive source point has an equal probability to be paired with a negative source point, without any preference. Except this difference, all the other parameters remain the same as in the previous run. **Figure 6.8** shows the second eigenfunction estimate under this scheme. Compared to the **Figure 6.7**, **Figure 6.8(b)** shows a smaller absolute magnitude of the estimate as well as the large relative fluctuation. This difference is because of the low efficiency of the pairing scheme; the sorting and pairing scheme performs better. As stated before, Arnou shows other possible pairing⁵⁰ criteria, among those, the sorting and pairing scheme is still the best of all in terms of efficiency. Therefore, in the following example, the sorting and pairing scheme is the only pairing scheme considered.



(a) Flux of the positive and negative particles, respectively, tallied over 100 meshes



(b) Estimates of the second eigenfunction without normalization

Figure 6.8. Second eigenfunction estimate of the mono-energetic problem using random pairing scheme (Ref. 49)

For the estimate of the second eigenvalue, five repetitions/replicas are performed for comparison purpose. **Table 6.2** lists all the second eigenvalue estimates along with computational times, and their average values with standard deviations across the replicas. The reference k_2 is obtained using the previous modified power iteration method with 50,000 particles per generation and 500 active generation after convergence. A fine mesh approximation with 100 equal-size meshes is used for the net-weight calculation. Another reference run with the conventional Monte Carlo method, with 20,000 particles per generation for 500 generations is used to illustrate the conventional computational time for this problem. Two replicas out of five have difference between their second

eigenvalue estimate and the reference result within two combined standard deviations, and the differences between the other three replicas and the reference results is within one combined standard deviation. The consistency demonstrates the capability and accuracy of the pairing mechanism for computing the second eigenvalue. Moreover, the computational time used for this pairing scheme in this case is comparable to the conventional Monte Carlo simulation. In other words, the price of this simulation is affordable in general.

Table 6.2. Summary of the second eigenvalue estimates with computational time of the mono-energetic problem using pairing scheme (Ref. 49)

		$k_2 \pm 1\sigma$	Computational Time
Pairing method	Replica 1	0.55962 \pm 0.00093	143.796s
	Replica 2	0.55834 \pm 0.00090	154.437s
	Replica 3	0.55744 \pm 0.00089	149.578s
	Replica 4	0.55896 \pm 0.00086	142.968s
	Replica 5	0.55857 \pm 0.00092	142.078s
	Average	0.55859 \pm 0.00036	149.695 \pm 2.402s
Modified power method	k_2 reference	0.55773 \pm 0.00013	--
Conventional Monte Carlo	k_1 reference	--	118.906s

In addition to the estimate of the second eigenfunction and eigenvalue, another issue about the number of effective sources needs to be addressed as well. The net

number of effective sources is smaller than the initially specified 20,000 in this example. However, the determination of the adjusted weights for each point source is still according to the 20,000 rather than the number of effective sources. Since the estimate of the eigenvalue is a ratio, this adjustment does not bias the results, but it does impact efficiency. Therefore, understanding the impact of the number of effective sources is important, and requires more analysis in the future.

Multi-region Two-group Problem

The second illustration example is more complex than the first one. Although it is still a one-dimensional system, it contains three regions filled with two kinds of materials, fissionable and non-fissionable. In addition, this example uses two energy groups instead of one in order to extend the applicability of this net-weight calculation method to more realistic problems. The properties of these materials, which are all arbitrary for illustration purpose, are summarized in **Table 6.3**. The system again extends from -4.5 cm to +4.5 cm. The middle of the system, from -3.0 cm to +3.0 cm is filled with fissionable material, and the other part of the system is filled with non-fissionable material. This is actually the same system specification as used in **Section 5.6**. Finally, this example uses regular angular dependence for one-dimensional systems, rather than the bi-directional simplification.

Table 6.3. Material properties used in the two-group problem for the pairing scheme (all macroscopic cross sections in cm^{-1}) (Ref. 49)

	Fissionable material		Non-fissionable material	
	Group 1	Group 2	Group 1	Group 2
Σ_t	1.0	1.0	1.0	1.0
Σ_c	0.05	0.2	0.05	0.1
Σ_f	0.05	0.1	0.0	0.0
ν	3.0	3.0	--	--
$\Sigma_{\text{inscatter}}$	0.1	0.7	0.05	0.9
$\Sigma_{\text{outscatter}}$	0.8	0.0	0.9	0.0
χ	1.0	0.0	--	--

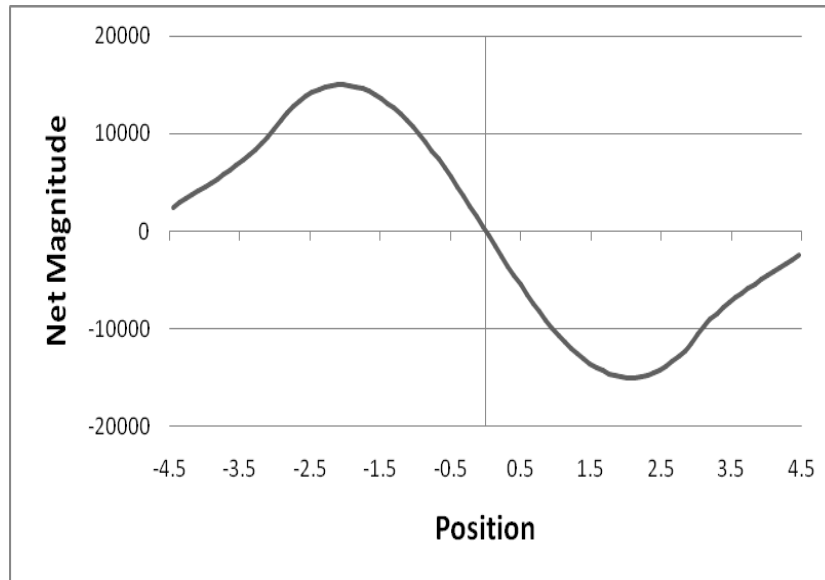
As in the previous example, five repetitions/replicas are simulated with 20,000 particles per generation per set initially for 100 inactive generations and 400 active generations to estimate the second eigenvalue. A reference result is obtained by using the modified power iteration method for 20,000 particles per generation for 400 generations after convergence. All these second eigenvalue estimates are summarized in **Table 6.4** along with some of the computational times. A conventional Monte Carlo simulation with 20,000 particles per generation for 400 generation is carried out for the comparison of the computational time. This time, all five replicas give estimates of the second eigenvalue within one combined standard deviation from reference result. This comparison indicates the capability and applicability of the pairing net-weight calculation method to estimate the second eigenvalue. In addition, the computational time is again

comparable to the conventional Monte Carlo method, which illustrates the efficiency of this method in terms of computational requirements.

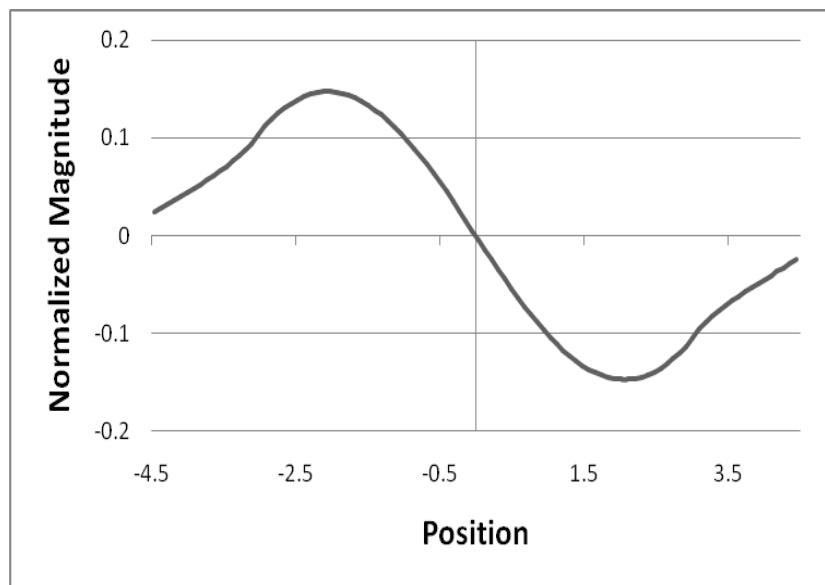
Table 6.4. Summary of the second eigenvalue estimates with computational time of the two-group problem using pairing scheme (Ref. 49)

		$k_2 \pm 1\sigma$	Computational Time
Pairing method	Replica 1	0.61958 \pm 0.00098	158.421s
	Replica 2	0.61969 \pm 0.00093	167.625s
	Replica 3	0.61998 \pm 0.00101	169.093s
	Replica 4	0.61925 \pm 0.00104	170.171s
	Replica 5	0.62089 \pm 0.00098	181.421s
	Average	0.61988 \pm 0.00028	169.346 \pm 3.667s
Modified power method	k_2 reference	0.61963 \pm 0.00063	--
Conventional Monte Carlo	k_1 reference	--	287.359s

In order to compare the accuracy of the estimate of the second eigenfunction, one another run is simulated with 1,000,000 particles per generation per set initially for 500 active generations after convergence. **Figure 6.9** shows the eigenfunction estimates without and with renormalization using the pairing net-weight calculation scheme. The estimate shown in **Figure 6.9(b)** agrees with the previous calculation using the modified power iteration method, shown in **Figure 5.7**.



(a) Without renormalization



(b) With renormalization

Figure 6.9. Second eigenfunction estimate of the two group problem using sorting and pairing scheme

To quantify this agreement, the combined standard deviations are computed between the renormalized second eigenfunction estimate from this simulation and the reference simulation. The difference of the estimates in each mesh is then divided by the

combined standard deviations to provide the relative difference. **Figure 6.10** shows this relative difference in the unit of combined standard deviation. Except for several outliers, most of the differences are within 3σ interval. Considering the possible underestimate effect of the variance, the estimates of the second eigenfunction is quantitatively consistent with reference result.

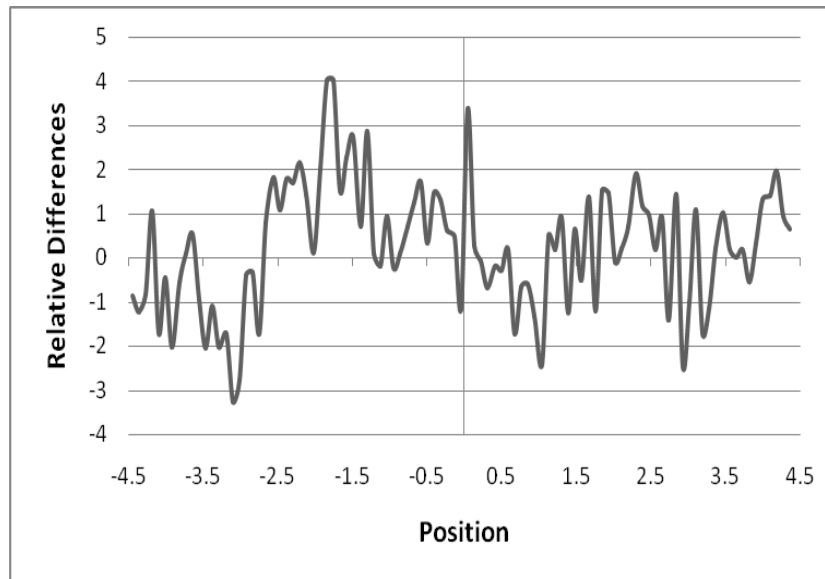


Figure 6.10. Relative differences in the unit of combined standard deviation of the two group problem using sorting and pairing scheme

6.5 Conclusions and Future Work

In this chapter, an innovative approach using pairing net-weight calculation scheme to compute the second eigenpair of a symmetric system is proposed. With certain adjusted procedures, this method could be applied to the Monte Carlo method. The one-dimensional testing examples give consistent estimates of the second eigenvalue and eigenfunction with reference results. Therefore, this chapter has demonstrated the capability, applicability, and accuracy of this net-weight calculation method for symmetric one-dimensional problems. This method could be used to compute the second

eigenpair to provide reference estimates for the validation of other methods, such as the modified power iteration method, in certain cases. In addition, this method could also be integrated to the modified power iteration method as an effective net-weight calculation approach for further development.

Several other issues must be clarified or analyzed to fully understand this method. Although this method works for symmetric one-dimensional problems, to extend the applicability to multi-dimensional problems is not straightforward. As stated in the previous section, since there is no clear criterion for sorting the source points in a multi-dimensional space, alternative approaches, perhaps using optimization theory, are necessary for the method to succeed. The source renormalization for each generation needs to be investigated further for the future implementation or improvement. The behavior of the variance may be totally different than in traditional Monte Carlo simulations because the estimate of the second eigenpair using solely the Monte Carlo approach is novel and different. Thus, the understanding of the variance will help the comprehension of the estimates. All of these aspects could be topic of a future work. Again, this chapter only reveals several of the advantages of this pairing net-weight calculation method, but more research has to be done in the future to support the development of this method for practical 3-D multi-group problems.

CHAPTER 7

CONCLUSIONS AND FUTURE WORK

The Monte Carlo method is widely used to solve the criticality or eigenvalue problems in nuclear engineering. The computation of the fundamental eigenvalue and eigenfunction is based on the power iteration method which requires discarding certain number of generations (cycles) before the convergence is reached. Several difficulties arise along with using the Monte Carlo method for power iteration calculation. One of the difficulties is that the non-convergence period is hard to determine in general due to the statistical nature of the Monte Carlo method. Another difficulty is the slow convergence rate for loosely coupled systems, which requires large amount of computational effort. Therefore, the objective of this dissertation is trying to provide some perspective and develop novel approaches to overcome these difficulties.

In Chapter 3, the linear regression model is applied to cycle-wise mesh tallies for convergence diagnostics purpose. The significance level could be chosen to be between 0.10 and 0.20 in common cases, and different levels have almost no effect on the diagnostics. Another parameter, the regression size, should be chosen according to the experience of users, as an acceptable convergence criterion. In the two test examples analyzed, this method shows the capability of providing diagnostics results comparable to or even more robust than other indicators, such as the entropy indicator, with appropriately chosen parameters. The attempt to remove the auto-correlation did not produce the expected results when applied to the same simulation examples; however, since theoretically it should provide improvement, this attempt should be carried on in future work. Other future work should include more testing examples to verify the applicability and limitations of this method. An automated mechanism is also desired to determine the optimal regression size and confidence level for any given systems.

In Chapter 5, the modified power iteration method is explained and demonstrated with detailed mathematical derivations. The modified power iteration method is capable of computing the fundamental eigenpair as well as higher eigenpairs, such as the second eigenvalue and eigenfunction of a nuclear system. Meanwhile, it could also accelerate the convergence rate in order to reduce the computational cost for convergence. After a simple matrix test problem, and several one-dimensional mono-energetic problems, the modified power iteration method is successfully applied to solve one-dimensional two-group criticality problems. The applicability of the method to multi-group problems indicates the potential of the method to be applied to real-life problems. Future work should include extending this method to multi-dimensional problems and investigating the variance estimate. Moreover, the presence of the negative histories opens a new question about how to calculate the net-weight contribution from both positive and negative particles.

Chapter 6 answers the question about the net-weight calculation using a pairing scheme, which combines the collision density distribution from each pair of positive and negative sources to sample the collision position. By using two source banks, the pairing scheme works with an iterative method to compute directly the second eigenvalue and eigenfunction for symmetric one-dimensional systems. However, the concept of the pairing scheme is not limited to symmetric problems; future work could aim to extend the method to general asymmetric systems. It could then serve as an effective net-weight calculation method as one component of the modified power iteration method in order to relax the requirement for mesh-wise net-weight calculation. Future work should include choosing an optimal pairing criterion for multi-dimensional problems and applying this method into the modified power iteration method for efficient simulations.

REFERENCES

- [1] N. Metropolis, "The Beginning of the Monte Carlo Method," *Los Alamos Science*, Special Issue (1987).
- [2] E. E. Lewis and W. F. Miller, Jr., *Computational Methods of Neutron Transport*, American Nuclear Society, Inc., 1993.
- [3] G. H. Golub and C. F. Van Loan, *Matrix Computations (Johns Hopkins Studies in Mathematical Sciences) (3rd Edition)*, 1996.
- [4] G.E. Whitesides, "A difficulty in computing the k-effective of the World," *Transactions of the American Nuclear Society*, **14**, 680 (1971).
- [5] T. E. Booth, "Power Iteration Method for the Several Largest Eigenvalues and Eigenfunctions," *Nuclear Science and Engineering*, **154**, 48–62 (2006).
- [6] B. Petrovic, "Numerical Demonstration of Source Convergence Issues in Monte Carlo Eigenvalue Simulations," *Transactions of the American Nuclear Society*, **84**, 173-175 (2001).
- [7] G. E. Whitesides, "Fission Source Convergence in Identical Arrays of Fissile Materials," *Transactions of the American Nuclear Society*, **45**,338 (1983).
- [8] R. N. Blomquist, M. Armishaw, D. Hanlon, N. Smith, Y. Naito, J. Yang, Y. Mioshi, T. Yamamoto, O. Jacquet and J. Miss, *Source Convergence in Criticality Safety Analysis*, NEA Report No. 5431, Nuclear Energy Agency, Organization for Economic Co-operation and Development, 2006.
- [9] R. Blomquist, A. Nouri, M. Armishaw, O. Jacquet, Y. Naito, Y. Miyoshi, and T. Yamamoto, "OECD/NEA Source Convergence Benchmark Program: Overview and Summary of Results," *Proc. 7th Intl. Conf. on Nuclear Criticality Safety*, **Vol I**, 278-282 (2003).
- [10] Y. Naito and J. Yang, "The Sandwich Method for Determining Source Convergence in Monte Carlo Calculation," *Journal of Nuclear Science and Technology*, **Vol. 41**, No. 5, p. 559-568 (2004).

- [11] B. Shi and B. Petrovic, "Investing the Use of Entropy-based Convergence Indicator in Monte Carlo Eigenvalue Simulations of Large Loosely-coupled Systems," *Joint International Conference on Supercomputing in Nuclear Applications and Monte Carlo 2010 (SNA+MC2010)*, Tokyo, Japan, 2010.
- [12] T. Ueki and F. B. Brown, "Informatics Approach to Stationarity Diagnostics of the Monte Carlo Fission Source Distribution," *Transactions of the American Nuclear Society*, **89**, 458 (2003).
- [13] T. Ueki and F. B. Brown, "Stationarity Modeling and Informatics-Based Diagnostics in Monte Carlo Criticality Calculations," *Nuclear Science and Engineering*, **149**, 38-50 (2005).
- [14] X-5 Monte Carlo Team, "MCNP – A General Monte Carlo N-particle Transport Code, Version 5," *Los Alamos National Laboratory*, (2003)
- [15] T. Ueki, F. B. Brown, D. K. Parsons and D. E. Kornreich. "Autocorrelation and Dominance Ratio in Monte Carlo Criticality Calculations," *Nuclear Science and Engineering*, 145, 279-290 (2003).
- [16] M. Wenner and A. Haghghat, "A generalized KPSS test for stationarity detection in Monte Carlo eigenvalue problems," *International Conference on the Physics of Reactors(PHYSOR2008) "Nuclear Power: A Sustainable Resource,"* Casino-Kursaal Conference Center, Interlaken, Switzerland, September 14-19, 2008.
- [17] M. Wenner and A. Haghghat, "A Combined Diagnostic Approach for Monte Carlo Source Convergence Identification," *International Conference on Mathematics, Computational Methods & Reactor Physics(M&C2009)*, Saratoga Springs, New York, May 3-7, 2009, on CD-ROM, American Nuclear Society, LaGrange Park, IL (2009).
- [18] H. J. Shim and C. H. Kim, "Convergence Criterion of Fundamental Mode Fission Source Distribution in Monte Carlo Calculations," *The Monte Carlo Method: Versatility Unbounded In A Dynamic Computing World(M&C2005)*, Chattanooga, Tennessee, April 17-21, 2005, on CD-ROM, American Nuclear Society, LaGrange Park, IL (2005).
- [19] H. J. Shim and C. H. Kim, "Stopping Criteria of Inactive Cycle Monte Carlo Calculations," *Nuclear Science and Engineering*, **157**, 132-141 (2007).

- [20] M. Kutner, C. Nachtsheim, J. Neter, and W. Li, *Applied Linear Statistical Models (Fifth Edition)*, McGraw-Hill Irwin (2004).
- [21] B. Shi and B. Petrovic, "Convergence Diagnostics for Eigenvalue Problems with Linear Regression Model," *International Conference on Mathematics and Computational Methods Applied to Nuclear Science and Engineering(M&C2011)*, Rio de Janeiro, RJ, Brazil, May 8-12, 2011, on CD-ROM, Latin American Section/American Nuclear Society (2011).
- [22] B. Shi and B. Petrovic, "Convergence Diagnostics Using Auto-correlated Linear Regression Model on Cycle-based Mesh Tally," *Transactions of the American Nuclear Society*, **Vol. 104**, 385-387, Hollywood, Florida, June 26–30, 2011.
- [23] C. Hildreth and J. Y. Lu, "Demand relations with autocorrelated disturbances," *Technical Bulletin 276*, Michigan State University, Agricultural Station (1960).
- [24] K. Morton, "Criticality Calculations by Monte Carlo Methods," *AERE-T/R-1903*, Harwell, 1956.
- [25] J. Wagner, S. Mosher, T. Evans, D. Peplow and J. Turner, "Hybrid and Parallel Domain-Decomposition Methods Development to Enable Monte Carlo for Reactor Analyses," *Joint International Conference on Supercomputing in Nuclear Applications and Monte Carlo 2010 (SNA+MC2010)*, Tokyo, Japan, 2010.
- [26] S. Yun and N. Z. Cho, "Monte Carlo Anchoring Method for Loosely-Coupled k-Eigenvalue Problems," *International Conference on Mathematics, Computational Methods & Reactor Physics(M&C2009)*, Saratoga Springs, New York, May 3-7, 2009, on CD-ROM, American Nuclear Society, LaGrange Park, IL (2009).
- [27] N. Z. Cho, G. S. Lee, and C.J. Park, "Partial Current-Based CMFD Acceleration of the 2D/1D Fusion Method for 3D Whole-Core Transport Calculations," *Transactions of the American Nuclear Society*, **88**, 594 (2003).
- [28] T. Yamamoto and Y. Miyoshi, "Reliable Method for Fission Source Convergence of Monte Carlo Criticality Calculation with Wielandt's Method," *Journal of Nuclear Science and Technology*, **Vol. 41**, No. 2, 99-107 (2004).
- [29] F. Brown, "Fundamentals of Monte Carlo Particle Transport," *Report No. LA-UR-05-4983*, Los Alamos National Laboratory, 2005.

- [30] D. Griesheimer and B. Toth, "A Novel Source Convergence Acceleration Scheme for Monte Carlo Criticality Calculations, Part I: Theory," *Joint International Topical Meeting on Mathematics Computation and Supercomputing in Nuclear Applications(M&C+SNA2007)*, Monterey, California, April 15-19, 2007, on CD-ROM, American Nuclear Society, LaGrange Park, IL (2007).
- [31] D. Griesheimer and B. Toth, "A Novel Source Convergence Acceleration Scheme for Monte Carlo Criticality Calculations, Part II Implementation and Results," *Joint International Topical Meeting on Mathematics Computation and Supercomputing in Nuclear Applications(M&C+SNA2007)*, Monterey, California, April 15-19, 2007, on CD-ROM, American Nuclear Society, LaGrange Park, IL (2007).
- [32] T. E. Booth and J. E. Gubernatis, "Improved Criticality Convergence via a Modified Monte Carlo Power Iteration Method," *International Conference on Mathematics, Computational Methods & Reactor Physics(M&C2009)*, Saratoga Springs, New York, May 3-7, 2009, on CD-ROM, American Nuclear Society, LaGrange Park, IL (2009).
- [33] J. E. Gubernatis and T. E. Booth, "Multiple Extremal Eigenpairs by the Power Method," *Journal of Computational Physics*, **227**, 8508–8522 (2008).
- [34] B. Shi and B. Petrovic, "Analysis of The Higher Eigenfunction Calculation Using a Modified Power Iteration Method," *PHYSOR2010, Advances in Reactor Physics to Power the Nuclear Renaissance*, Pittsburgh, Pennsylvania, USA, May 9-14, 2010, on CD-ROM, American Nuclear Society, LaGrange Park, IL (2010).
- [35] T. E. Booth, "Computing the Higher k-Eigenfunctions by Monte Carlo Power Iteration: A Conjecture," *Nuclear Science and Engineering*, **143**, 291-300 (2003).
- [36] T. Yamamoto, "Convergence of the Second Eigenfunction in Monte Carlo Power Iteration," *Annals of Nuclear Energy*, **36**, 7-14 (2009).
- [37] T. Booth and J. Gubernatis, "Exact Regional Monte Carlo Weight Cancellation for Second Eigenfunction Calculations," *Nuclear Science and Engineering*, **165**, 283-291 (2010).
- [38] B. Shi and B. Petrovic, "Implementation of the modified power iteration method to two-group Monte Carlo eigenvalue problems," *Annals of Nuclear Energy*, **38**, 781-787 (2011).

- [39] T. Booth, “Eigenfunction Convergence Acceleration Example —Implications for MCNP,” Los Alamos National Laboratory Report LA-UR 10-01644 (2010).
- [40] T. Booth, “Eigenfunction Convergence Acceleration Experiments in MCNP,” Los Alamos National Laboratory Report LA-UR 10-04872 (2010).
- [41] T. Booth, “Examples of Superfast Power Iteration,” Los Alamos National Laboratory Report LA-UR 10-06663 (2010).
- [42] T. Booth, “A Simple Eigenfunction Convergence Acceleration Method for Monte Carlo,” *International Conference on Mathematics and Computational Methods Applied to Nuclear Science and Engineering (M&C2011)*, Rio de Janeiro, RJ, Brazil, May 8-12, 2011, on CD-ROM, Latin American Section/American Nuclear Society (2011).
- [43] R. Siewer, “Histopolating Splines,” *Journal of Computational and Applied Mathematics*, **220**, 661–673 (2008)
- [44] K. Banerjee and W. Martin, “A Proposed Kernel Density Estimator Method for Monte Carlo Eigenvalue Calculations,” *Proc. Int. Conf. Physics of Reactors (PHYSOR08)*, Interlaken, Switzerland, September 14–19, 2008.
- [45] T. Yamamoto, “Non-Regionwise Weight Cancellation for Monte Carlo Higher Order Criticality Calculations Using Kernel Density Estimator,” *Annals of Nuclear Energy*, **38**, 2515–2520 (2011).
- [46] D. Griesheimer, W. Martin, and J. Holloway, “Convergence Properties of Monte Carlo Functional Expansion Tallies,” *Journal of Computational Physics*, **211**, 129–153 (2006).
- [47] M. Kalos, “Monte Carlo Calculations of the Ground State of Three- and Four-Body Nuclei,” *Physics Review*, **Vol. 128**, No. 4 (1962).
- [48] D. Arnow, M. Kalos, M. Lee, and K. Schmidt, “Green’s Function Monte Carlo for Few Fermion Problems,” *Journal of Chemical Physics*, **77**, 5562-5572 (1982).
- [49] B. Shi and B. Petrovic, “Calculating the Second Eigenpair in Criticality Calculations Using the Monte Carlo Method with Source Points Pairing as an

Efficient Net-Weight (“Cancellation”) Algorithm,” *Nuclear Science and Engineering* (under review)

- [50] D. Arnow, *Stochastic Solutions to the Schrodinger Equations for Fermions*, Ph.D. dissertation, New York University (1982).